

Doctor Thesis  
Theoretical study  
on superconducting gap structures  
and pairing mechanisms  
of iron based superconductors  
( 鉄系超伝導体における超伝導ギャップ構造及び  
ペアリング機構の理論研究 )

Condensed-matter theory group,  
Department of Physics,  
Graduate school of Science,  
Nagoya University  
461202042 Tetsuro Saito  
February 20, 2015

# Contents

<b>1</b>	<b>Introduction</b>	<b>4</b>
1.1	Background . . . . .	4
1.2	Typical $T$ - $x$ (doping rate) phase diagram . . . . .	5
1.3	Crystal structures . . . . .	6
1.4	Electronic band structures . . . . .	8
1.5	Candidates of pairing mechanisms and superconductive symmetry: spin-fluctuation-mediated $s_{\pm}$ -wave state and orbital-fluctuation-mediated $s_{++}$ -wave state . . . . .	9
1.6	Orbital-spin fluctuation theory . . . . .	10
1.6.1	Interaction terms . . . . .	10
1.6.2	Spin and orbital fluctuations . . . . .	11
1.7	$s_{++}$ and $s_{\pm}$ -wave superconducting gap functions . . . . .	14
1.8	The contents of this thesis . . . . .	15
<b>2</b>	<b>Heavily electron doped compound (<math>\text{KFe}_2\text{Se}_2</math>)</b>	<b>17</b>
2.1	Introduction for $\text{KFe}_2\text{Se}_2$ . . . . .	17
2.2	Tight binding model of $\text{KFe}_2\text{Se}_2$ . . . . .	18
2.3	Random phase approximation . . . . .	19
2.4	Eliashberg gap equation . . . . .	21
2.5	Summary . . . . .	24
<b>3</b>	<b>Reproduction of experimental gap structure in <math>\text{LiFeAs}</math></b>	<b>25</b>
3.1	Introduction for $\text{LiFeAs}$ . . . . .	25
3.2	Formalism . . . . .	26
3.3	SC gap functions . . . . .	30
3.3.1	Orbital-fluctuation-mediated $s_{++}$ -wave state . . . . .	30
3.3.2	Spin-fluctuation-mediated $s_{\pm}$ -wave state . . . . .	31
3.3.3	Coexistence of orbital and spin fluctuations: $s_{++}$ -wave and hole- $s_{\pm}$ -wave states . . . . .	32
3.4	Spin-orbit interaction . . . . .	34
3.4.1	Hamiltonian including SOI . . . . .	36
3.4.2	Eliashberg gap equation with SOI . . . . .	38
3.4.3	Gap structure in the case where only the outer $d_{xz/yz}$ -orbital hole band at Z point crosses the Fermi level . . . . .	40
3.4.4	Gap structure in the case where only the inner $d_{xz/yz}$ -orbital hole band at Z point crosses the Fermi level . . . . .	42

3.5	Summary . . . . .	44
<b>4</b>	<b>Loop nodes on the e-FSs of <math>\text{BaFe}_2(\text{As,P})_2</math></b>	<b>47</b>
4.1	Introduction for $\text{BaFe}_2(\text{As,P})_2$ . . . . .	47
4.2	Formulation . . . . .	48
4.3	SC gap structures . . . . .	51
4.3.1	$s_{\pm}$ -wave SC gap mediated by spin fluctuations . . . . .	52
4.3.2	$s_{++}$ -wave SC gap mediated by orbital fluctuations . . . . .	53
4.3.3	Loop-shape nodes due to the competition of spin and orbital fluctuations . . . . .	54
4.4	Discussion . . . . .	60
4.5	Summary . . . . .	60
<b>5</b>	<b>Summary</b>	<b>62</b>
<b>A</b>	<b>Five orbital tight binding model for LiFeAs</b>	<b>65</b>
<b>B</b>	<b>Hole-<math>s_{\pm}</math> wave state in Ba122</b>	<b>67</b>

# 1 Introduction

Since the discovery of Fe-based high- $T_c$  superconductors by Kamihara *et al* [1], the pairing mechanism and superconducting (SC) symmetry had been studied very intensively. In this section, we explain the present situation of the study on Fe-based superconductors. Next, we describe the contents of this thesis.

## 1.1 Background

Superconductivity is a significant research field for not only engineering but also fundamental physics. Understanding the mechanisms of the superconductivity is one of the most important themes. Since Kamerlingh Onnes found that electronic conductivity of mercury becomes zero below the critical temperature  $T_c$  [2], a lot of efforts had been devoted in order to reveal the mechanism. Primarily, the mechanism is explained by Bardeen, Cooper, and Schrieffer [3]. According to the BCS theory, superconductivity is realized by electrons forming Cooper pairs realized by attractive interaction between electrons and phonon. This theory explains superconductivity in weakly correlated electron systems. However, in 1987, high- $T_c$  cuprate superconductors were found [4].  $T_c$  of cuprates is too high to be explained by BCS theory. The interaction causing the pairing is mediated by spin fluctuations.

In 2008, iron based superconductors were found [1] and  $T_c$  leaped to 55K immediately. At present, it is the superconductor with the highest  $T_c$  next to cuprates. Iron based superconductors had been studied intensively from a lot of aspects since not only do they have very high  $T_c$  but also a new pairing mechanism different from that of cuprates can be realized in iron pnictides.

In iron pnictides,  $3d$  electrons construct the electronic structure near the Fermi level and all of five  $d$  electrons play prominent roll. Therefore, iron based superconductor is a multiorbital system, differently from single orbital cuprate. In many iron pnictides, antiferromagnetic and orbital orders are realized in the mother compounds. By doping the carrier, these long range orders vanish and the superconductivity is realized. Therefore, in the superconducting phase, both the spin and orbital fluctuations are developed. Since these fluctuations mediate the pairing interaction of the cooper pairs, theorists had been studied the scenarios of both the spin-fluctuation-mediated superconductivity [5] and orbital-fluctuation-mediated superconductivity [6].

In the spin-fluctuation-mediated superconductivity, the  $s$ -wave state with

sign reversal ( $s_{\pm}$ -wave state) is realized [5]. However, the  $s_{\pm}$ -wave superconducting state is very fragile against the non-magnetic impurity because of the sign change of the superconducting gap [7, 8]. Although the  $s_{\pm}$ -wave state with  $T_c=30\text{K}$  is predicted to disappear when the residual resistivity  $\rho_0$  is as small as  $20 \sim 30 \mu\Omega\text{cm}$  [9, 10], the superconductivity of iron pnictides is very robust against impurities up to  $\rho_0 = 300 \sim 500 \mu\Omega\text{cm}$ . In addition, the correlation between  $T_c$  and the strength of spin fluctuations is unclear in various compounds. For example,  $T_c$  of  $\text{Ba(Fe,Co)}_2\text{As}_2$  and  $\text{LiFeAs}$  are similar. However, the spin fluctuations are developed in  $\text{Ba(Fe,Co)}_2\text{As}_2$  [11] although are weak in  $\text{LiFeAs}$  [12] according to the NMR experiments.

On the other hand, in the orbital-fluctuation-mediated superconductivity, the  $s$ -wave state without sign reversal ( $s_{++}$ -wave state) is realized [6]. In this case, the robustness of impurity is consistent because the  $s_{++}$ -wave state do not have the sign change of superconducting gap functions [9, 10].

Development of orbital fluctuations is explained by the Aslamazov-Larkin-type term of vertex correction (VC) [13, 14]. Indeed, the orbital fluctuations are developed in self consistent VC (SC-VC) method. By applying SC-VC method, the property of normal state, for example, structural phase transition [14], softening of sheer modulus  $C_{66}$  [15], and so on, can be explained.

For understanding the mechanism of the superconductivity, the study of superconducting gap structure is significant. In the case of cuprates, the  $d$ -wave superconducting state is realized, which is the most important evidence for the realization of the spin-fluctuation-mediated superconductivity.

In this thesis, we study the superconducting state of iron pnictides by focusing on the gap structures. In order to understanding pairing mechanisms, we make realistic three dimensional multiorbital model of  $\text{KFe}_2\text{Se}_2$ ,  $\text{LiFeAs}$ , and  $\text{BaFe}_2(\text{As,P})_2$ . Next, we calculate the gap structures when both the spin fluctuations and orbital fluctuations are developed. Finally, we clarify the superconducting mechanism of iron based superconductivity by comparing the numerical results with the experimental results.

## 1.2 Typical $T$ - $x$ (doping rate) phase diagram

Figure 1 shows typical  $T$ - $x$  (doping rate) phase diagram of iron pnictides. Mother compounds of most iron pnictides show the antiferromagnetism and do not show superconductivity. When carrier doping or isovalent doping is induced, superconductivity is realized. In the underdoped regime, the

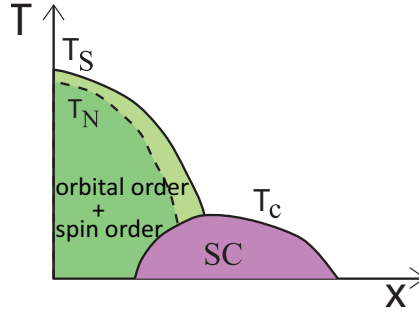


Figure 1: A typical phase diagram for Fe-based superconductors.  $T_S$  is the structure transition temperature, which is expected to be induced by orbital polarization  $n_{xz} > n_{yz}$  according to the ARPES measurements and the sizable softening of  $C_{66}$ .  $T_N$  is the magnetic transition temperature. Reprinted from Ref.[16]. ©2013 by the American Physical Society.

second-order orthorhombic structural transition occurs at  $T_S$  and striped type magnetic order is realized at  $T_N \lesssim T_S$ . In the orthorhombic phase, the Fe  $d$ -orbital polarization  $n_{xz} \neq n_{yz}$  is realized, where  $n_{xz(yz)}$  is the filling of  $d_{xz(yz)}$  orbital[17]. Also, sizable softening of shear modulus  $C_{66}$  [18, 19, 20] and the renormalization of phonon velocity [21] indicate the development of orbital fluctuations near the orthorhombic phase. Strong spin fluctuations are also observed near the magnetic ordered phase. Next to the structural transition, the SC phase appears. Thus, the phase diagram in fig. 1 (a) indicates that both orbital and spin fluctuations could be closely related to the mechanisms of superconductivity. Up to now, pairing mechanism of iron pnictides had been studied from aspects of development of both the spin fluctuations and orbital fluctuations based on multiorbital models.

### 1.3 Crystal structures

Iron pnictides are classified into some groups by crystal structures. However, conductive layer of all type of the structures is same and composed of Fe and pnictogen. Figure 2 (a) shows the overhead view of conducting layer. Fe is located in same plane and + (–) in  $Pn$  means the pnictogen is located above (under) the Fe plane.

Figure 2 (b) shows the crystal structure of LaFeAsO, which is called

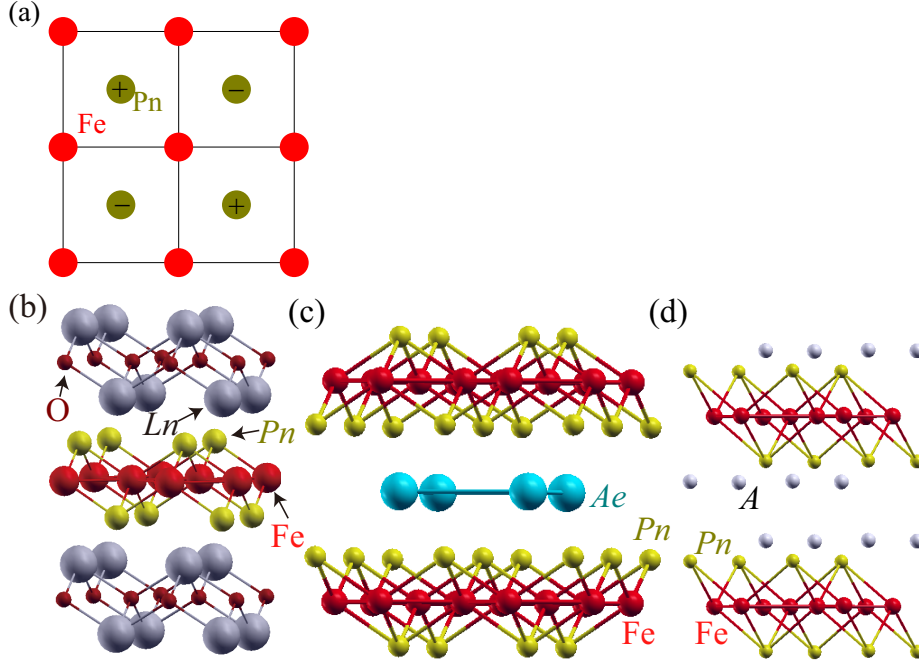


Figure 2: (a) Overhead view of conducting layer of iron pnictides. Fe is located in same plane. + (−) in  $Pn$  means the pnictogen is located above (under) the Fe plane. (b)-(d) Crystal structures of (b)  $LnFePnO$  (1111 system), (c)  $AeFe_2Pn_2$  (122 system), and (d)  $AFePn$  (111 system).

1111 system because of the elemental ratio. All Fe is located in same plane and pnictogen is located tetrahedrally above and under the Fe plane. The mother compound  $LaFeAsO$  is antiferromagnetism. However, when O is substituted for F and electron is doped, the antiferromagnetism is broken and superconductivity is realized. The compound which has the most highest  $T_c$  ( $\sim 55K$ ) in iron pnictides is comprised in 1111 system.

Figure 2 (c) shows the crystal structure of  $BaFe_2As_2$ , which is called 122 system. The conductive layer is same as 1111 system. However insulated layer is comprised of only alkali earth elements. Same as 1111 system, the mother compound  $BaFe_2As_2$  is antiferromagnetism. When Ba is substituted for K (hole is doped), Fe is substituted for Co (electron is doped), or As is substituted for P (chemical pressure is added), the antiferromagnetism is broken and superconductivity is realized. In 122 system, high quality and

large single crystal can be synthesized and numerous measurements had been conducted. Therefore, 122 system is important for understanding entire iron pnictides.

Figure 2 (d) shows the crystal structure of LiFeAs, which is called 111 system. Unlike in the case of 1111 or 122 system, LiFeAs shows superconductivity without doping. Recently, very clean single crystal of LiFeAs is synthesized. Since measurements which are not affected by impurity can be performed, LiFeAs is significant compound for understanding the pairing mechanism of iron pnictides.

There are other groups which have no insulated layer or more complex insulated layer. However, we do not explain these groups in detail since these groups are not discussed in this thesis.

## 1.4 Electronic band structures

In this section, we explain typical electronic band structure of iron pnictides. In this thesis, we denote  $d_{z^2}$ ,  $d_{xz}$ ,  $d_{yz}$ ,  $d_{xy}$ ,  $d_{x^2-y^2}$  orbitals as 1, 2, 3, 4, 5, where  $x$ ,  $y$  axis correspond to the nearest Fe-Fe directions.

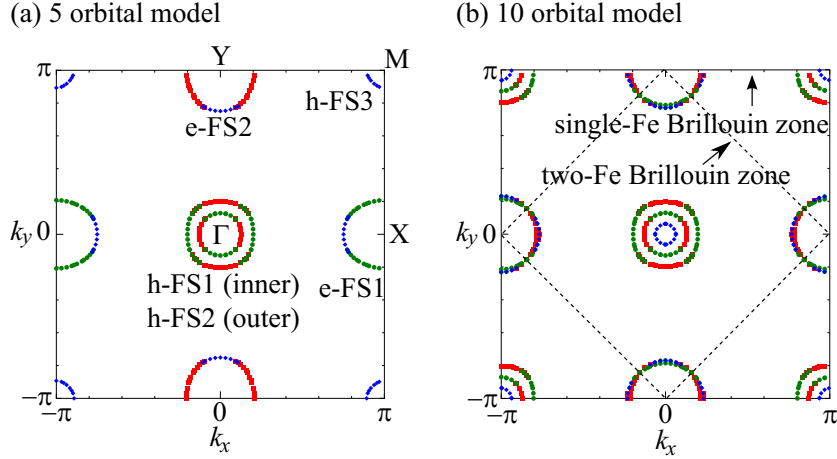


Figure 3: (a) FSs for  $n = 6.05$  in the unfolded five orbital model. (b) FSs for  $n = 6.05$  in the ten orbital model. They are mainly composed of  $d_{xz}$  (green)  $d_{yz}$  (red)  $d_{xy}$  (blue).

The Fermi surfaces (FSs) for filling  $n = 6.05$  in the five orbital model



given by the first principle calculation for LaFeAsO [5] is shown in Fig. 3 (a). This is typical example of FSs of iron pnictides. The five orbital model (single Fe unit cell) is obtained by the unfolding the ten orbital model (two-Fe unit cell), which is shown in fig. 3 (b). Both models are equivalent mathematically, and the unfolding is performed by following the procedure in ref. [22].  $n = 6.05$  correspond to underdoped regime (LaFeAsO<sub>0.95</sub>F<sub>0.05</sub>). The green, red, and green colors correspond to  $d_{xz}$ ,  $d_{yz}$ , and  $d_{xy}$  orbital, respectively. There are two holelike FSs (h-FSs) at  $\Gamma$  point, electronlike FSs (e-FSs) at X and Y points, and one h-FS at M point.

In most iron pnictides, there are h-FSs at  $\Gamma$  and M points and e-FS at X and Y points, which is similar to LaFeAsO<sub>0.95</sub>F<sub>0.05</sub>, although the size or number of FSs are different.

### 1.5 Candidates of pairing mechanisms and superconductive symmetry: spin-fluctuation-mediated $s_{\pm}$ -wave state and orbital-fluctuation-mediated $s_{++}$ -wave state

Just after the discovery of Fe-based superconductors, the spin-fluctuation-mediated  $s$ -wave with sign reversal ( $s_{\pm}$ -wave) between h-FSs and e-FSs had been proposed based on the band calculation [23] and the random phase approximation (RPA) [5, 24, 25]. Spin-fluctuation-mediated unconventional superconductivity is believed to be realized in various metals, such as high- $T_c$  cuprates [26, 27, 28],  $\kappa$ -(BEDT-TTF)<sub>2</sub>X [29, 30, 31], and CeMIn<sub>5</sub> ( $M$ =Co,Rh,Ir) [32].

In principle, spin-fluctuation-mediated superconductivity is fragile against nonmagnetic impurities or randomness, since the SC gap function has sign changes inevitably. This is also true for iron pnictides, although the FSs are disconnected and the SC gap is fully-gapped. According to Ref. [9, 10], decrease in  $T_c$  per  $\rho_{\text{imp}} = 1\mu\Omega\text{cm}$  reaches  $\sim 1\text{K}$  *independently of the impurity potential strength*. Contrary to this expectation, the SC state is very robust against various impurities [7, 8] and heavy-particle irradiations [33]. Moreover, the spin-fluctuation-mediated superconductors are expected to show a “resonance peak” in the neutron inelastic scattering as a reflection of sign-change in the SC gap. However, the observed “resonance-like” peak structure in iron pnictides [34, 35, 36] is reproduced theoretically by considering the strong correlation effect via quasiparticle damping, even in

the conventional  $s$ -wave state without sign reversal ( $s_{++}$ -wave state) [37].

In  $\text{BaFe}_2(\text{As}_{1-x}\text{P}_x)_2$ ,  $T_c$  increases as  $x$  decreases till the lattice structure transition occurs at  $x = 0.27$ , and  $T_c$  is positively correlated to the spin-fluctuation strength for  $x \geq 0.33$  [38]. On the other hand,  $T_c$  in  $\text{LaFeAsO}_{1-x}\text{F}_x$  at  $x = 0.14$  increases from 26 K to 43 K by applying the pressure, whereas spin-fluctuation strength observed by  $1/T_1T$  measurement is almost unchanged [39]. Thus, the correlation between the spin-fluctuation strength and  $T_c$  seems to depend on compounds.

Considering these difficulties in the  $s_{\pm}$ -wave scenario, the orbital fluctuation-mediated  $s_{++}$ -wave state had been proposed [6, 13]. The phase diagram explained in sec. 1.2 indicate the development of orbital fluctuations. In Refs. [6, 40, 41, 42, 43] the authors have shown that small quadrupole interaction induced by Fe-ion oscillations gives rise to the large antiferro- and ferro-orbital fluctuations. Also, in Refs. [13, 14], the authors had developed the *spin+orbital* fluctuation theory in multiorbital Hubbard model by including the VCs to the susceptibilities, which are neglected in the RPA. It was found that the Aslamazov-Larkin type VC due to Coulomb interaction produces large effective quadrupole interaction. The emergence of the orbital fluctuations due to the VC is also recognized in a simple two-orbital model, using the self-consistent VC method [44] as well as newly developed two-dimensional renormalization group method (RG+cRPA method) [45].

## 1.6 Orbital-spin fluctuation theory

In this subsection, we introduce the orbital fluctuation theory to avoid the difficulties in the  $s_{\pm}$ -wave scenario described in previous subsection.

### 1.6.1 Interaction terms

We introduce both the coulomb interaction and quadrupole interaction. Coulomb interaction is comprised of intraorbital Coulomb  $U$ , interorbital Coulomb  $U'$ , Hund's coupling  $J$ , and pair hopping  $J'$ ; [5]

$$\begin{aligned}
 H_{\text{Coulomb}} = & \sum_a^{\text{site}} \left( U \sum_l n_{al\uparrow} n_{al\downarrow} + U' \sum_{l>m} \sum_{\sigma\sigma'} n_{al\sigma} n_{am\sigma'} \right. \\
 & \left. - J \sum_{l \neq m} \mathbf{S}_{al} \cdot \mathbf{S}_{am} + J' \sum_{l \neq m} c_{al\uparrow}^\dagger c_{al\downarrow}^\dagger c_{am\downarrow} c_{am\uparrow} \right), \quad (1)
 \end{aligned}$$

where  $a$  denotes the site, and  $l, m$  are the five  $d$ -orbitals.

In addition to the Coulomb interaction, we introduce quadrupole interaction. Quadrupole interaction is induced by the electron-phonon ( $e$ -ph) interaction due to Fe ion oscillations as follows, [6]

$$V_{\text{quad}} = -g_1(\omega_l) \sum_a^{\text{site}} \left( \hat{O}_{yz}^a \cdot \hat{O}_{yz}^a + \hat{O}_{xz}^a \cdot \hat{O}_{xz}^a \right) - g_2(\omega_l) \sum_a^{\text{site}} \left( \hat{O}_{xy}^a \cdot \hat{O}_{xy}^a \right), \quad (2)$$

where  $g_i(\omega_l) = g_i \omega_0^2 / (\omega_l^2 + \omega_0^2)$ , and  $g_i = g_i(0)$  is the quadrupole interaction at  $\omega_l = 0$ .  $\omega_0$  is the cutoff energy of the quadrupole interaction. The operator  $\hat{O}_\Gamma^a$  ( $\Gamma = xz, yz, xy$ ) is given as

$$\hat{O}_\Gamma^a = \sum_{l,m} o_\Gamma^{l,m} \hat{m}_{l,m}^a, \quad (3)$$

( $\hat{m}_{l,m}^a = \sum_\sigma c_{l\sigma}^\dagger(\mathbf{R}_a) c_{m\sigma}(\mathbf{R}_a)$ ) is the quadrupole operator at site  $\mathbf{R}_a$ . The coefficient is defined as  $o_{xz}^{l,m} = 7\langle l|\hat{x}\hat{z}|m\rangle$  for  $\Gamma = xz$ , where  $\hat{x} = x/r$  and so on. [40] The non-zero coefficients of  $o_\Gamma^{l,m} = o_\Gamma^{m,l}$  are given as [40]

$$o_{xz}^{2,5} = o_{xz}^{3,4} = \sqrt{3}o_{xz}^{1,2} = 1, \quad (4)$$

$$-o_{yz}^{3,5} = o_{yz}^{2,4} = \sqrt{3}o_{yz}^{1,3} = 1, \quad (5)$$

$$-o_{xy}^{2,3} = -\sqrt{3}o_{xy}^{1,4} = 1. \quad (6)$$

Thus,  $\hat{V}_{\text{quad}}$  has many non-zero inter-orbital elements. As explained in Ref. [6],  $g_1$  ( $g_2$ ) is induced by in-plane (out-plane) Fe-ion oscillations. Also, the Aslamazov-Larkin type VC (AL-VC) due to Coulomb interaction produces large effective quadrupole interaction  $g_1$  [13]. Thus, the quadrupole interaction in eq. (2) is derived from both the VC and  $e$ -ph interaction.

### 1.6.2 Spin and orbital fluctuations

In this section, we perform the RPA for the model given in sec. 1.4 by using  $64 \times 64$   $\mathbf{k}$  meshes and 2048 Matsubara frequencies. We fix the temperature at  $T = 0.02$  eV, and set the filling of each Fe-site as  $n = 6.0$ . Hereafter, the unit of energy as eV. The irreducible susceptibility in the five-orbital model is given by

$$\chi_{ll',mm'}^0(q) = -\frac{T}{N} \sum_k G_{l,m}^0(k+q) G_{m',l'}^0(k), \quad (7)$$

where  $q = (\mathbf{q}, \omega_l)$  and  $k = (\mathbf{k}, \epsilon_n)$ .  $\epsilon_n = (2n + 1)\pi T$  and  $\omega_l = 2l\pi T$  are the fermion and boson Matsubara frequencies.  $\hat{G}^0(k) = [i\epsilon_n + \mu - \hat{h}_{\mathbf{k}}^0]^{-1}$  is the Green function in the orbital basis, where  $\hat{h}_{\mathbf{k}}^0$  is the matrix representation of  $\hat{H}^0$  and  $\mu$  is the chemical potential. In the RPA, the susceptibilities for spin and charge sectors are given by [46]

$$\hat{\chi}^s(q) = \frac{\hat{\chi}^0(q)}{\hat{1} - \hat{\Gamma}^s \hat{\chi}^0(q)}, \quad (8)$$

$$\hat{\chi}^c(q) = \frac{\hat{\chi}^0(q)}{\hat{1} - \hat{\Gamma}_g^c(\omega_l) \hat{\chi}^0(q)}, \quad (9)$$

where

$$(\Gamma^s)_{l_1 l_2, l_3 l_4} = \begin{cases} U, & l_1 = l_2 = l_3 = l_4, \\ U', & l_1 = l_3 \neq l_2 = l_4, \\ J, & l_1 = l_2 \neq l_3 = l_4, \\ J', & l_1 = l_4 \neq l_2 = l_3, \\ 0, & \text{otherwise} \end{cases} \quad (10)$$

$$\hat{\Gamma}_g^c(\omega_l) = \hat{\Gamma}^c - 2\hat{V}_{\text{quad}}(\omega_l), \quad (11)$$

$$(\hat{\Gamma}^c)_{l_1 l_2, l_3 l_4} = \begin{cases} -U, & l_1 = l_2 = l_3 = l_4, \\ U' - 2J, & l_1 = l_3 \neq l_2 = l_4, \\ -2U' + J, & l_1 = l_2 \neq l_3 = l_4, \\ -J', & l_1 = l_4 \neq l_2 = l_3, \\ 0, & \text{otherwise} \end{cases} \quad (12)$$

Hereafter, we assume  $J = J'$  and  $U = U' + 2J$  and fix the ratio  $J/U = 1/6$ .

In the RPA, the enhancement of the spin susceptibility  $\hat{\chi}^s$  is mainly caused by the intra-orbital Coulomb interaction  $U$ , using the “intra-orbital nesting” of the FSs. On the other hand, the enhancement of  $\hat{\chi}^c$  in the present model is caused by the quadrupole-quadrupole interaction in eq. (2), utilizing the “inter-orbital nesting” of the FSs. Figure 4 shows the  $U$ - $g(0)$  phase diagram for  $n = 6.1$ .  $\alpha_{s(c)}$  is the spin (charge) Stoner factor, which is given the maximum eigenvalue of  $\hat{\Gamma}^s \hat{\chi}^0(\mathbf{q}, 0)$  ( $\hat{\Gamma}_g^c(0) \hat{\chi}^0(\mathbf{q}, 0)$ ). The magnetic (orbital) order is realized when the spin (charge) Stoner factor is unity. For  $n = 6.1$ , the critical value of  $U$  is  $U_{\text{cr}} = 1.27$  eV, and the critical value of  $g$  is  $g_{\text{cr}} = 0.23$  eV for  $U = 0$ .

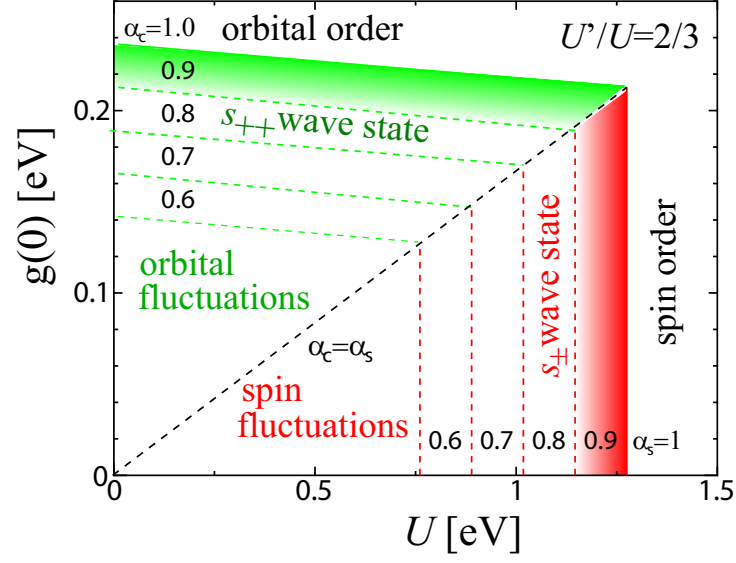


Figure 4: Obtained  $U$ - $g(0)$  phase diagram for  $n = 6.1$ . Near the orbital-density-wave boundary,  $s_{++}$ -wave SC state is realized by orbital fluctuations. Reprinted from Ref.[41]. ©2010 by the American Physical Society.

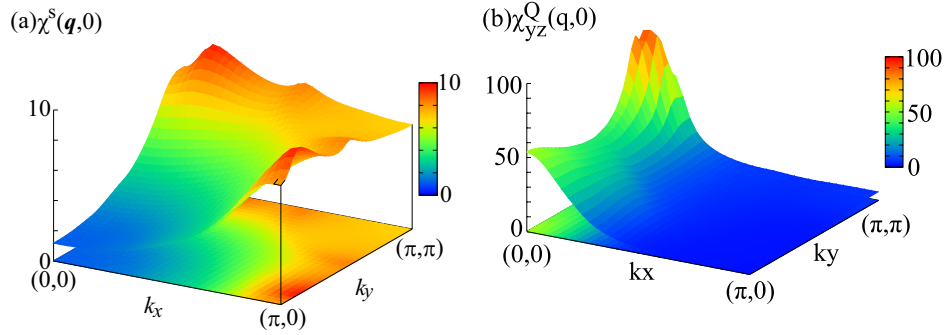


Figure 5: Obtained (a)  $\chi^s(\mathbf{q}, 0)$  and (b)  $\chi^Q_{yz}(\mathbf{q}, 0)$ , for  $n = 6.1$ ,  $U = 1$ ,  $g_1 = g_2 = 0.216$ , and  $T = 0.02$ . Note that  $\chi^Q_{xz}(\mathbf{q}', 0) = \chi^Q_{yz}(\mathbf{q}, 0)$ , where  $\mathbf{q}'$  is given by the rotation of  $\mathbf{q}$  by  $\pi/2$ .

Figure 5 (a) shows the obtained spin susceptibility

$$\chi^s(\mathbf{q}, 0) \equiv \sum_{l,m} \chi^s_{l,l:m,m}(\mathbf{q}, 0), \quad (13)$$

given by the RPA for  $U = 1$  and  $g_1 = g_2 = 0.216$ . The spin Stoner factor is  $\alpha_s = 0.79$ . The spin susceptibility has peaks around  $(\pi, 0), (0, \pi)$  due to the intra- $d_{xz,yz}$ -orbital nesting between h-FS1,2 and e-FS1,2, and also has a rigidlike structure  $(\pi, \pi/2)$  to  $(\pi/2, \pi)$  caused by the intra- $d_{xy}$ -orbital nesting between h-FS3 and e-FS1,2.

Figure 5 (b) shows the quadrupole susceptibility

$$\chi_\Gamma^Q(\mathbf{q}, 0) = \sum_{l,l',m,m'} o_\Gamma^{l,l'} \chi_{l,l':m,m'}^c(\mathbf{q}, 0) o_\Gamma^{m',m}, \quad (14)$$

for the channel  $\Gamma = yz$ . given by the RPA for  $U = 1$  and  $g_1 = g_2 = 0.216$ . The charge Stoner factor is  $\alpha_c = 0.98$ . In this model, both  $\chi_{yz}^Q(0, \pi)$  and  $\chi_{xz}^Q(\pi, 0)$  are the most divergent channels. For  $\Gamma = yz$ , the dominant contribution comes from  $\chi_{2,4;4,2}^c(0, \pi) \approx \chi_{2,4;2,4}^c(0, \pi)$ , due to the inter-orbital nesting (orbital 2 and 4) between h-FS1,2 and e-FS2. Its second largest peak near  $(0, 0)$  originate from forward scattering in the e-FS1 that composed of  $d_{xz}$  and  $d_{xy}$ .

### 1.7 $s_{++}$ and $s_{\pm}$ -wave superconducting gap functions

In this subsection, we analyze the following linearized Eliashberg equation using the RPA by taking account of both the spin and orbital fluctuations on the equal footing [46]:

$$\lambda_E \Delta_{ll'}(k) = \frac{T}{N} \sum_{k', m_i} W_{lm_1, m_4 l'}(k - k') G_{m_1 m_2}^0(k') \Delta_{m_2 m_3}(k') G_{m_4 m_3}^0(-k'), \quad (15)$$

where,

$$\hat{W}(q) = -\frac{3}{2} \hat{\Gamma}^s \hat{\chi}^s \hat{\Gamma}^s + \frac{1}{2} \hat{\Gamma}^c \hat{\chi}^c \hat{\Gamma}^c - \frac{1}{2} (\hat{\Gamma}^s - \hat{\Gamma}^c), \quad (16)$$

for the singlet states.  $\lambda_E$  is the eigenvalue of the gap equation, which approaches unity as  $T \rightarrow T_c$ . Hereafter, we use  $64^2$   $\mathbf{k}$  meshes, and 2048 Matsubara frequencies. We perform the calculation at relatively high temperatures ( $T \geq 0.02$ ) since the number of meshes is not enough for  $T < 0.02$ .

Figure 6 (a) and (b) show the SC gap on the FSs in the band representation for  $U = 1.09$  and  $U = 1.10$ , respectively. We put  $n = 6.1$ ,  $T = 0.02$ ,  $\omega_D = 0.02$ , and  $g_1 = g_2 = 0.21$ , which correspond to  $\alpha_c = 0.98$ . The horizontal axis is the azimuth angle for  $\mathbf{k}$  point with the origin at  $\Gamma$  (Y) point for

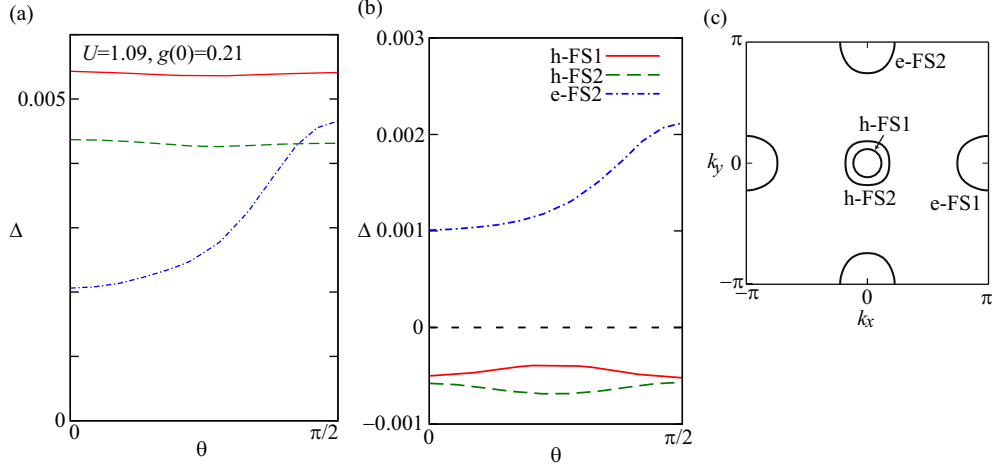


Figure 6: (a) (b) Obtained SC gap functions for (a)  $U = 1.09$  and (b)  $U = 1.10$ , respectively. We put  $g_1 = g_2 = 0.21$  ( $\alpha_c = 0.98$ ),  $T = 0.02$ , and  $\omega_D = 0.02$ . They are normalized as  $N^{-1} \sum_{\mathbf{k}, lm} |\Delta_{lm}(\mathbf{k})|^2 = 1$ . We use 2048 Matsubara frequencies. (c) FSs in the unfolded Brillouin zone for  $n = 6.1$ . Note that h-FS3 disappears for  $n = 6.1$ . Reprinted from Ref.[41]. ©2010 by the American Physical Society.

h-FS1,2 (e-FS2). For  $U = 1.09$ , the  $s_{++}$  state is realized by orbital fluctuations [6]. On the other hand, the  $s_{\pm}$  state is realized for  $U = 1.10$  since the spin fluctuations dominate the orbital fluctuations.

## 1.8 The contents of this thesis

In the study of the pairing mechanism, the  $\mathbf{k}$ -dependence of gap function offers us very useful information. Up to now, detailed gap structures of various iron based superconductors are measured by angle resolved photoemission spectroscopy (ARPES). In this thesis, we studied the various iron pnictides of gap functions theoretically in order to obtain a significant information of pairing mechanism.

In sec. 2, we study the iron-selenium 122-structure compound  $\text{KFe}_2\text{Se}_2$  with  $T_c \sim 30\text{K}$ . In this heavily electron doped system, h-FSs disappear and isotropic SC gap is observed by both ARPES[47, 48, 49] and specific heat measurements [50]. Thus, the study of gap structure of  $\text{KFe}_2\text{Se}_2$  will give us

important information to reveal the pairing mechanism of iron pnictides.

In sec. 3, we study LiFeAs. For studying the pairing mechanism, LiFeAs is favorable since very clean single crystals can be synthesized and intrinsic gap structure free from the impurity effect can be obtained. Recently, ARPES measurements show the spin-orbit interaction (SOI) is very important in LiFeAs. [51, 52] Therefore, we also calculate the gap structures considering SOI.

In sec. 4, we study the origin of the nodal gap structure observed by experiments [53, 54] for  $\text{BaFe}_2(\text{As,P})_2$ . When either spin or orbital fluctuations develop alone, full gap  $s$ -wave state is realized. Therefore, the nodal gap structure cannot be reproduced. However, by considering combination of orbital and spin fluctuations, we reproduce the nodal gap structures of  $\text{BaFe}_2(\text{As,P})_2$ .



## 2 Heavily electron doped compound ( $\text{KFe}_2\text{Se}_2$ )

### 2.1 Introduction for $\text{KFe}_2\text{Se}_2$

Recently, iron-selenium 122-structure compound  $A_x\text{Fe}_2\text{Se}_2$  ( $A = \text{K}, \text{Rb}, \text{Cs}$ ) with  $T_c \sim 30$  K was discovered [55]. This heavily electron-doped superconductor has been attracting great attention since both the band calculations [56, 57] and ARPES measurements [47, 48, 49] indicate the absence of h-FSs. NMR measurements report the weakness of spin fluctuations [58], and both ARPES [47, 48, 49] and specific heat measurements [50] indicate the isotropic SC gap. Thus, study of  $A_x\text{Fe}_2\text{Se}_2$  will give us important information to reveal the pairing mechanism of iron pnictides.

The unit-cell of iron-based superconductors contains two Fe atoms. However, except for 122-systems, one can construct a simple “single-Fe model” from the original “two-Fe model” by applying the gauge transformation on  $d$ -orbitals [22]. By this procedure, the original Brillouin zone (BZ) is enlarged to the “unfolded BZ”. Based on the single-Fe model, spin-fluctuation-mediated  $d$ -wave state ( $B_{1g}$  representation) “without nodes” had been proposed [59, 60, 61], by paying attention to the nesting between e-FSs. However, we cannot construct a “single-Fe model” for 122 systems since finite hybridization between e-FSs prevents the unfolding procedure [22]. Therefore, theoretical study based on the original two-Fe model is highly desired to conclude the gap structure.

In this section, we study the ten-orbital (two Fe atoms) for  $\text{KFe}_2\text{Se}_2$  by considering both the Coulomb interaction and quadrupole interaction using the RPA. When the Coulomb interaction is large, we obtain the  $d$ -wave SC state due to the spin fluctuations, as predicted by the recent theoretical studies in the single-Fe Hubbard models [59, 60, 61]. However, the gap function on the FSs inevitably has “nodal structure” in the two-Fe model, due to the symmetry requirement of the body-centered tetragonal lattice. On the other hand, orbital-fluctuation-mediated  $s_{++}$ -wave state is realized by quadrupole interaction; Since the nodal SC state is fragile against randomness, study of impurity effect will be useful to distinguish these SC states.

## 2.2 Tight binding model of $\text{KFe}_2\text{Se}_2$

We perform the local-density-approximation (LDA) band calculation for  $\text{KFe}_2\text{Se}_2$  using Wien2k code based on the experimental crystal structure [55]. Next, we derive the ten-orbital tight-binding model that reproduces the LDA band structure and its orbital character using Wannier90 code and Wien2Wannier interface [62]. The dispersion of the model and the primitive BZ are shown in Figs. 7 (a) and (b).

In Fig. 7, we show the FSs of  $\text{KFe}_2\text{Se}_2$  for (c)  $k_z = 0$  and (d)  $k_z = \pi/2$  planes when the electron number per Fe-ion is  $n = 6.5$ : On each plane, there are four large and heavy e-FSs around X and Y points, and one small and light e-FSs around Z point. For  $n = 6.5$ , the energy of the h-band at  $\Gamma$  point from the Fermi level,  $E_h$ , is about  $-0.07$  eV. Since the obtained FS topology and the value of  $E_h$  are consistent with recent reports by ARPES measurements [47, 48, 49], we study the case  $n = 6.5$  hereafter. In the present BZ in (b),  $\Gamma$  and Z points and X and Y points in (c) are not equivalent, and  $k_z = \pi$  plane is given by shifting (c) by  $(\pi, \pi)$ . As for (d), T and T' points and P and P' points are equivalent. Therefore the reciprocal wave vector on the  $k_z = \pi/2$  plane is  $(\pi, \pi)$  and  $(\pi, -\pi)$ . The diamond-shaped shadows in the  $k_z = \pi/2$  plane indicates the sign of basis function for  $B_{1g}$  ( $x^2 - y^2$ -type) representation, which has nodes on the P-P' line on both FS1 (inner FS) and FS2 (outer FS).

To confirm the existence of nodes, we verify that FS1 and FS2 in  $\text{KFe}_2\text{Se}_2$  are largely hybridized. In fact, the weights of  $d$ -orbitals on FS1,2 given in Fig. 7 (e) are smooth functions of  $\theta$ , which is the strong evidence for the hybridization in wide momentum space. This hybridization disappears when inter-layer hoppings are neglected: Then, both  $xy(\text{FS1})$  and  $xy(\text{FS2})$  show cusps at  $\theta = \pi/4$ , and  $xz(\text{FS2})$  suddenly drops to almost zero for  $\theta \geq \pi/4$ . In Fig. 7 (f), we explain the origin of nodal gap based on the fully-gapped  $d$ -wave solution in the single-Fe model [59, 60, 61]: By introducing inter-layer hoppings, two elliptical e-FSs with positive and negative  $\Delta$  in the unfolded BZ are hybridized to form FS1 and 2 with four-fold symmetry. As a result, nodal lines inevitably emerge on FS1 and 2, at least near the  $|k_z| = \pi/2$  plane.

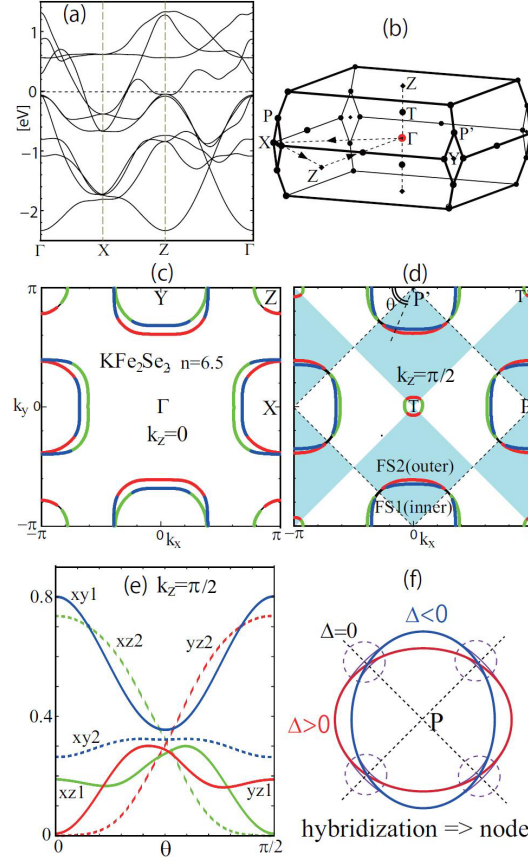


Figure 7: (a) Dispersion of the present ten-orbital model for  $\text{KFe}_2\text{Se}_2$ .  $\Gamma$ ,  $X$ , and  $Z$  points are on the  $k_z = 0$  plane. (b) Primitive BZ for body-centered tetragonal lattice. (c)(d) FSs on the  $k_z = 0$  plane and  $k_z = \pi/2$  plane. The green, red, and blue lines correspond to  $xz$ ,  $yz$ , and  $xy$  orbitals, respectively. The diamond-shaped shadows in (d) indicates the sign of basis function for  $B_{1g}$  representation. (e) Weight of each orbital on the inter FS (FS1) and the outer FS (FS2) as function of  $\theta$ ;  $\theta$  is shown in (d). (f) Hybridization between two e-pockets in 122 systems should create the nodal  $d$ -wave gap. Reprinted from Ref.[42]. ©2011 by the American Physical Society.

### 2.3 Random phase approximation

In this section, we perform the RPA for the present model as described in sec. 1.6, by using  $64 \times 64$   $\mathbf{k}$  meshes and 512 Matsubara frequencies.

In the RPA, the enhancement of the spin susceptibility  $\hat{\chi}^s$  is mainly caused by the intra-orbital Coulomb interaction  $U$ , using the “intra-orbital nesting” of the FSs. On the other hand, the enhancement of  $\hat{\chi}^c$  in the present model is caused by the quadrupole-quadrupole interaction in eq. (2), utilizing the “inter-orbital nesting” of the FSs. In this section, we set  $g_1 = g_2 = g$ . The magnetic (orbital) order is realized when the spin (charge) Stoner factor  $\alpha_{s(c)}$ , which is the maximum eigenvalue of  $\hat{\Gamma}^s \hat{\chi}^0(\mathbf{q}, 0)$  ( $\hat{\Gamma}_g^c(0) \hat{\chi}^0(\mathbf{q}, 0)$ ), is unity. For  $n = 6.5$  and  $k_z = 0$ , the critical value of  $U$  is  $U_{\text{cr}} = 1.18$  eV, and the critical value of  $g$  is  $g_{\text{cr}} = 0.23$  eV for  $U = 0$ . These values change only  $\sim 2\%$  for different  $k_z$ . The obtained  $U$ - $g$  phase diagram is very similar to Fig. 4, irrespective of the absence of h-FSs in  $\text{KFe}_2\text{Se}_2$ . The reason would be (i) the density-of-states (DOS) in  $\text{KFe}_2\text{Se}_2$  is about  $1\text{eV}^{-1}$  per Fe, which is comparable with other iron pnictides, and (ii) the nesting between e-FSs is rather strong because of their square-like shape.

Figure 8 (a) shows the total spin susceptibility  $\chi^s(\mathbf{q}, 0)$  at  $U = 1.1$  eV and  $g_1 = g_2 = 0$  for  $k_z = 0$  plane.  $\chi^s$  is given by the intra-orbital nesting, and its peak position is  $\mathbf{q} \approx (\pi, 0.4\pi)$ , consistently with previous studies [59, 60, 61]. The obtained incommensurate spin correlation is the origin of the  $d$ -wave SC gap. Figure 8 (b) shows the off-diagonal orbital susceptibility  $\chi_{yz,xy;yz,xy}^c(\mathbf{q}, 0)$  for the  $k_z = 0$  plane at  $U = 0$  and  $g_1 = g_2 = 0.22$  eV. It is derived from the inter-orbital nesting between  $xz$  and  $xy$ , and its peak position is  $\mathbf{q} \approx (0.7\pi, 0.4\pi)$ . Note that the peak position of  $\chi_{xz,xy;xz,xy}^c$  is  $\mathbf{q} \approx (0.4\pi, 0.7\pi)$ . The obtained strong spin- and orbital-correlations are the origin of the  $d$ -wave and  $s_{++}$ -wave SC states.

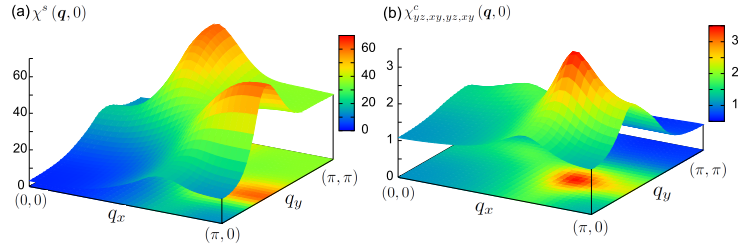


Figure 8: (a)  $\chi^s(\mathbf{q}, 0)$  for  $U = 1.1$  eV and  $g_1 = g_2 = 0$ , and (b)  $\chi_{yz,xy;yz,xy}^c(\mathbf{q}, 0)$  for  $U = 0$  and  $g_1 = g_2 = 0.22$  eV. Reprinted from Ref.[42]. ©2011 by the American Physical Society.

## 2.4 Eliashberg gap equation

In this section, we analyze the linearized Eliashberg equation eq. (15). In the actual calculation results shown below, we take  $64 \times 64$   $\mathbf{k}$ -point meshes and 512 Matsubara frequencies. First, we study the spin-fluctuation-mediated SC state for  $U \lesssim U_c$  by putting  $g = 0$ . Figures 9 (a)-(c) show the gap functions of the  $d$ -wave solution at  $T = 0.03$  eV for  $k_z = 0, \pi/4$ , and  $\pi/2$ , respectively. In case of  $U = 1.1$  eV, the eigenvalue  $\lambda_E$  is 0.61 for (a), 0.63 for (b), and 0.62 for (c); the relation  $\lambda_E \geq 1$  corresponds to the SC state. They are relatively small since the SC condensation energy becomes small when the SC gap has complicated nodal line structure. On the (c)  $k_z = \pi/2$  plane, the nodal lines are along  $\theta = \pi/4$  and  $3\pi/4$  directions, consistently with the basis of  $B_{1g}$  representation in Fig. 7 (d). These nodes move to near the BZ boundary,  $\theta = 0$  and  $\pi$ , on the (b)  $k_z = \pi/4$  plane, and they deviate from the FSs on the (a)  $k_z = 0$  plane. As results, the nodal gap appears for  $\pi/4 < |k_z| < 3\pi/4$  in the whole BZ  $|k_z| \leq \pi$ .

We also obtain the  $s_{\pm}$ -wave state, with the sign reversal of the SC gap between e-FS and the “hidden h-FS below the Fermi level” given by the valence bands 5,6. The obtained solution is shown in Fig. 9 (d) for  $k_z = \pi/2$ . Interestingly, the obtained eigenvalue is  $\lambda_E = 0.99$  for  $U = 1.1$  eV, which is larger than  $\lambda_E$  for  $d$ -wave state in Fig. 9 (a)-(c). Such large  $\lambda_E$  originates from the scattering of Cooper pairs between e-FSs and the “hidden h-FS”, which was discussed as the “valence-band Suhl-Kondo (VBSK) effect” in the study of  $\text{Na}_x\text{CoO}_2$  in Ref. [63].

Here, we analyze the  $T$ -dependence of  $\lambda_E$  based on a simple two-band model with inter-band repulsion: The set of gap equations is given by [63]  $\lambda_E \Delta_h = -V N_e L_e \Delta_e$  and  $\lambda_E \Delta_e = -V N_h L_h \Delta_h$ , where  $V > 0$  is the repulsive interaction between e- and h-FSs, and  $N_{e,h}$  is the DOS near the Fermi level. When (i) the top of the h-FS is well above the Fermi level,  $L_e = L_h = \ln(1.13\omega_c/T)$ , where  $\omega_c$  is the cutoff energy. Thus, the eigenvalue is given as  $\lambda_E = V\sqrt{N_e N_h} \ln(1.13\omega_c/T) \propto -\ln T$ , similar to single-band BCS superconductors. On the other hand, when (ii) h-pocket is slightly below the Fermi level,  $L_h = (1/2)\ln(\omega_c/|E_h|)$ , where  $E_h < 0$  is the energy of the top of h-band [63]. Thus, the eigenvalue is given as  $\lambda_E = V\sqrt{N_e N_h L_h} \sqrt{\ln(1.13\omega_c/T)} \propto \sqrt{-\ln T}$ . Therefore, in case (ii), the  $T$ -dependence of  $\lambda_E$  is much moderate. In fact, as shown in Fig. 10 (a),  $\lambda_E$  for  $d$ -wave state increases monotonically with decreasing  $T$ , while  $\lambda_E$  for  $s_{\pm}$ -wave state saturates at low temperatures. This result suggests that the  $d$ -

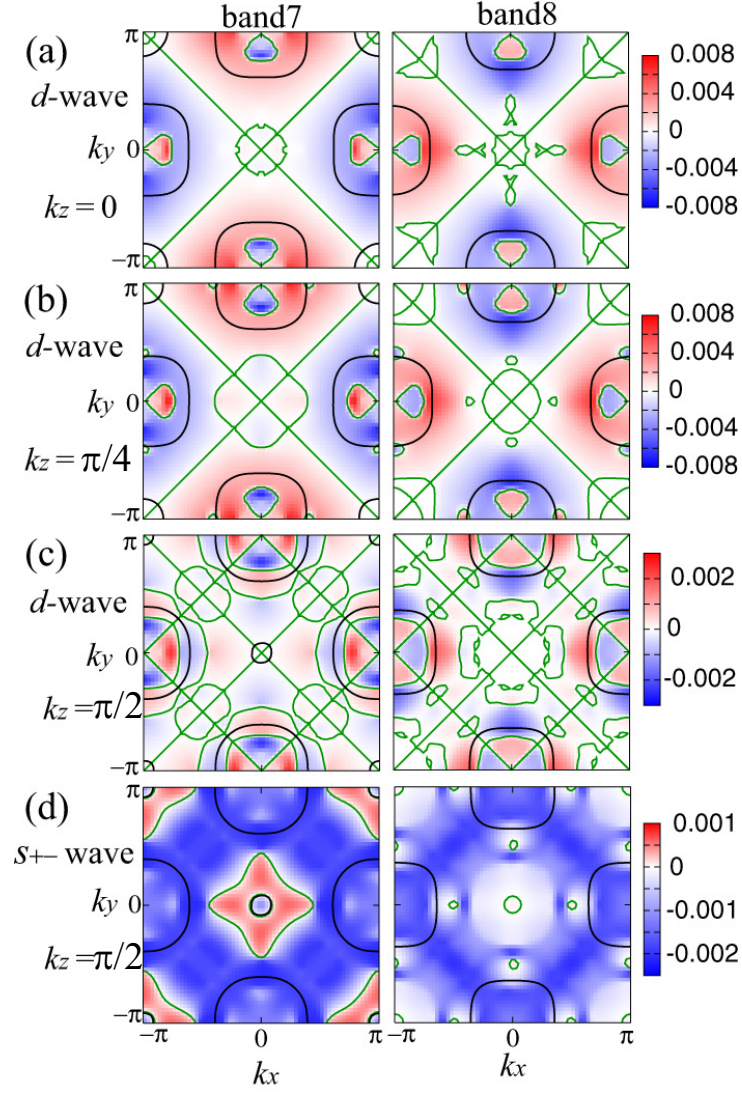


Figure 9: SC gap functions for outer FS (FS2) on band 7 and inner FS (FS1) on band 8:  $d$ -wave gap functions on the (a)  $k_z = 0$ , (b)  $k_z = \pi/4$ , and (c)  $k_z = \pi/2$  planes. Black and green lines represent the FSs and gap nodes. (d)  $s_{\pm}$ -wave gap function on the  $k_z = \pi/2$  plane. Reprinted from Ref.[42]. ©2011 by the American Physical Society.

wave state overcomes the  $s_{\pm}$ -wave state at  $T_c \sim 30\text{K}$  in  $\text{K}_x\text{Fe}_2\text{Se}_2$ . Although  $T_c$  in the  $s_{\pm}$ -wave state is  $\sim 0.06$  eV in Fig. 10 (a), it is greatly reduced by the self-energy correction that is absent in the RPA [64].

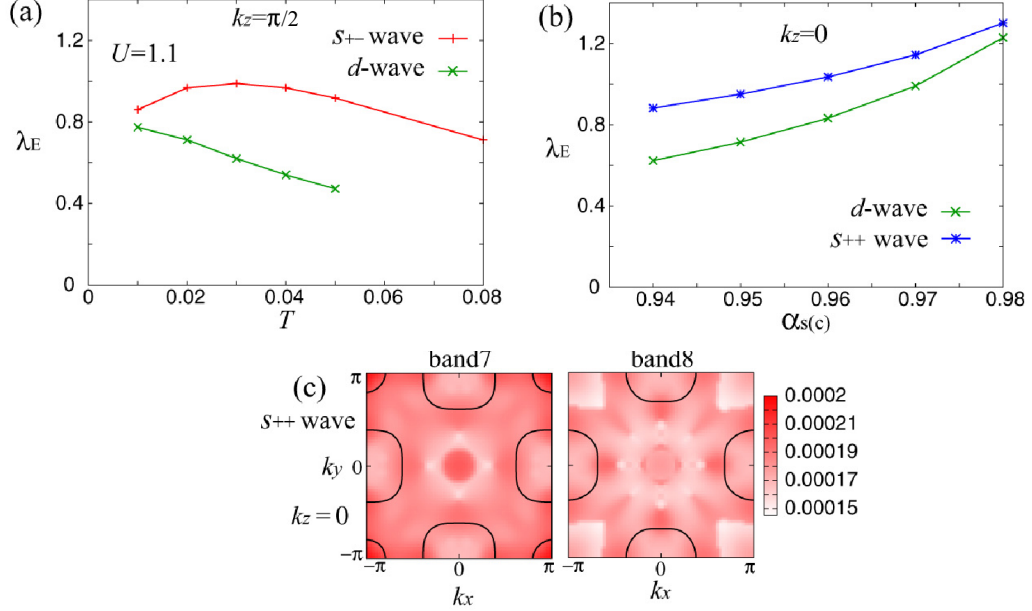


Figure 10: (a)  $T$ -dependence of  $\lambda_E$  for  $d$ - and  $s_{\pm}$ -wave states.  $\lambda_E$  at  $T = 0.01$  eV is underestimated because of the shortage of  $\mathbf{k}$ - and Matsubara-meshes. (b)  $\alpha_s$ - ( $\alpha_c$ -) dependence of  $\lambda_E$  for  $d$ -wave ( $s_{++}$ -wave) state at  $T = 0.03$  eV. (c) SC gap functions for  $s_{++}$ -wave state. Reprinted from Ref.[42]. ©2011 by the American Physical Society.

We discuss the VBSK effect for  $s_{\pm}$  wave state in more detail: According to inelastic neutron scattering measurement of  $\text{Ba}(\text{Fe},\text{Co})_2\text{As}_2$  [34, 35, 36], the characteristic spin-fluctuation energy is  $\omega_{\text{sf}} \sim 100\text{K}$  just above  $T_c \sim 30\text{K}$ . If we assume a similar  $\omega_{\text{sf}}$  in  $\text{KFe}_2\text{Se}_2$  since  $T_c$  is close, we obtain the relation  $\omega_c \sim \omega_{\text{sf}} \ll |E_h|$  in  $\text{KFe}_2\text{Se}_2$ . Since  $L_h$  is a monotonic decrease function of  $|E_h|/\omega_c$  and  $L_h < 1$  for  $-E_h/\omega_c > 0.15$ , we consider that  $d$ -wave state overcomes the  $s_{\pm}$ -wave state in  $\text{KFe}_2\text{Se}_2$ , as far as the spin-fluctuation-mediated superconductivity is considered. Although high- $T_c$   $s_{\pm}$ -wave state might be realized for  $|E_h|/\omega_c < 0.1$ , then the realized  $T_c$  will be very sensitive to  $E_h$  or the filling  $n$  [63].

Now, we study the  $s_{++}$ -wave state due to orbital fluctuations on the  $k_z = 0$  plane with  $n = 6.5$ . In Fig. 10 (b), we show the  $\alpha_c$ -dependence of  $\lambda_E$  at  $T = 0.03$  for the  $s_{++}$ -wave state with  $U = 0$ , and the  $\alpha_s$ -dependence of  $\lambda_E$  for the  $d$ -wave state with  $g_1 = g_2 = 0$ . In calculating the  $s_{++}$ -wave state, we use rather larger phonon energy;  $\omega_D = 0.15$  eV, considering that the calculating temperature is about ten times larger than the real  $T_c$ . The SC gap functions for  $s_{++}$ -wave state are rather isotropic, as shown in Fig. 10 (c). However, the obtained SC gap becomes more anisotropic in case of  $U > 0$  [64].

We stress that the RPA is insufficient for quantitative study of  $\lambda_E$  since the self-energy correction  $\Sigma$  is dropped: In Ref. [64], we have studied the present model based on the FLEX approximation, and found that the critical region with  $\alpha_c \gtrsim 0.95$  is enlarged by the inelastic scattering  $\gamma = \text{Im}\Sigma$ . Also, the  $\gamma$ -induced suppression in  $\lambda_E$  for  $d$ - or  $s_{\pm}$ -wave states is more prominent than that for  $s_{++}$ -wave state, since  $\gamma$  due to spin fluctuations is larger than that due to orbital fluctuations [64].

We found the paper by Mazin [65], in which the  $k_z$  dependence of the nodal  $d$ -wave gap in Fig. 4 corresponds to Figs. 9 (a)-(c) in this section.

## 2.5 Summary

In this section, we studied the mechanism of superconductivity in  $\text{KFe}_2\text{Se}_2$  based on the ten-orbital HH model without h-FSs. Similar to iron-pnictide superconductors, orbital-fluctuation-mediated  $s_{++}$ -wave state is realized by quadrupole interaction. We also studied the spin-fluctuation-mediated  $d$ -wave state, and confirmed that nodal lines appear on the large e-pockets, due to the hybridization between two e-FSs that is inherent in 122 systems. Therefore, careful measurements on the SC gap anisotropy is useful to distinguish these different pairing mechanisms. Study of impurity effect on  $T_c$  is also useful since  $d$ -wave (and  $s_{\pm}$ -wave) state is fragile against impurities.



### 3 Reproduction of experimental gap structure in LiFeAs

#### 3.1 Introduction for LiFeAs

LiFeAs ( $T_c = 18\text{K}$ ) is favorable for the study of pairing mechanism since very clean single crystals can be synthesized. For this reason, the intrinsic gap structure free from the impurity effect can be obtained in the case of LiFeAs. The detailed gap structure of LiFeAs had been obtained by ARPES [66, 67]. The FSs given in Ref. [66] are shown in Fig. 11 (a), which are reproduced by the ten-orbital tight-binding model (two-Fe unit cell). Figure 11 (b) shows the FSs in the five-orbital model (single Fe unit cell) obtained by unfolding the original ten-orbital model. Both models are equivalent mathematically, and the unfolding is performed by following the procedure in Ref. [22].

The bad nesting in LiFeAs between h-FSs and e-FSs attracts great attention, as an important hint to understand the variety and commonness of the pairing mechanism in Fe-based superconductors. Consistently, the observed spin fluctuations are moderate according to NMR measurements [12] and neutron scattering measurements [68, 69, 70].

In Ref. [71], the spin fluctuation mediated  $s_{\pm}$ -wave state had been studied by using the ten-orbital model for LiFeAs. The obtained gap functions on the tiny hole-pockets h-FS1 and h-FS2 in Fig. 11 (b) are very small when the filling of electrons per Fe-site is  $n = 6.0$ , although they are the largest in the ARPES measurement [66, 67] and the Scanning Tunneling Microscopy (STM) measurement [72]. Thus, it is an important challenge to verify to what extent the experimental gap structure is reproduced based on the orbital fluctuation theories.

In this section, we study the five-orbital model of LiFeAs based on the recently-developed orbital-spin fluctuation theories [6, 13]. When only the orbital fluctuations develop, the anisotropic  $s_{++}$ -wave state without sign-reversal is obtained. In this case, experimentally observed gap structure of LiFeAs, especially the largest gap experimentally observed on h-FS1 and h-FS2, is quantitatively reproduced. This is a hallmark of the orbital-fluctuation-mediated superconductivity since the spin fluctuation scenario predicts the smallest gap on h-FS1 and h-FS2. When orbital and spin fluctuations coexist, we can obtain the “hole- $s_{\pm}$ -wave state”, in which the gap structure with “sign-reversal between h-FSs” is realized. This exotic gap structure

had been discussed in (Ba,K)Fe<sub>2</sub>As<sub>2</sub> experimentally, [74, 75] and it might be realized in other Fe-based superconductors.

### 3.2 Formalism

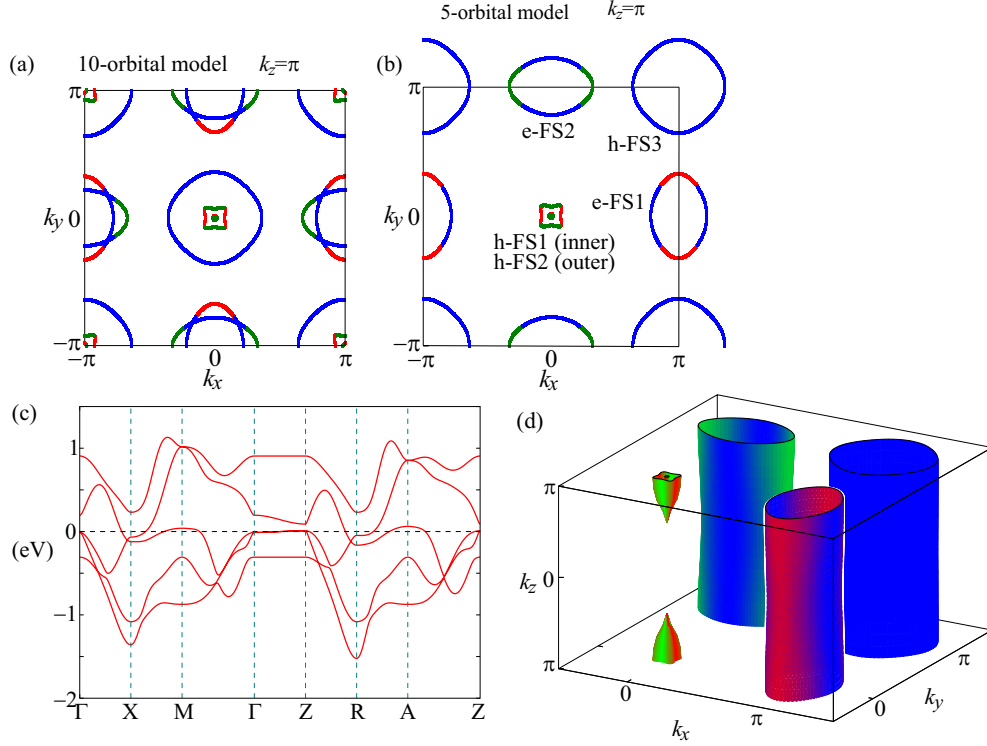


Figure 11: The FSs in the  $k_z = \pi$  plane of the three-dimensional ten-orbital model (a) and five-orbital model (b) for LiFeAs. The green, red, and blue colors correspond to  $d_{xz}$ ,  $d_{yz}$ , and  $d_{xy}$  orbitals, respectively. In (b), h-FS1,2,3 are hole-like, and e-FS1,2 are electron-like. (c) The dispersion of the band structure of the five-orbital model. (d) The three-dimensional shape of the FSs of the five-orbital model. Reprinted from Ref.[76]. ©2014 by the American Physical Society.

The three-dimensional ten-orbital tight-binding model had been obtained in Ref. [71] by fitting the experimentally observed dispersion reported in Ref.

[66], and its FSs are shown in Fig. 11 (a). In this model, the band renormalization due to the mass enhancement  $m^*/m_b \sim 2$  is taken into account. To simplify the numerical calculation, we derive the five-orbital model by unfolding the original ten-orbital model [22]. The FSs and the band dispersion of the five-orbital model are shown in Fig. 11 (b) and (c), respectively. The three-dimensional FSs of the five-orbital model are shown in Fig. 11 (d).

The kinetic term of the five orbital model is given as

$$\begin{aligned}\hat{H}^0 &= \sum_{ablm\sigma} t_{l,m}(\mathbf{R}_a - \mathbf{R}_b) c_{l\sigma}^\dagger(\mathbf{R}_a) c_{m\sigma}(\mathbf{R}_b) \\ &= \sum_{\mathbf{k}lm\sigma} \left\{ \sum_a t_{l,m}(\mathbf{R}_a) e^{i\mathbf{k} \cdot \mathbf{R}_a} \right\} c_{l\sigma}^\dagger(\mathbf{k}) c_{m\sigma}(\mathbf{k}),\end{aligned}\quad (17)$$

where  $a, b$  represent the Fe-sites,  $l, m = 1 - 5$  represent the  $d$  orbital, and  $\sigma = \pm 1$  is the spin index.  $\mathbf{R}_a$  is the position of Fe-site,  $c_{l\sigma}^\dagger(\mathbf{R}_a)$  is the creation operator of the  $d$  electron, and  $t_{l,m}(\mathbf{R}_a)$  is the hopping integral. The values of  $t_{l,m}(\mathbf{R})$  are shown in Appendix A.

Figure 12 (a) and (b) show the inverse of the Fermi velocity on the  $i$ -th FS,  $1/v_F^i(\mathbf{k})$ , in  $k_z = 0$  and  $k_z = \pi$  planes, respectively. The horizontal axis is  $\theta = \tan^{-1}(\bar{k}_y/\bar{k}_x)$ , where  $(\bar{k}_x, \bar{k}_y)$  is the momentum on the FS with the origin at the center of each pocket. Figure 12 (c)-(f) show the  $l$ -orbital weight on the  $i$ -th FS, given by  $|U_{l,i}(\mathbf{k})|^2 = |\langle \mathbf{k}, l | \mathbf{k}, i \rangle|^2$  at the Fermi momentum.

As for the interaction term, we introduce both the Coulomb interaction ( $U, U', J = (U - U')/2$ ) and quadrupole interaction, as described in sec 1.6. In this section, we set  $g_1 = g$  and  $g_2 = 0$  in eq. (2).

Now, we perform the RPA for the present model by applying the eqs. (7) - (9) in sec. 1.6.2, by using  $64 \times 64 \times 16$   $\mathbf{k}$  meshes. We fix the temperature at  $T = 0.01$ , and set the filling of each Fe-site as  $n = 6.0$ .

In the RPA, the enhancement of the spin susceptibility  $\hat{\chi}^s$  is mainly caused by the intra-orbital Coulomb interaction  $U$ , using the “intra-orbital nesting” of the FSs. On the other hand, the enhancement of  $\hat{\chi}^c$  in the present model is caused by the quadrupole-quadrupole interaction in eq. (2), utilizing the “inter-orbital nesting” of the FSs. The magnetic (orbital) order is realized when the spin (charge) Stoner factor  $\alpha_s$  ( $\alpha_c$ ), which is the maximum eigenvalue of  $\hat{\Gamma}^s \hat{\chi}^0(\mathbf{q}, 0)$ , ( $\hat{\Gamma}_g^c(0) \hat{\chi}^0(\mathbf{q}, 0)$ ), is unity. Here, the critical value of  $U$  is  $U_{\text{cr}} = 0.448$  eV, and the critical value of  $g_1$  is  $g_{\text{cr}} = 0.132$  eV for  $U = 0$ . (We note again that the band renormalization due to the mass enhancement  $m^*/m_b \sim 2$  is taken into account in the present tight-binding model.)

### 3 REPRODUCTION OF EXPERIMENTAL GAP STRUCTURE IN LIFEAS28

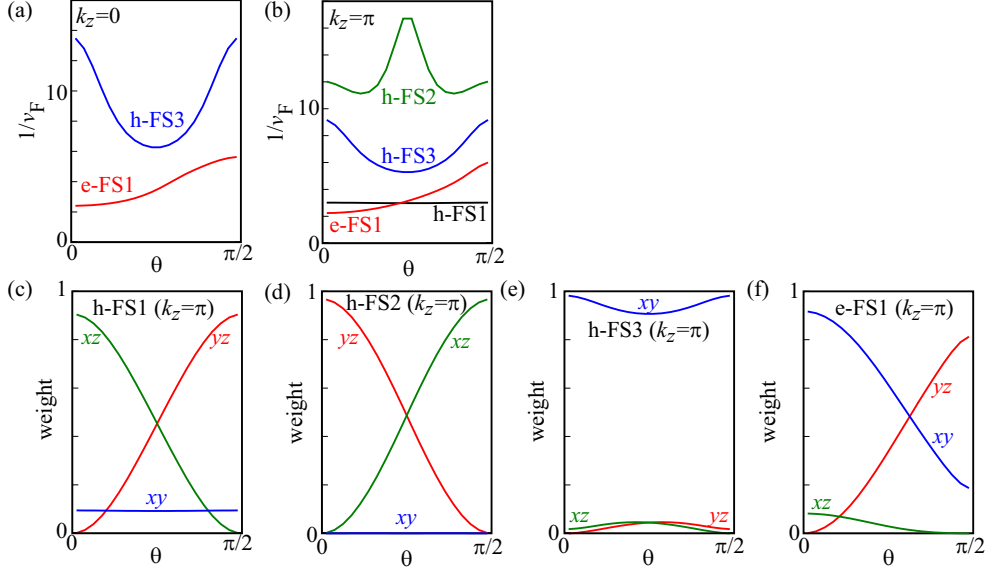


Figure 12: (a,b) Inverse of the Fermi velocity on the  $i$ -th FS  $1/v_F^i(\mathbf{k})$ . The horizontal axis is  $\theta = \tan^{-1}(k_y/k_x)$ . (c-f) The weight of each  $d$ -orbital on the  $i$ -th FS. Reprinted from Ref.[76]. ©2014 by the American Physical Society.

Figure 13 (a) shows the obtained spin susceptibility  $\chi^s(\mathbf{q}, 0) \equiv \sum_{l,m} \chi_{l,l;m,m}^s(\mathbf{q}, 0)$  in the  $q_z = 0$  plane given by the RPA for  $U = 0.439$  and  $g = 0$ . The spin Stoner factor is  $\alpha_s = 0.98$ . At  $T = 0.01$ , the obtained peak is incommensurate at  $(\pi, \delta)$  with  $\delta \approx 0.1\pi$ , consistently with the recent neutron scattering experiment [69]. The relation  $\chi_{4,4;4,4}^s(\mathbf{q}, 0) \gg \chi_{2,2;2,2}^s(\mathbf{q}, 0), \chi_{3,3;3,3}^s(\mathbf{q}, 0)$  holds in the present model, due to the intra  $d_{xy}$ -orbital nesting between h-FS3 and e-FS. That is, the spin fluctuations develop mainly on the  $d_{xy}$ -orbital.

Figure 13 (b) shows the quadrupole susceptibility  $\chi_\Gamma^Q(\mathbf{q}, 0) = \sum_{l,l',m,m'} o_\Gamma^{l,l'} \chi_{l,l';m,m'}^c(\mathbf{q}, 0) o_\Gamma^{m',m}$  for the channel  $\Gamma = xz$  in the  $q_z = 0$  plane. The charge Stoner factor is  $\alpha_c = 0.98$ . In this model, both  $\chi_{xz}^Q(\mathbf{q}, 0)$  and  $\chi_{yz}^Q(\mathbf{q}, 0)$  are the most divergent channels. For  $\Gamma = xz$ , the dominant contribution comes from  $\chi_{3,4;4,3}^c(\mathbf{q}, 0) \approx \chi_{3,4;3,4}^c(\mathbf{q}, 0)$ , due to the inter-orbital nesting (orbital 3 and 4) between h-FS1,2 and e-FS1. The obtained  $\chi_{xz}^Q(\mathbf{q}, 0)$  shows broad peak around  $(\pi, \delta)$  with  $|\delta| \lesssim 0.2\pi$ .

We note that both  $\chi_{xz}^Q(\mathbf{q}, 0)$  and  $\chi^s(\mathbf{q}, 0)$  are almost independent of  $q_z$ .

### 3 REPRODUCTION OF EXPERIMENTAL GAP STRUCTURE IN LiFeAs29

That is, both the orbital and spin fluctuations are almost two-dimensional.

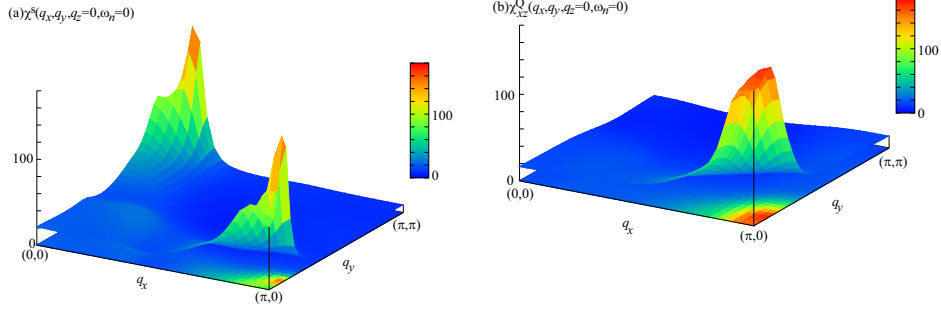


Figure 13: (a) Obtained spin susceptibility  $\chi^s(\mathbf{q}, 0)$  for  $U = 0.98U_{\text{cr}}$  and  $g_1 = g_2 = 0$ . The spin fluctuations develop mainly on the  $d_{xy}$ -orbital. (b) Obtained  $O_{xz}$ -channel quadrupole susceptibility  $\chi^Q_{xz}(\mathbf{q}, 0)$  for  $U = 0$  and  $g_1 = 0.98g_{\text{cr}}$ , developed among the  $d_{xz}/d_{yz}$ -orbitals. Reprinted from Ref.[76]. ©2014 by the American Physical Society.

Next, we solve the linearized Eliashberg equation based on the three-dimensional model of LiFeAs. In order to obtain the fine momentum dependence of the SC gap, we concentrate on the gap functions only on the FSs as done in Ref. [73]: We used  $80 \times 16$   $\mathbf{k}$  points for each Fermi surface sheet. Without impurities, the linearized Eliashberg equation is given as [73]

$$\lambda_E \Delta^i(\mathbf{k}, \epsilon_n) = \frac{\pi T}{(2\pi)^3} \sum_{\epsilon_m} \sum_j^{\text{FS}} \int_{\text{FS}j} \frac{d\mathbf{k}'_{\text{FS}j}}{v^j(\mathbf{k}')} V^{ij}(\mathbf{k}, \mathbf{k}', \epsilon_n - \epsilon_m) \frac{\Delta^j(\mathbf{k}', \epsilon_m)}{|\epsilon_m|}, \quad (18)$$

where  $\lambda_E$  is the eigenvalue that reaches unity at  $T = T_c$ .  $i$  and  $j$  denote the FSs, and  $\Delta^i(\mathbf{k}, \epsilon_n)$  is the gap function on the  $i$ -th FS at the Fermi momentum  $\mathbf{k}$ . The integral in eq. (18) means the surface integral on the  $j$ -th FS. The pairing interaction  $V$  in eq. (18) is

$$V^{ij}(\mathbf{k}, \mathbf{k}', \epsilon_n - \epsilon_m) = \sum_{l_i} U_{l_1,i}^*(\mathbf{k}) U_{l_4,i}(\mathbf{k}) \times V_{l_1 l_2, l_3 l_4}(\mathbf{k} - \mathbf{k}', \epsilon_n - \epsilon_m) U_{l_2,j}(\mathbf{k}') U_{l_3,j}^*(\mathbf{k}'), \quad (19)$$

$$\hat{V} = \hat{V}^c + \hat{V}^s + \hat{V}^{(0)}, \quad (20)$$

$$\hat{V}^c = \frac{1}{2}\hat{\Gamma}_g^c\hat{\chi}^c\hat{\Gamma}_g^c, \quad \hat{V}^s = -\frac{3}{2}\hat{\Gamma}^s\hat{\chi}^s\hat{\Gamma}^s, \quad (21)$$

$$\hat{V}^{(0)} = \frac{1}{2}(\hat{\Gamma}_g^c - \hat{\Gamma}^s), \quad (22)$$

where  $U_{l,i}(\mathbf{k}) = \langle \mathbf{k}; l | \mathbf{k}; i \rangle$  is the transformation unitary matrix between the band and the orbital representations.

In this calculation, we simplify the energy dependence of  $\hat{V}$ . We assume that  $\hat{V}^\xi$  ( $\xi = c, s$ ) can be separated into the momentum and orbital dependent part  $\hat{V}^\xi(\mathbf{k}, \omega_l = 0)$  and energy dependent part  $g_\xi(\omega_l)$ :

$$\hat{V}^\xi(\mathbf{k}, \omega_l) = \hat{V}^\xi(\mathbf{k}, \omega_l = 0) \times g_\xi(\omega_l). \quad (23)$$

We calculated  $\hat{V}^\xi(\mathbf{k}, \omega_l = 0)$  without approximation. On the other hand,  $g_\xi(\omega_l)$  is determined as

$$g_\xi(\omega_l) = \text{Re} \left[ \frac{V_{\max}^\xi(\omega_l)}{V_{\max}^\xi(\omega_l = 0)} \right], \quad (24)$$

where  $V_{\max}^\xi(0)$  is the largest value of  $V_{l_1 l_2, l_3 l_4}^\xi(\mathbf{k}, \omega_l = 0)$  for any  $\{l_i\}$  and  $\mathbf{k}$ . It is verified that this simplification affects the momentum dependence of the SC gap functions only quantitatively, although the obtained  $\lambda_E$  is slightly underestimated. Thus, this approximation would be appropriate for the present purpose, that is, the analysis of the anisotropy of the SC gap.

### 3.3 SC gap functions

In this section, we analyze the linearized Eliashberg equation, eq.(18), and obtain the three-dimensional gap function  $\Delta^i(\theta, k_z)$ , defined on the Fermi surface sheet  $i$ . Here, we divide the variables  $\theta = [0, 2\pi]$  and  $k_z = [-\pi, \pi]$  into 80 and 16 meshes, respectively, and use 512 Matsubara frequencies. The pairing interaction in eq. (20) is given by the RPA, assuming that  $J = J'$  and  $U = U' + 2J$ , and fix the ratio  $J/U = 1/6$ . The used parameters are  $T = 0.01$  and  $\omega_D = 0.02$ .

#### 3.3.1 Orbital-fluctuation-mediated $s_{++}$ -wave state

We first discuss the  $s_{++}$ -wave state realized by orbital fluctuations: Figure 14 (a) shows the obtained gap functions in the case of  $g_1 = 0.129$  and  $U = 0$

( $\alpha_c = 0.98$ ) in the  $k_z = \pi$ -plane. As for the hole-pockets, the gap functions on the h-FS1,2 composed of ( $d_{xz}, d_{yz}$ )-orbitals are the largest, while the gap on the h-FS3 composed of  $d_{xy}$ -orbital is the smallest. These results are quantitatively consistent with the experimental data [66] shown in dotted lines. (We adjust the magnitude of gap functions since it cannot be determined by solving the linearized gap equation.)

As for the electron-pockets, the gap function has the local maxima at  $\theta = 0$ , and the minimum point is  $\theta \approx 0.4\pi$ . This result is also consistent with the experimental data [66]. We found that the gap structure is essentially independent of the strength of orbital fluctuations. Therefore, overall experimental data are quantitatively reproduced by the orbital fluctuation theory. In Fig. 14 (b), we show the three-dimensional gap structure. The gap function on each FS is almost independent of  $k_z$ . Note that h-FS1 and h-FS2 appear only for  $k_z \approx \pm\pi$ ; see Fig. 11 (d).

In Fig. 14 (c), we discuss the origin of the orbital- and FS-dependences of the gap functions: The broad peak of the quadruple susceptibility  $\chi_{xz}^Q(\mathbf{q}, 0)$  at  $\mathbf{q} \approx (\pi, \delta)$  with  $|\delta| \lesssim 0.2\pi$  in Fig. 13 (b) is mainly given by the inter-orbital nesting between h-FS1,2 (orbital 2,3) and e-FS1 (orbital 4). For this reason, the maximum gap is realized on h-FS1 ( $\Delta_1^h$ ), h-FS2 ( $\Delta_2^h$ ), and e-FS1 ( $\Delta_1^e$ ) at  $\theta = 0$ . The gap size of h-FS3 ( $\Delta_3^h$ ) is the smallest, and its maximum is located at  $\theta = \pi/4$ . Therefore, the experimentally observed gap functions are understood based on the orbital fluctuation theory very well.

### 3.3.2 Spin-fluctuation-mediated $s_{\pm}$ -wave state

Next, we discuss the  $s_{\pm}$ -wave state realized by spin fluctuations: Figure 15 (a) shows the obtained gap structure in the case of  $g_1 = g_2 = 0$  and  $U = 0.439$  ( $\alpha_s = 0.98$ ) in the  $k_z = \pi$ -plane. The gap functions are almost independent of  $k_z$ , except that h-FS1,2 exist only for  $k_z \sim \pi$ . The obtained gap structure is essentially independent even if smaller  $U$  is used. Similarly to the previous study in Ref. [71], the gap functions on the h-FS1,2 are very small. However, this result is opposite to the experimental data shown by dotted lines. The  $k_z$ -dependence of the gap functions for  $\theta = \pi/4$  are shown in Fig. 15 (b). All gaps depend on  $k_z$  only slightly.

In addition, the obtained  $\theta$ -dependence of the gap on the e-FS1 is very different from the experimental data. Both  $\Delta_3^h$  and  $\Delta_1^e$  show the maximum values at  $\theta \approx \pi/4$ , because of the reason that they are connected by the wave vector of the spin fluctuations  $\mathbf{Q} \approx (\pi, 0), (0, \pi)$  shown in Fig. 15 (c).

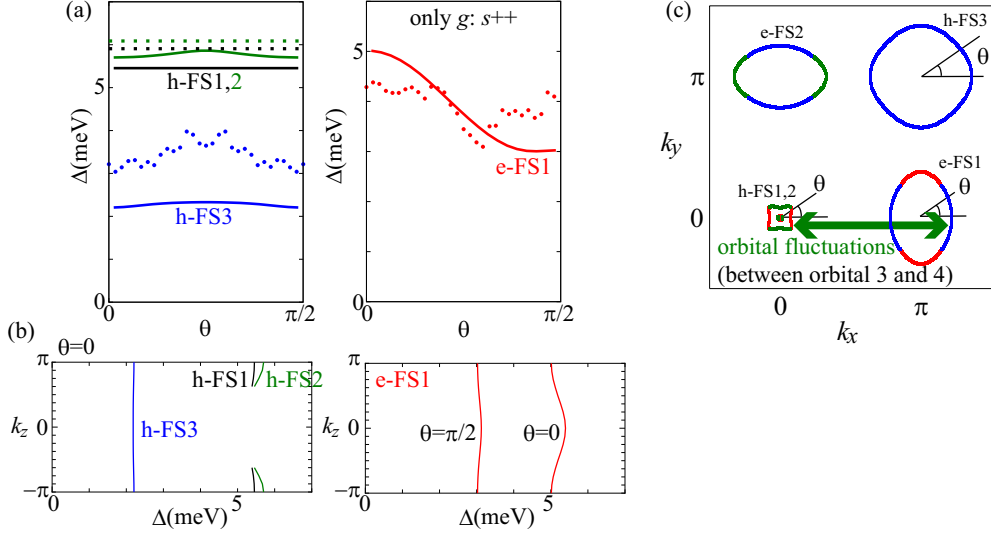


Figure 14: (a) Obtained  $s_{++}$ -wave gap functions for  $U = 0$  and  $g_1 = 0.129$  in the  $k_z = \pi$ -plane. The eigenvalue is  $\lambda_E = 0.64$ . The dotted lines represent the experimental data given by the ARPES measurement in Ref. [66]. (b)  $k_z$ -dependence of the gap functions. (c) Explanation for the orbital dependence of the gap functions due to orbital fluctuations. Reprinted from Ref.[76]. ©2014 by the American Physical Society.

In addition, the gap function of h-FS3 has eight nodes inconsistently with experiments. We verified these eight nodes disappear by using larger value of  $J/U \sim 0.4$  ( $U' = U - 2J \sim 0.2U$ ) as used in Ref. [71].

We found the  $s_{\pm}$ -wave gap for smaller  $U$  ( $\alpha_s = 0.90$ ). In this case, the magnitude of  $\Delta_{1,2}^h$  becomes relatively large. On the other hand, the nodal gap appears on the e-FSs, inconsistently with experiments. Thus, the overall experimental data is difficult to be explained by the spin fluctuation theory.

### 3.3.3 Coexistence of orbital and spin fluctuations: $s_{++}$ -wave and hole- $s_{\pm}$ -wave states

Now, we discuss the superconducting state when the orbital and spin fluctuations coexist. In the present model for LiFeAs, we find that the coexistence of orbital and spin fluctuations leads to a very exotic  $s$ -wave state, since the band structure of LiFeAs is very different from that of BaFe<sub>2</sub>(As,P)<sub>2</sub>.



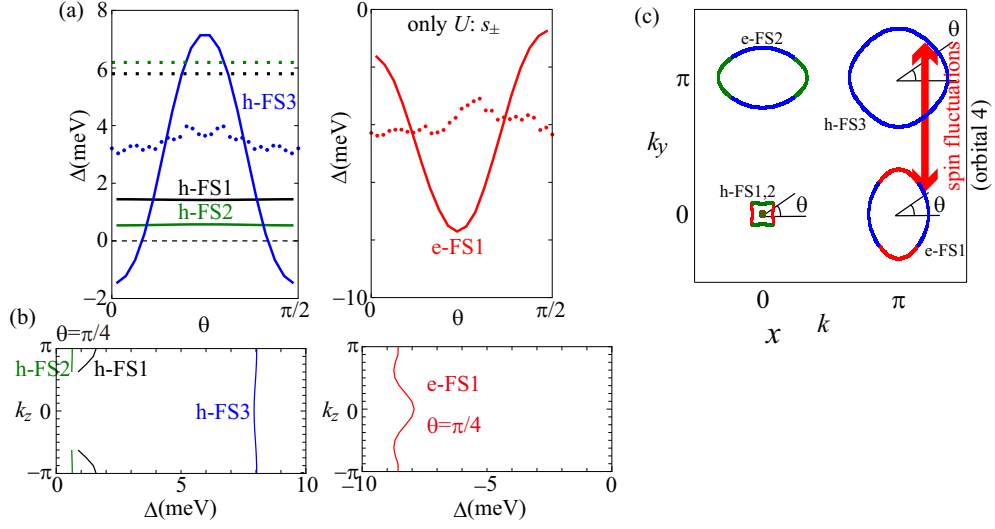


Figure 15: (a) Obtained  $s_{\pm}$ -wave gap functions for  $U = 0.439$  and  $g_1 = g_2 = 0$  in the  $k_z = \pi$ -plane. The eigenvalue is  $\lambda_E = 0.79$ . (b)  $k_z$ -dependence of the gap functions. (c) Explanation for the orbital dependence of the gap functions due to spin fluctuations. Reprinted from Ref.[76]. ©2014 by the American Physical Society.

Figure 16 (a) shows the obtained gap functions in the case of  $g_1 = 0.125$  and  $U = 0.200$ . The obtained Stoner factors are  $\alpha_c = 0.98$  and  $\alpha_s = 0.45$ . In this case, the orbital fluctuations are much larger than the spin fluctuations, and therefore we obtain the  $s_{++}$ -wave state. Except for h-FS3, the obtained gap structures are similar to those of the “pure  $s_{++}$ -wave state” without  $U$  in Fig. 14. Due to the moderate spin fluctuations on the  $d_{xy}$ -orbital, the anisotropy of  $\Delta_3^h$  is enlarged, consistently with experimental results.

If we increase the value of  $U$  further, we obtain a highly nontrivial gap structure with sign-reversal within the h-FSs: Figure 16 (b) shows the obtained gap functions in the case of  $g_1 = 0.122$  and  $U = 0.380$  ( $\alpha_c = 0.98$  and  $\alpha_s = 0.85$ ). Here, only  $\Delta_3^h$  is negative. In this “hole- $s_{\pm}$ -wave state” with “sign-reversal within hole-pockets”, the obtained gap structures of  $\Delta_{1,2}^h$  and  $\Delta_{1,2}^e$  are qualitatively similar to those in the  $s_{++}$ -wave state in Fig. 14. On the other hand,  $\Delta_3^h$  becomes very anisotropic, similarly to  $\Delta_3^h$  in the  $s_{\pm}$ -wave state in Fig. 15.

We discuss the reason why hole- $s_{\pm}$ -wave is realized by the coexistence of

orbital and spin fluctuations: In the present hole- $s_{\pm}$ -wave state, as shown in Fig. 16 (c),  $\Delta_{1,2}^h \cdot \Delta_{1,2}^e$  is positive due to orbital fluctuations, whereas  $\Delta_3^h \cdot \Delta_{1,2}^e$  is negative due to spin fluctuations. The obtained gap structure is qualitatively consistent with ARPES measurement in Ref. [66], although the gap structures of the  $s_{++}$ -wave state in Fig. 14 are more consistent with experiments. The present mechanism of the “sign-reversal within hole-pockets” due to orbital+spin fluctuations would be realized in other Fe-based superconductors. In fact, the hole- $s_{\pm}$ -wave state was first discussed in  $\text{Ba}_{1-x}\text{K}_x\text{Fe}_2\text{As}_2$  based on the thermal conductivity and penetration depth measurements [74], in addition to the recent ARPES study [75]. In Appendix B, We report the calculated hole- $s_{\pm}$  state by using the tight binding model of  $\text{BaFe}_2\text{As}_2$ .

Finally, we discuss on other theoretical works which predict the sign-reversal within hole-pockets. The hole- $s_{\pm}$ -wave state was first discussed by the authors in Ref. [77], assuming the repulsive interaction between h-FSs and e-FSs in addition to the repulsive pairing interaction within the h-FSs. For LiFeAs, similar scenario was discussed in Ref. [78], by introducing competing repulsive interactions, although the repulsive interaction within the h-FSs is much weaker within the RPA because of the ill-nesting. Also, the authors in Ref. [79] discussed the orbital antiphase  $s^{+-}$  state, in which the sign-reversal within hole-pocket is realized due to the strong repulsion between  $d_{xy}$  and  $d_{xz,yz}$  orbitals. In this state, the gap on e-FS is nodal in the unfolding picture, whereas it is fully-gapped in the present hole- $s_{\pm}$  state in Fig. 16 (b).

References [77, 78, 79] considered the competition between two kinds of repulsive interactions. In contrast, in the present paper, the hole- $s_{\pm}$ -wave state is explained in terms of the cooperation between the “attractive interaction among ( $d_{xz}, d_{yz}$ )- and  $d_{xy}$ -orbitals” and “repulsive interaction on the  $d_{xy}$ -orbital”.

### 3.4 Spin-orbit interaction

Recent ARPES study shows spin-orbit interaction (SOI) is important in LiFeAs[51, 52]. For example, it was found that the  $d_{xz/yz}$  hole bands at  $\Gamma$ -Z line, which must be degenerated when SOI is not considered, was split. Also, detailed gap structure was observed. The ARPES study by Miao, *et al.* shows only the outer band of the two  $d_{xz/yz}$  orbital hole bands at Z point crosses the Fermi level. [52] Although, another ARPES study by Borisenko *et al.* shows only the inner band of the two bands crosses the Fermi level. [51]

### 3 REPRODUCTION OF EXPERIMENTAL GAP STRUCTURE IN LIFEAS35

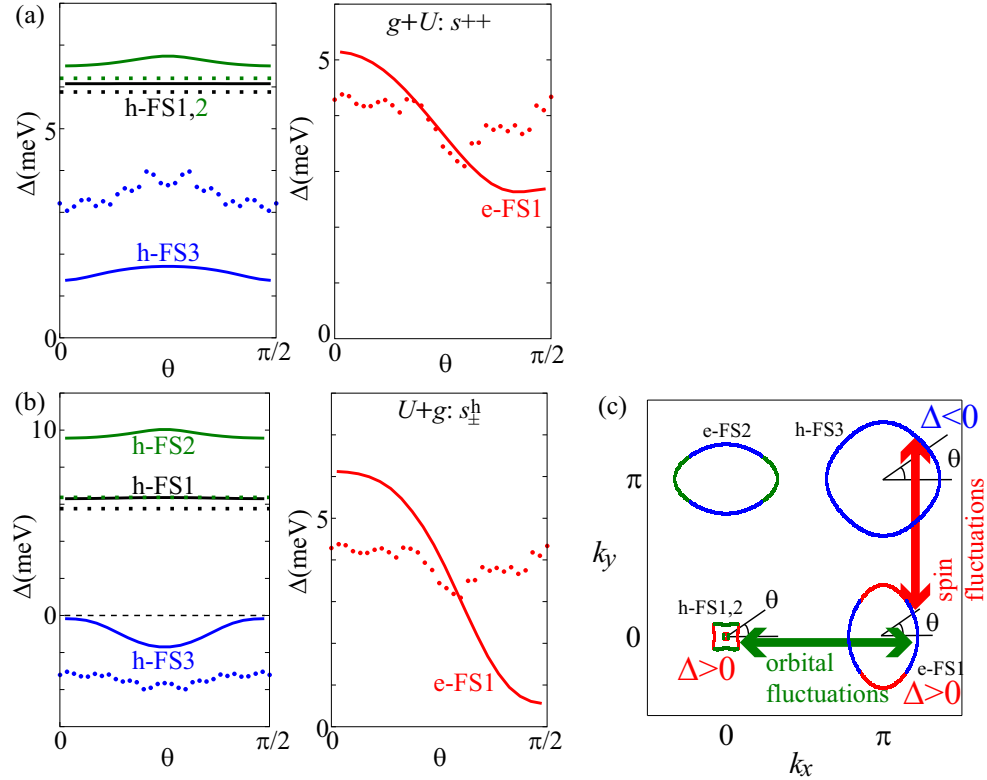


Figure 16: Obtained gap functions in the case where  $U \neq 0$  and  $g_1 \neq 0$ : (a) The  $s_{++}$ -wave state for  $U = 0.200$  and  $g_1 = 0.125$  in the  $k_z = \pi$ -plane. The eigenvalue is  $\lambda_E = 0.47$ . (b) The hole- $s_{\pm}$ -wave state for  $U = 0.380$  and  $g_1 = 0.122$  in the  $k_z = \pi$ -plane, in which only the gap function on the h-FS3 is negative. The eigenvalue is  $\lambda_E = 0.20$ . (c) Origin of the hole- $s_{\pm}$ -wave state due to the coexistence of the “orbital-fluctuations among ( $d_{xz}, d_{yz}$ )- and  $d_{xy}$ -orbitals” and the “spin-fluctuations on the  $d_{xy}$ -orbital”. Reprinted from Ref.[76]. ©2014 by the American Physical Society.

In addition, the strongly dispersing band with minimum in Z point is newly discovered. [51] Therefore, theoretical study with the band structures which reproduce the ARPES measurements and include the SOI is highly required. In this section, we introduce the Eliashberg gap equation including SOI. In addition, we construct the tight binding models which reproduce the ARPES measurements by Miao, *et al.* and that by Borisenko *et al.* and calculate the

gap structures by using the constructed models.

### 3.4.1 Hamiltonian including SOI

When we consider the SOI, we have to use ten orbital model. In the presence of SOI for  $d$  electron, total Hamiltonian is given by

$$\hat{H} = \begin{pmatrix} \hat{H}_0 + \lambda \hat{l}_z/2 & \lambda(\hat{l}_x - i\hat{l}_y)/2 \\ \lambda(\hat{l}_x + i\hat{l}_y)/2 & \hat{H}_0 - \lambda \hat{l}_z/2 \end{pmatrix} \quad (25)$$

where the first and the second rows (columns) correspond to  $\uparrow$ -spin and  $\downarrow$ -spin.  $\lambda$  is coupling constant of SOI. The matrix elements for  $\hat{\mathbf{l}}$  for  $d$ -orbital are given by[80]

$$\hat{l}_x = \begin{pmatrix} 0 & 0 & \sqrt{3}i & 0 & 0 \\ 0 & 0 & 0 & i & 0 \\ -\sqrt{3}i & 0 & 0 & 0 & -i \\ 0 & -i & 0 & 0 & 0 \\ 0 & 0 & i & 0 & 0 \end{pmatrix}, \quad (26)$$

$$\hat{l}_y = \begin{pmatrix} 0 & -\sqrt{3}i & 0 & 0 & 0 \\ \sqrt{3}i & 0 & 0 & 0 & -i \\ 0 & 0 & 0 & -i & 0 \\ 0 & 0 & i & 0 & 0 \\ 0 & i & 0 & 0 & 0 \end{pmatrix}, \quad (27)$$

$$\hat{l}_z = \begin{pmatrix} 0 & 0 & 0 & 0 & 0 \\ 0 & 0 & -i & 0 & 0 \\ 0 & i & 0 & 0 & 0 \\ 0 & 0 & 0 & 0 & 2i \\ 0 & 0 & 0 & -2i & 0 \end{pmatrix}, \quad (28)$$

where the first to fifth rows (columns) correspond to  $d$  orbitals  $z^2, xz, yz, xy, x^2 - y^2$ , respectively.

Red (Blue) lines of Fig. 17 (a) shows the band structure of LiFeAs for  $\lambda = 0.05$  (0), respectively. A and B points are shown in Fig. 17 (b). When  $\lambda = 0$ , the band near the Fermi level at Z point is degenerated, however, this degenerated band is split by SOI. Figure 17 (b) and (c) show the FSs of LiFeAs for  $\lambda = 0.05$  and 0, respectively. This model is consistent with the ARPES measurement by Miao *et al.* in the way that only outer band of two

### 3 REPRODUCTION OF EXPERIMENTAL GAP STRUCTURE IN LiFeAs37

$d_{xz/yz}$ -orbital hole band at Z point crosses the Fermi level. [52] In sec. 3.4.4, we construct the tight binding model which reproduces the recent ARPES measurement by Borisenko *et al.*

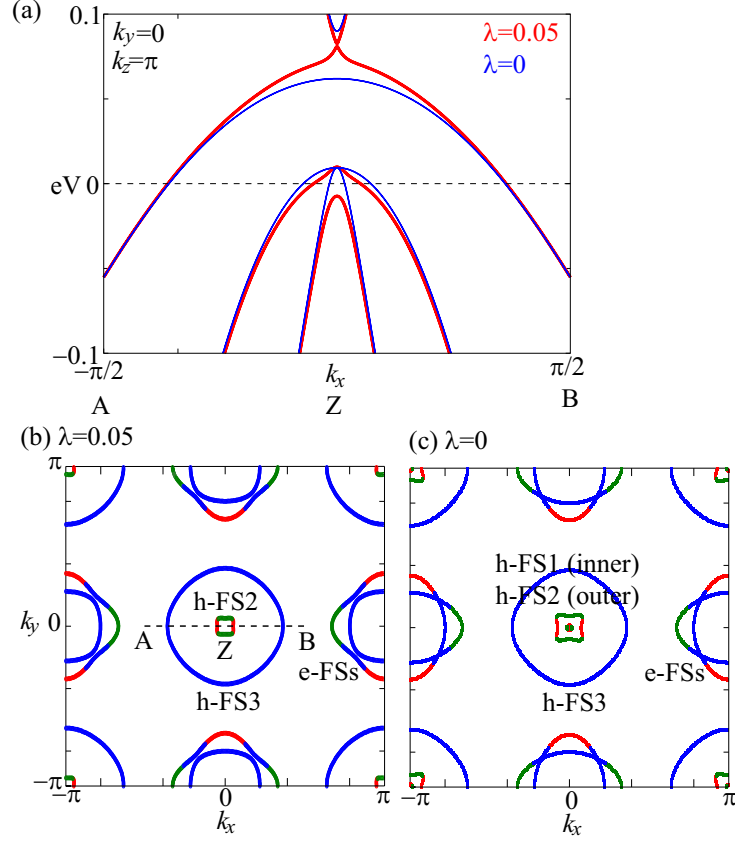


Figure 17: (a) The dispersion of the band structure between A and B points for  $\lambda = 0.05$  (red lines) and 0 (blue lines), respectively. A and B points are shown in (b). Fermi surfaces of LiFeAs on the plane of  $k_z = \pi$  for (b)  $\lambda = 0.05$  and (c) 0, respectively. Green, red, and blue colors correspond to  $d_{xz}$ ,  $d_{yz}$ , and  $d_{xy}$  orbitals, respectively.

### 3.4.2 Eliashberg gap equation with SOI

Here, we explain the linearized Eliashberg equation with SOI. The linearized Eliashberg equation is given as

$$\lambda_E \Delta_{\Sigma\bar{\Sigma}}^L(\mathbf{k}, \epsilon_n) = \frac{\pi T}{(2\pi)^3} \sum_{\epsilon_m} \sum_M^{\text{FS}} \sum_{\Lambda}^{\text{U,D}} \int_{\text{FSM}} \frac{d\mathbf{k}'_{\text{FSM}}}{v^M(\mathbf{k}')} \times V_{\Sigma\bar{\Sigma}\Lambda\bar{\Lambda}}^{LM}(\mathbf{k}, \mathbf{k}', \epsilon_n - \epsilon_m) \frac{\Delta_{\Lambda\bar{\Lambda}}^M(\mathbf{k}', \epsilon_m)}{|\epsilon_m|}, \quad (29)$$

where  $\lambda_E$  is the eigenvalue that reaches unity at  $T = T_c$ .  $L$  and  $M$  denote the FSs, and  $\Sigma$  and  $\Lambda$  ( $= +1(\text{U}), -1(\text{D})$ ) denote the pseudo-spin. Here,  $\Sigma = -\bar{\Sigma}$ .  $\Delta_{\Sigma\bar{\Sigma}}^L(\mathbf{k}, \epsilon_n)$  is the gap function on the  $L$ -th FS and pseudo-spin  $\Sigma$  and  $\bar{\Sigma}$  at the Fermi momentum  $\mathbf{k}$ . The integral in eq. (29) means the surface integral on the  $M$ -th FS. The pairing interaction  $V$  in eq. (29) is given by

$$V_{\Sigma\bar{\Sigma}\Lambda\bar{\Lambda}}^{LM}(\mathbf{k}, \mathbf{k}', \epsilon_n - \epsilon_m) = \sum_{lmm'l'} \sum_{\sigma\lambda\lambda'\sigma'} U_{lL}^{\sigma\Sigma*}(\mathbf{k}) U_{l'L'}^{\sigma'\bar{\Sigma}*}(-\mathbf{k}) \times V_{lmm'l'}^{\sigma\lambda\lambda'\sigma'}(\mathbf{k} - \mathbf{k}', \epsilon_n - \epsilon_m) U_{m'M'}^{\lambda'\bar{\Lambda}}(-\mathbf{k}') U_{mM}^{\lambda\Lambda}(\mathbf{k}'), \quad (30)$$

where  $\sigma, \lambda (= \uparrow (\text{u}), \downarrow (\text{d}))$  mean real spin and  $U_{lL}^{\sigma\Sigma}(\mathbf{k}) = \langle \mathbf{k}; l\sigma | \mathbf{k}; L\Sigma \rangle$  is the transformation unitary matrix between the band and the orbital representations.  $V_{lmm'l'}^{\sigma\lambda\lambda'\sigma'}$  is given by

$$V_{lmm'l'}^{\sigma\lambda\lambda'\sigma'} = V_{lmm'l'}^c \delta_{\sigma\lambda} \delta_{\sigma'\lambda'} + V_{lmm'l'}^s \boldsymbol{\sigma}_{\sigma\lambda} \cdot \boldsymbol{\sigma}_{\sigma'\lambda'} \\ = \begin{cases} V_{lmm'l'}^c + V_{lmm'l'}^s, & \sigma = \lambda = \lambda' = \sigma', \\ V_{lmm'l'}^c - V_{lmm'l'}^s, & \sigma = \lambda \neq \lambda' = \sigma', \\ 2V_{lmm'l'}^s, & \sigma = \lambda' \neq \lambda = \sigma', \\ 0, & \text{otherwise,} \end{cases} \quad (31)$$

$$\hat{V}^c = \frac{1}{2} \hat{\Gamma}^c \hat{\chi}^c \hat{\Gamma}^c, \quad \hat{V}^s = \frac{1}{2} \hat{\Gamma}^s \hat{\chi}^s \hat{\Gamma}^s. \quad (32)$$

Here,  $\hat{V}^\xi (\xi = \text{c, s})$  is calculated without SOI.

### 3 REPRODUCTION OF EXPERIMENTAL GAP STRUCTURE IN LIFEAS39

Now, we derive the relation which connect  $U_{lL}^{\sigma\Sigma}(\mathbf{k})$  to  $U_{lL}^{\bar{\sigma}\bar{\Sigma}}(-\mathbf{k})$ . The Hamiltonian including SOI is given by

$$\begin{aligned}\hat{H}(\mathbf{k}) &= \begin{pmatrix} \hat{H}_0(\mathbf{k}) + \lambda\hat{l}_z/2 & \lambda(\hat{l}_x - i\hat{l}_y)/2 \\ \lambda(\hat{l}_x + i\hat{l}_y)/2 & \hat{H}_0(\mathbf{k}) - \lambda\hat{l}_z/2 \end{pmatrix} \\ &= \begin{pmatrix} \hat{H}^{\text{uu}}(\mathbf{k}) & \hat{H}^{\text{ud}}(\mathbf{k}) \\ \hat{H}^{\text{du}}(\mathbf{k}) & \hat{H}^{\text{dd}}(\mathbf{k}) \end{pmatrix}.\end{aligned}\quad (33)$$

$\hat{H}^*(-\mathbf{k})$  is given by

$$\begin{aligned}\hat{H}^*(-\mathbf{k}) &= \begin{pmatrix} \hat{H}_0^*(-\mathbf{k}) + \lambda\hat{l}_z^*/2 & \lambda(\hat{l}_x^* - i\hat{l}_y^*)/2 \\ \lambda(\hat{l}_x^* + i\hat{l}_y^*)/2 & \hat{H}_0^*(-\mathbf{k}) - \lambda\hat{l}_z^*/2 \end{pmatrix} \\ &= \begin{pmatrix} \hat{H}_0(\mathbf{k}) - \lambda\hat{l}_z/2 & -\lambda(\hat{l}_x + i\hat{l}_y)/2 \\ -\lambda(\hat{l}_x - i\hat{l}_y)/2 & \hat{H}_0(\mathbf{k}) + \lambda\hat{l}_z/2 \end{pmatrix} \\ &= \begin{pmatrix} \hat{H}^{\text{dd}}(\mathbf{k}) & -\hat{H}^{\text{du}}(\mathbf{k}) \\ -\hat{H}^{\text{ud}}(\mathbf{k}) & \hat{H}^{\text{uu}}(\mathbf{k}) \end{pmatrix}.\end{aligned}\quad (34)$$

We define  $\hat{U}(\mathbf{k}) = \begin{pmatrix} \hat{U}^{\text{uU}}(\mathbf{k}) & \hat{U}^{\text{uD}}(\mathbf{k}) \\ \hat{U}^{\text{dU}}(\mathbf{k}) & \hat{U}^{\text{dD}}(\mathbf{k}) \end{pmatrix}$  as matrix which diagonalize  $\hat{H}(\mathbf{k})$ . That is

$$\hat{U}^\dagger(\mathbf{k})\hat{H}(\mathbf{k})\hat{U}(\mathbf{k}) = \begin{pmatrix} \hat{E}(\mathbf{k}) & \hat{0} \\ \hat{0} & \hat{E}(\mathbf{k}) \end{pmatrix}, \quad (35)$$

where  $\hat{E}(\mathbf{k})$  is diagonal matrix. When we use the eqs. (34) and (35),

$$\begin{pmatrix} \hat{U}^{\text{dD}\dagger}(\mathbf{k}) & -\hat{U}^{\text{uD}\dagger}(\mathbf{k}) \\ -\hat{U}^{\text{dU}\dagger}(\mathbf{k}) & \hat{U}^{\text{uU}\dagger}(\mathbf{k}) \end{pmatrix} \hat{H}^*(-\mathbf{k}) \begin{pmatrix} \hat{U}^{\text{dD}}(\mathbf{k}) & -\hat{U}^{\text{dU}}(\mathbf{k}) \\ -\hat{U}^{\text{uD}}(\mathbf{k}) & \hat{U}^{\text{uU}}(\mathbf{k}) \end{pmatrix} = \begin{pmatrix} \hat{E}(\mathbf{k}) & \hat{0} \\ \hat{0} & \hat{E}(\mathbf{k}) \end{pmatrix}. \quad (36)$$

Then,  $\hat{U}(-\mathbf{k})$  is given as

$$\hat{U}(-\mathbf{k}) = \begin{pmatrix} \hat{U}^{\text{dD}*}(\mathbf{k}) & -\hat{U}^{\text{dU}*}(\mathbf{k}) \\ -\hat{U}^{\text{uD}*}(\mathbf{k}) & \hat{U}^{\text{uU}*}(\mathbf{k}) \end{pmatrix}. \quad (37)$$

The relations which connect  $U_{lL}^{\sigma\Sigma}(\mathbf{k})$  to  $U_{lL}^{\bar{\sigma}\bar{\Sigma}}(-\mathbf{k})$  are given by

$$\begin{aligned}U_{lL}^{\text{uU}}(-\mathbf{k}) &= U_{lL}^{\text{dD}*}(\mathbf{k}), & U_{lL}^{\text{dD}}(-\mathbf{k}) &= U_{lL}^{\text{uU}*}(\mathbf{k}), \\ U_{lL}^{\text{uD}}(-\mathbf{k}) &= -U_{lL}^{\text{dU}*}(\mathbf{k}), & U_{lL}^{\text{dU}}(-\mathbf{k}) &= -U_{lL}^{\text{uD}*}(\mathbf{k}).\end{aligned}\quad (38)$$

Next, we transform the gap equation (29). When we set  $\Sigma = U(\bar{\Sigma} = D)$  and resolve the summation of  $\Lambda$ , gap equation is calculated as

$$\begin{aligned} \lambda_E \Delta_{UD}^L(\mathbf{k}, \epsilon_n) = & \frac{\pi T}{(2\pi)^3} \sum_{\epsilon_m} \sum_M^{\text{FS}} \int_{\text{FSM}} \frac{d\mathbf{k}'_{\text{FSM}}}{v^M(\mathbf{k}')} \\ & \times \left\{ V_{UDUD}^{LM}(\mathbf{k}, \mathbf{k}', \epsilon_n - \epsilon_m) \frac{\Delta_{UD}^M(\mathbf{k}', \epsilon_m)}{|\epsilon_m|} \right. \\ & \left. + V_{UDDU}^{LM}(\mathbf{k}, \mathbf{k}', \epsilon_n - \epsilon_m) \frac{\Delta_{DU}^M(\mathbf{k}', \epsilon_m)}{|\epsilon_m|} \right\} \quad (39) \end{aligned}$$

When we use the relation  $\Delta_{UD}^L(k) = -\Delta_{DU}^L(k)$ ,

$$\begin{aligned} \lambda_E \Delta^L(\mathbf{k}, \epsilon_n) = & \frac{\pi T}{(2\pi)^3} \sum_{\epsilon_m} \sum_M^{\text{FS}} \int_{\text{FSM}} \frac{d\mathbf{k}'_{\text{FSM}}}{v^M(\mathbf{k}')} \\ & \times \left\{ V_{UDUD}^{LM}(\mathbf{k}, \mathbf{k}', \epsilon_n - \epsilon_m) - V_{UDDU}^{LM}(\mathbf{k}, \mathbf{k}', \epsilon_n - \epsilon_m) \right\} \frac{\Delta^M(\mathbf{k}', \epsilon_m)}{|\epsilon_m|} \quad (40) \end{aligned}$$

where  $\Delta^L(\mathbf{k}, \epsilon_n) = \Delta_{UD}^L(\mathbf{k}, \epsilon_n)$ .

### 3.4.3 Gap structure in the case where only the outer $d_{xz/yz}$ -orbital hole band at Z point crosses the Fermi level

In this section, we analyze the linearized Eliashberg equation, Eq. (40) by using the tight binding model constructed in sec. 3.4.1. This model is consistent with the ARPES measurement by Miao *et al.* [52] Here, we divide the valuables  $\theta = [0 : 2\pi]$  and  $k_z = [-\pi : \pi]$  into 48 and 16 meshes, respectively. The used parameters are  $T = 0.01$ ,  $\omega_D = 0.02$ , and  $\lambda = 0.05$ .

We first discuss the  $s_{++}$ -wave state realized by orbital fluctuations: Figure 18 (a) shows the obtained gap functions in the case of  $g_1 = 0.129$  and  $U = 0$  ( $\alpha_c = 0.98$ ) (same as sec. 3.3.1) in the  $k_z = \pi$  plane. As for the hole pockets, the gap functions on the h-FS2 composed of  $(d_{xz}, d_{yz})$  orbitals are the largest, while the gap on the h-FS3 composed of the  $d_{xy}$  orbital is the smallest. These results are quantitatively consistent with the experimental data [66] shown by dotted lines (We adjust the magnitude of gap functions since it cannot be determined by solving the linearized gap equation.) and very similar to our previous results without SOI, except that h-FS1 exists only when we do not consider SOI as sec. 3.3.1 [76].



As for the electron pockets, the gap of inner e-FS is larger than that of outer e-FS, and has the local maxima at  $\theta = 0$  and  $\pi/2$  and the minima at  $\theta = \pi/4$ . These results are also consistent with the experimental data [66] and very similar to our previous results without SOI as sec. 3.3.1 [76]. These results are essentially independent of strength of smaller  $g$ . Obtained gap function is almost independent of  $k_z$ .

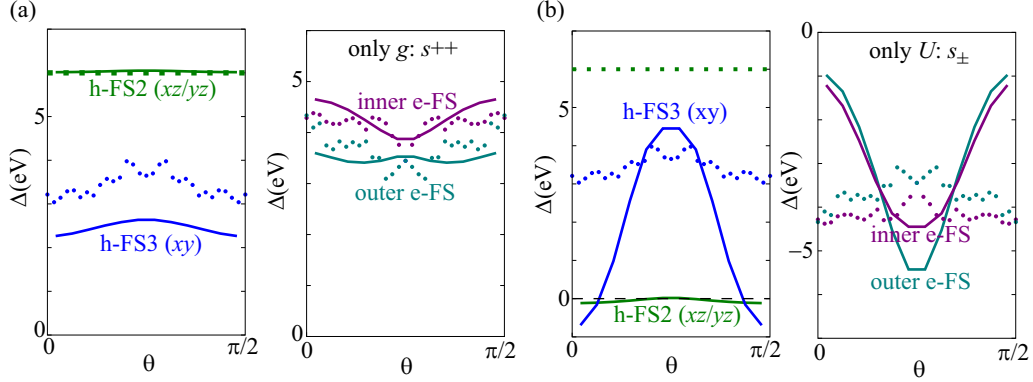


Figure 18: Obtained gap functions for (a)  $g_1 = 0.129$  and  $U = 0$  ( $s_{++}$ -wave state) (b)  $U = 0.349$  and  $g_1 = g_2 = 0$  ( $s_{\pm}$ -wave state) in the  $k_z = \pi$ -plane. The dotted lines represent the experimental data given by the ARPES measurement in Ref. [66].

Next, we discuss the  $s_{\pm}$ -wave state realized by spin fluctuations: Figure 18 (b) shows the obtained gap structure in the case of  $g_1 = g_2 = 0$  and  $U = 0.439$  ( $\alpha_s = 0.98$ ) (same as sec. 3.3.2) in the  $k_z = \pi$  plane. The gap functions are almost independent of  $k_z$ , except that h-FS2 exists only for  $k_z = \pi$ . The obtained gap structure is essentially independent even if smaller  $U$  is used. The gap functions on the h-FS2 are very small. However, this result is opposite to the experimental data [66] shown by dotted lines.

In addition, the obtained  $\theta$  dependence of the gap on the e-FSs and h-FS3 is very different from the experimental data [66]. Both the gap on the h-FS3 and e-FSs show the maximum values at  $\theta = \pi/4$ , since they are connected by the wave vector of spin fluctuations  $\mathbf{Q} \sim (\pi, 0), (0, \pi)$ . In addition the gap function on h-FS3 has eight nodes, which is inconsistent with experiments [66]. These results are very similar to our previous results without SOI as sec. 3.3.2 [76].

We note that almost same gap structure as sec. 3.3.3 is obtained when orbital and spin fluctuations coexist.

#### 3.4.4 Gap structure in the case where only the inner $d_{xz/yz}$ -orbital hole band at Z point crosses the Fermi level

Recently, detailed gap structure of LiFeAs is measured by ARPES. [51] The strongly dispersing band with minimum in Z point is newly discovered and only the inner band of two  $d_{xz/yz}$  hole band at Z point crosses the Fermi level. In this section, we construct the tight binding model which reproduces the band structure observed by Borisenko *et al.* and calculate the gap structure by using the model.

In order to reproduce the observed band structure, we add the following corrections of the hopping integrals of  $d_{xy}$  orbital,

$$\begin{aligned} \Delta t_{xy,xy}(0, 0, 0) &= \Delta E_{xy}/8, & \Delta t_{xy,xy}(\pm a, 0, 0) &= -\Delta E_{xy}/16, \\ \Delta t_{xy,xy}(0, \pm a, 0) &= -\Delta E_{xy}/16, & \Delta t_{xy,xy}(\pm a, \pm a, 0) &= \Delta E_{xy}/32, \\ \Delta t_{xy,xy}(0, 0, \pm c) &= -\Delta E_{xy}/16, & \Delta t_{xy,xy}(\pm a, 0, \pm c) &= \Delta E_{xy}/32, \\ \Delta t_{xy,xy}(0, \pm a, \pm c) &= \Delta E_{xy}/32, & \Delta t_{xy,xy}(\pm a, \pm a, \pm c) &= -\Delta E_{xy}/64, \end{aligned} \quad (41)$$

where  $a$  ( $c$ ) is the lattice constant between nearest Fe sites (nearest conducting layer). These corrections raise the  $d_{xy}$  orbital electron band at Z point by  $\Delta E_{xy}$ . Here, we set  $\Delta E_{xy} = -0.8$  and spin-orbit coupling constant  $\lambda = 0.05$ .

Figure 19 (a) shows the obtained FSs for  $k_y = 0$  plane of the three dimensional ten orbital model. There are tiny  $d_{xz/yz}$  orbital h-FSs at  $|k_z| \sim \pi/4$ , in addition to the h-FS1,3 and two e-FSs. Figure 19 (b) shows the dispersion of the band structure of ten orbital model. There is a strongly dispersing band on the  $\Gamma$ -Z line. Additionally, the h-FS near the Z point is comprised of inner band of the two  $d_{xz/yz}$  orbital hole band, although, the h-FS of the model constructed in sec. 3.4.1 is comprised of outer band.

Next, we analyze the linearized Eliashberg equation, Eq. (40). Here, we divide the valuables  $\theta = [0 : 2\pi]$  and  $k_z = [-\pi : \pi]$  into 48 and 16 meshes, respectively.

We first discuss the  $s_{++}$ -wave state realized by orbital fluctuations: Figure 19 (c) shows the obtained gap functions in the case of  $g_1 = 0.123$  and  $U = 0$  ( $\alpha_c = 0.98$ ) in the  $k_z = \pi$  plane. As for the hole pockets, the gap functions on the h-FS1 composed of  $(d_{xz}, d_{yz})$  orbitals are the largest, while the gap on the h-FS3 composed of the  $d_{xy}$  orbital is the smallest. These results are

### 3 REPRODUCTION OF EXPERIMENTAL GAP STRUCTURE IN LIFEAS43

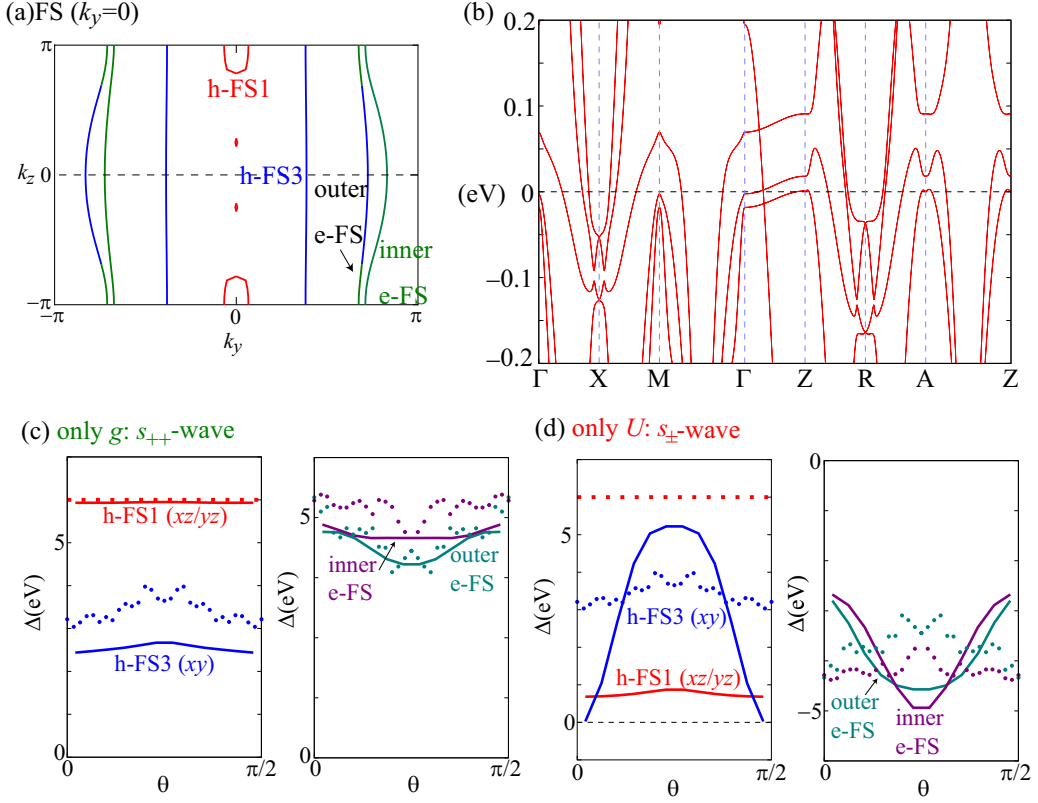


Figure 19: (a) The obtained FS in the  $k_y = 0$  plane of the three dimensional ten orbital model. We set  $\Delta E_{xy} = 0.8$  and  $\lambda = 0.05$ . The green, red, and blue colors correspond to  $d_{xz}$ ,  $d_{yz}$ , and  $d_{xy}$  orbitals, respectively. (b) The dispersion of the band structure of the ten orbital model. Obtained gap functions for (c)  $g_1 = 0.123$  and  $U = 0$  ( $s_{++}$ -wave state) (d)  $U = 0.424$  and  $g_1 = g_2 = 0$  ( $s_{\pm}$ -wave state) in the  $k_z = \pi$ -plane. The dotted lines represent the experimental data given by ARPES measurement in Ref. [66].

quantitatively consistent with the experimental data [66] shown by dotted lines and very similar to previous results in sec. 3.3.1 [76] and 3.4.3 except that the number of h-FSs near the Z point depend on the models.

As for the electron pockets, the gap of inner e-FS is larger than that of outer e-FS. However, the  $\theta$  dependence of gap function on e-FSs is different from experimental gap structure [66]. This result is inconsistent with the previous results in sec. 3.3.1 [76] and 3.4.3. This difference may be caused

by the fact that the  $\theta$  dependence of the weight of  $d$ -orbitals in this model is different from that in the models used in the previous sections.

Next, we discuss the  $s_{\pm}$ -wave state realized by spin fluctuations: Figure 18 (d) shows the obtained gap structure in the case of  $g_1 = g_2 = 0$  and  $U = 0.424$  ( $\alpha_s = 0.98$ ) in the  $k_z = \pi$  plane. The gap functions on the h-FS1 are very small. However, this result is opposite to the experimental data [66] shown by dotted lines.

In addition, the obtained  $\theta$  dependence of the gap on the e-FSs and h-FS3 is very different from the experimental data [66]. Both the gaps on the h-FS3 and e-FSs show the maximum values at  $\theta = \pi/4$ , since they are connected by the wave vector of spin fluctuations  $\mathbf{Q} \sim (\pi, 0), (0, \pi)$ . These results are rather similar to our previous results in sec. 3.3.2 [76] and 3.4.3.

### 3.5 Summary

In this section, we studied the three-dimensional five-orbital model of LiFeAs based on the recently-developed orbital-spin fluctuation theories [6, 13]. It is found that the experimentally observed gap structure of LiFeAs in Ref. [66] is quantitatively reproduced in terms of the orbital-fluctuation mechanism. Especially, the largest gap on h-FS1 and h-FS2 in Fig. 11 (b) is naturally reproduced by the inter-orbital fluctuations, as demonstrated in Figs. 14 (a), whereas it is unable to be explained by the spin fluctuation scenario. Therefore, the largest gap on h-FS1,2 is the hallmark of the orbital-fluctuation-mediated superconductivity in LiFeAs.

When orbital and spin fluctuations coexist, the “hole- $s_{\pm}$ -wave state” is obtained, in which only the gap of the largest  $d_{xy}$ -orbital hole-pocket is sign-reversed. We expect that the present mechanism of the “sign-reversal within hole-pockets” due to orbital+spin fluctuations would be realized in other Fe-based superconductors, although LiFeAs might not be the case. In fact, the realization of the hole- $s_{\pm}$ -wave state was first discussed in  $\text{Ba}_{1-x}\text{K}_x\text{Fe}_2\text{As}_2$  based on the thermal conductivity and penetration depth measurements [74]. The hole- $s_{\pm}$ -wave is naturally realized under the coexistence of the “spin-fluctuations on the  $d_{xy}$ -orbital” and the “orbital-fluctuations among the ( $d_{xz}, d_{yz}$ )- and  $d_{xy}$ -orbitals”.

Figure 20 shows the obtained  $\alpha_c$ - $\alpha_s$  phase diagram of the gap structure in LiFeAs. As expected, the  $s_{\pm}$ -wave state ( $s_{++}$ -wave state) is realized for wide region of  $\alpha_s > \alpha_c$  ( $\alpha_c > \alpha_s$ ). When both  $\alpha_s$  and  $\alpha_c$  are close to unity, we obtain the hole- $s_{\pm}$ -wave gap in a wide region. The gap structure at each point

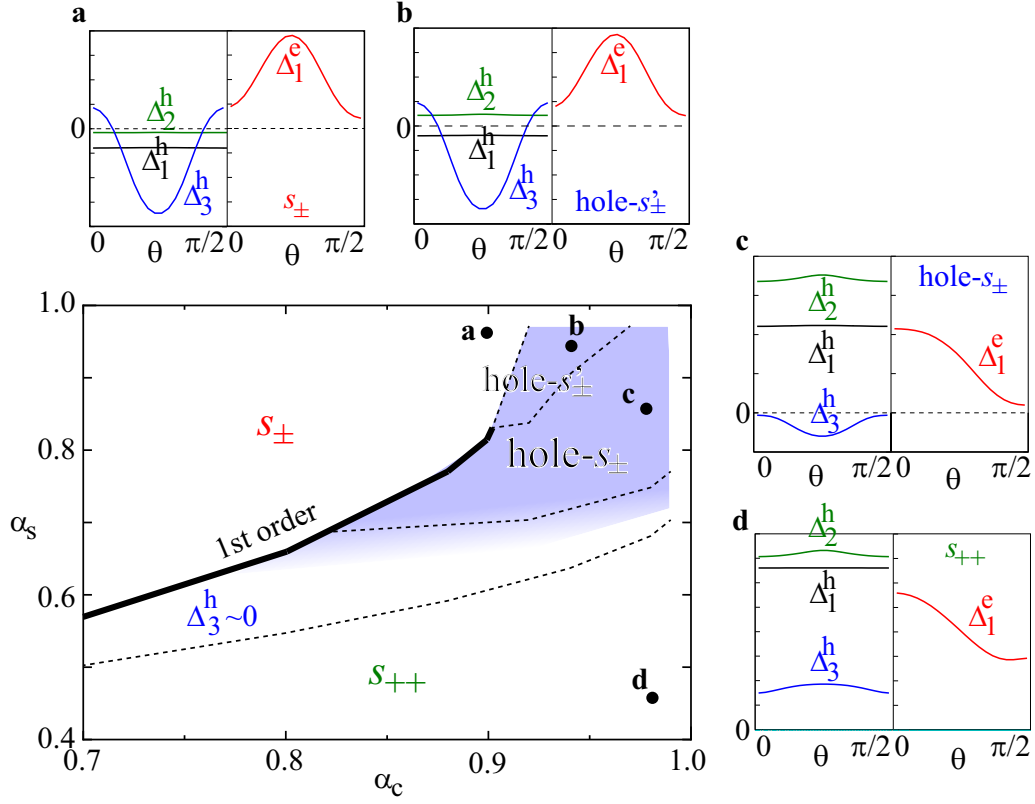


Figure 20:  $\alpha_c$ - $\alpha_s$  phase diagram of the gap structure in LiFeAs. The gap structure at each point **a**~**d** is shown in the figure. Each  $s_{\pm}$ -wave,  $s_{++}$ -wave, and hole- $s_{\pm}$ -wave state is realized in wide parameter region. In the region “ $\Delta_3^h \sim 0$ ”, the gaps on other FSs have the same sign, so nearly  $s_{++}$ -wave state is realized. In the “hole- $s'_{\pm}$ -wave gap” state at point **b**,  $\Delta_1^h \cdot \Delta_2^h$  is negative, and both  $|\Delta_1^h|$  and  $|\Delta_2^h|$  are very small. Reprinted from Ref.[76]. ©2014 by the American Physical Society.

**a**~**d** is shown in the figure. In the region “ $\Delta_3^h \sim 0$ ”, obtained  $\Delta_3^h(\theta)$  is nodal and very small in magnitude, and it is close to the  $s_{++}$ -wave state in that other gaps are positive and large. In the “hole- $s'_{\pm}$ -state” at point **b**,  $\Delta_1^h$  and  $\Delta_2^h$  are opposite in sign, and both  $|\Delta_1^h|$  and  $|\Delta_2^h|$  are very small. Therefore, various types of  $s$ -wave gap structure are realized due to the cooperation of orbital and spin fluctuations.

In sec. 3.4, We constructed two three-dimensional ten orbital models of

LiFeAs including SOI, which are consistent with ARPES measurements [51, 52] and studied the three-dimensional gap structure. When SOI is considered, degenerated band that consists of  $d_{xz}$  and  $d_{yz}$  orbital at  $\Gamma$ -Z line is split and one of the tiny h-FSs around Z point disappears. However, gap structure is not affected by SOI. Especially, the gap function on the tiny h-FS at Z point is large when  $g$  is large and  $s_{++}$ -wave state is realized.

## 4 Loop nodes on the e-FSSs of $\text{BaFe}_2(\text{As,P})_2$

### 4.1 Introduction for $\text{BaFe}_2(\text{As,P})_2$

Very interestingly, in optimally-doped  $\text{BaFe}_2(\text{As,P})_2$ , nodal gap structure with high- $T_c$  ( $\sim 30\text{K}$ ) is realized. The SC gaps on the three h-FSSs are fully-gapped and almost orbital-independent both in the  $k_z = \pi$  plane [81] and in the  $k_z = 0$  plane [54], consistently with the orbital fluctuation scenario in Ref. [41]. Also, loop-shape nodes on the e-FSSs are observed by angle-resolved thermal conductivity measurement in the vortex state [53] and ARPES measurements [54, 81]. These results indicate the existence of competing pairing interactions, and the study of these facts would be significant to understand the mechanism of high- $T_c$  superconductivity.

On the other hand, the ARPES measurement by Ref. [82] reported the horizontal node on the  $z^2$ -orbital e-FS around the Z point in  $\text{BaFe}_2(\text{As,P})_2$ , contrary to the reports by Refs. [54, 81]. This result is consistent with the prediction of the theory of the spin-fluctuation-mediated  $s_{\pm}$ -wave state in Ref. [83]. However, the existence of the horizontal node would be inconsistent with the large in-plane field angle dependence of the thermal conductivity reported in Ref. [53]. Also, very small  $T$ -linear term in the specific heat in the SC state would not be compatible to the presence of nodes on heavy h-FSSs [84, 85].

In this section, we theoretically study the origin of the nodal gap structure in  $\text{BaFe}_2(\text{As,P})_2$ , in order to obtain a significant information of the pairing mechanism of Fe-based superconductors. For this purpose, we construct the three-dimensional (3D) ten-orbital tight-binding model for  $\text{BaFe}_2(\text{As,P})_2$ , and calculate the dynamical spin and orbital susceptibilities due to the combination of Coulomb and quadrupole interactions. By solving the Eliashberg gap equation, we obtain the fully-gapped  $s_{\pm}$ -wave ( $s_{++}$ -wave) state due to strong spin (orbital) fluctuations. When both spin and orbital fluctuations strongly develop, which will be realized near the orthorhombic phase, nodal  $s$ -wave state with loop-shape nodes on the e-FSSs is realized due to the competition between attractive and repulsive interactions. It is realized during a smooth crossover between  $s_{++-}$  and  $s_{\pm}$ -wave states [6, 86]. In contrast, the SC gaps on the h-FSSs are fully-gapped due to orbital fluctuations. Thus, the present study explains the main characters of the gap structure in  $\text{BaFe}_2(\text{As,P})_2$ .

In Sec. 4.2, we introduce the three-dimensional ten-orbital tight-binding

model, which contains two Fe-sites in each unit cell. We analyze this model based on the RPA, by taking both the Coulomb and quadrupole interactions into account. The latter interaction originates from the Coulomb interaction beyond the RPA, described by the vertex corrections. In Sec. 4.3, we analyze the SC gap equation for various model parameters, and derive the loop-shape nodes on e-FSs due to the competition between orbital and spin fluctuations. Some discussion and the summary are presented in Secs. 4.4 and 4.5, respectively.

## 4.2 Formulation

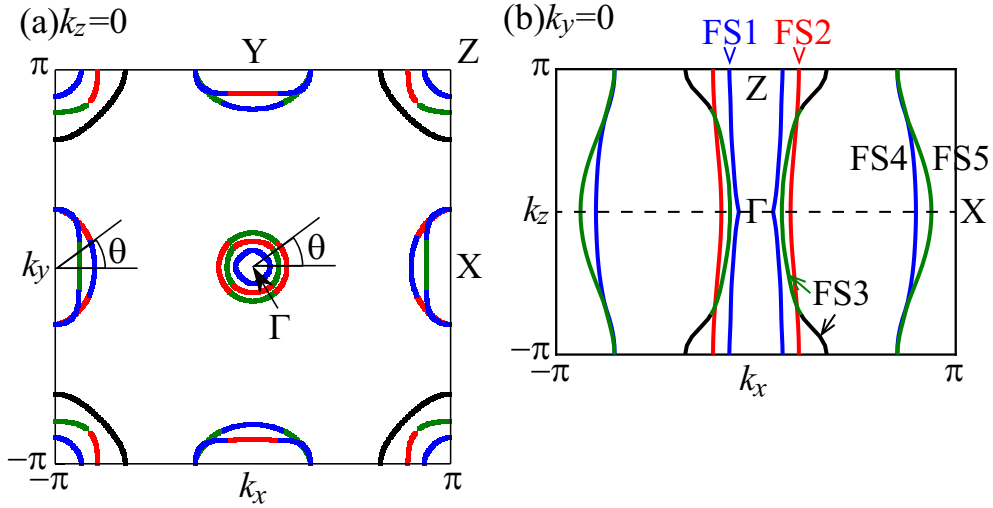


Figure 21: The Fermi surfaces in the (a)  $k_z = 0$  plane and (b)  $k_y = 0$  plane of the present ten orbital model for the filling  $n = 6.0$ . The green, red, blue and black lines correspond to  $xz$ ,  $yz$ ,  $xy$  and  $z^2$  orbitals, respectively. In (b), there are three h-FSs (FS1, FS2 and FS3) and four e-FSs (FS4 and FS5). Reprinted from Ref.[16]. ©2013 by the American Physical Society.

First, we perform the local-density-approximation (LDA) band calculation for  $\text{BaFe}_2\text{As}_2$  and  $\text{BaFe}_2\text{P}_2$  using WIEN2K code based on the experienced crystal structure. Next, we derive the ten-orbital tight-binding model that reproduces the LDA band structure and its orbital character using WANNIER90 code and WIEN2WANNIER interface. [62] Using the obtained



two sets of tight-binding parameters (hopping integrals and on-site energies), the parameters of  $\text{BaFe}_2(\text{As}_{1-x}\text{P}_x)_2$  are well approximated by making a linear combination of them with a ratio of  $1 - x : x$  [83]. In this section, we use the tight-binding parameters for  $x = 0.30$  otherwise noted. The kinetic term is given as eq. (17).

However, the  $xy$ -orbital h-FS given by the LDA is too small compared to the experimental results by ARPES measurements. In order to increase the size of  $xy$ -orbital h-FS, we introduce the following orbital-dependent potential term around the  $\Gamma$ -point:

$$\hat{H}^{\text{kin}} = \hat{H}^0 + \sum_{l\alpha,\sigma} \sum_{\mathbf{k}} e_l \left[ \frac{\cos k_x \cos k_y + 1}{2} \right] c_{l\alpha,\sigma}^\dagger(\mathbf{k}) c_{l\alpha,\sigma}(\mathbf{k}), \quad (42)$$

where  $e_l$  is the energy shift of the orbital- $l$  at  $\Gamma$ -point. We put  $e_{xy} = 0.02$  eV,  $e_{xz} = e_{yz} = -0.01$  eV and the others are 0. The FSs in this model are composed of three h-FSs around  $\Gamma$ -point and four e-FSs around  $X$ - and  $Y$ -points. Figure 21 shows the obtained FSs in the (a)  $k_z = 0$  and (b)  $k_y = 0$  planes, respectively. The electron filling per Fe-site is  $n = 6.0$ . In Fig. 21 (b), there are three h-FSs (FS1, FS2 and FS3) and two e-FSs (FS4 and FS5). We call FS4 (FS5) the outer (inner) e-FS.

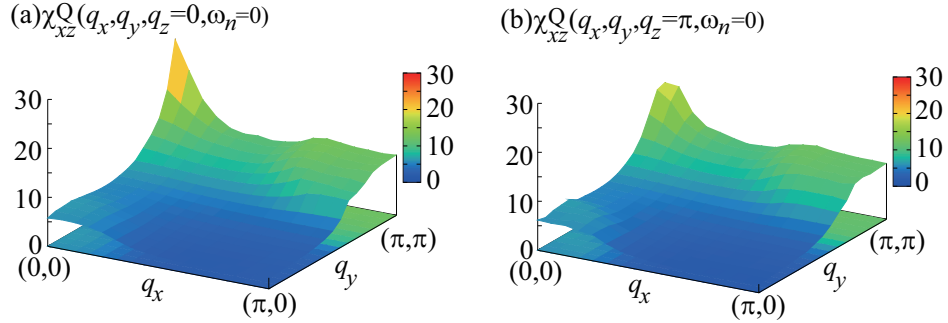


Figure 22: Obtained  $O_{xz}$ -channel quadrupole fluctuations  $\chi_{xz}^Q(\mathbf{q}, 0)$  for  $n = 6.0$  and  $\alpha_c = 0.98$ , in the (a)  $q_z = 0$  plane and (b)  $q_z = \pi$  plane. The obtained  $q_z$  dependence of  $\chi_{xz}^Q(\mathbf{q}, 0)$  is rather weak. Reprinted from Ref.[16]. ©2013 by the American Physical Society.

Next, we apply the RPA for this model. As for the interaction term, we introduce both the Coulomb interaction ( $U$ ,  $U'$ ,  $J = (U - U')/2$ ) and

quadrupole interaction, as described in sec 1.6. In this section, we set  $g_1 = g_2 = g$  in eq. (2) otherwise noted. In the presence of quadrupole interaction in eq. (2),  $\chi_\Gamma^Q(q)$  given in eq. (14) is strongly enhanced. In the present study, the channel  $\Gamma = xz, yz$  is the most strongly enhanced, due to the good inter-orbital nesting in Fe-based superconductors [6]. Figure 22 shows the obtained  $\hat{\chi}_{xz}^Q(\mathbf{q}, 0)$  in the (a)  $q_z = 0$  and (b)  $q_z = \pi$  planes [40]. The large peak at  $\mathbf{q} \approx (0, \pi)$  originates from the interorbital ( $yz \leftrightarrow xy$ ) nesting between e-FS and h-FS, and the small peak at  $\mathbf{q} \approx (\pi, \pi)$  originates from the interorbital ( $xz \leftrightarrow z^2$ ) nesting between two h-FSs. Therefore, the obtained development of  $\chi_{xz}^Q(q)$  and  $\chi_{yz}^Q(q)$  means the existence of strong orbital fluctuations on the  $xz$ -,  $yz$ -,  $xy$ - and  $z^2$ -orbitals, of which the FSs of  $\text{BaFe}_2(\text{As,P})_2$  are composed.

Next, we explain linearized Eliashberg equation. In this section, we present the numerical results in the presence of impurities just to make the SC gap functions smoother. In the presence of dilute impurities ( $n_{\text{imp}} \ll 1$ ), the linearized Eliashberg equation is given as [73]

$$Z^i(\mathbf{k}, \epsilon_n) \lambda_E \Delta^i(\mathbf{k}, \epsilon_n) = \frac{\pi T}{(2\pi)^3} \sum_{\epsilon_m} \sum_j^{\text{FS}} \int_{\text{FS}j} \frac{d\mathbf{k}'_{\text{FS}j}}{v^j(\mathbf{k}')} V^{ij}(\mathbf{k}, \mathbf{k}', \epsilon_n - \epsilon_m) \frac{\Delta^j(\mathbf{k}', \epsilon_m)}{|\epsilon_m|} + \delta \Sigma_a^i(\mathbf{k}, \epsilon_n), \quad (43)$$

where  $\lambda_E$  is the eigenvalue that reaches unity at  $T = T_c$ .  $i$  and  $j$  denote the FSs, and  $\Delta^i(\mathbf{k}, \epsilon_n)$  is the gap function on the  $i$ -th FS (FS $i$ ) at the Fermi momentum  $\mathbf{k}$ . The integral in eq. (43) means the surface integral on FS $j$ . The pairing interaction  $V$  in eq. (43) is given as eq. (19).

In eq. (43),  $Z$  is given as

$$Z^i(\mathbf{k}, \epsilon_n) = 1 + \frac{\gamma^i(\mathbf{k}, \epsilon_n)}{|\epsilon_n|}, \quad (44)$$

where  $\gamma^i$  is the impurity induced quasiparticle damping rate. Here, we calculate the damping rate using  $T$ -matrix approximation. We consider the case of Fe-site substitution, where the impurity potential  $I$  is diagonal in the  $d$ -orbital basis. The  $T$ -matrix for an impurity at  $\alpha (= A \text{ or } B)$  site is given as

$$\hat{T}^\alpha(\epsilon_n) = \left[ \hat{1} - \hat{I}^\alpha \hat{G}_{\text{loc}}^\alpha(\epsilon_n) \right]^{-1} \hat{I}^\alpha, \quad (45)$$

which is  $\mathbf{k}$ -independent in the orbital basis. Here,  $I_{l,l'}^\alpha = I \delta_{l,l'}$  is the impurity

potential, and  $\hat{G}_{\text{loc}}^\alpha$  is the local Green function given as

$$\begin{aligned} [G_{\text{loc}}]_{ll'}^\alpha(\epsilon_n) &= \frac{1}{N} \sum_{\mathbf{k}'} G_{ll'}^\alpha(\mathbf{k}', \epsilon_n) \\ &= -s_n \frac{i\pi}{(2\pi)^3} \sum_j \int_{\text{FS}_j} \frac{d\mathbf{k}'_{\text{FS}_j}}{v^j(\mathbf{k}')} U_{l\alpha,j}(\mathbf{k}') U_{l'\alpha,j}^*(\mathbf{k}'), \end{aligned} \quad (46)$$

where  $s_n = \text{sgn}(\epsilon_n)$ .

In the  $T$ -matrix approximation, which is exact for  $n_{\text{imp}} \ll 1$ , the normal self-energy in the band diagonal basis is given as

$$\delta\Sigma_{\mathbf{n}}^i(\mathbf{k}, \epsilon_n) = n_{\text{imp}} \sum_{ll'\alpha} U_{l\alpha,i}^*(\mathbf{k}) T_{ll'}^\alpha(\epsilon_n) U_{l'\alpha,i}(\mathbf{k}), \quad (47)$$

where  $n_{\text{imp}}$  is the impurity concentration ratio. Then, the quasiparticle damping rate is given as

$$\gamma^i(\mathbf{k}, \epsilon_n) = -\text{Im} \delta\Sigma_{\mathbf{n}}^i(\mathbf{k}, \epsilon_n) s_n. \quad (48)$$

Also,  $\delta\Sigma_{\mathbf{a}}^i$  is the impurity-induced anomalous self-energy given as

$$\delta\Sigma_{\mathbf{a}}^i(\mathbf{k}, \epsilon_n) = n_{\text{imp}} \sum_{ll'\alpha} U_{l\alpha,i}^*(\mathbf{k}) U_{l'\alpha,i}(\mathbf{k}) \sum_{mm'} T_{lm}^\alpha(\epsilon_n) X_{mm'}^\alpha(\epsilon_n) T_{l'm'}^\alpha(-\epsilon_n), \quad (49)$$

where

$$X_{mm'}^\alpha(i\epsilon_n) = \frac{\pi}{(2\pi)^3} \sum_j \int_{\text{FS}_j} \frac{d\mathbf{k}'_{\text{FS}_j}}{v^j(\mathbf{k}')} U_{m\alpha,j}(\mathbf{k}') U_{m'\alpha,j}^*(\mathbf{k}') \frac{\Delta^j(\mathbf{k}', \epsilon_n)}{|\epsilon_n|}. \quad (50)$$

In this section, we simplify the energy dependence of  $\hat{V}$  as explained as eqs. (23) and (24) at the end of sec. 3.2.

### 4.3 SC gap structures

In this section, we analyze the linearized Eliashberg equation, eq. (43), using the 3D model of  $\text{BaFe}_2(\text{As,P})_2$  for  $n = 6.0$ . Hereafter, we use  $32 \times 32 \times 16\mathbf{k}$  meshes for calculating charge and spin susceptibilities. We assume that  $J = J'$  and  $U = U' + 2J$ , and fix the ratio  $J/U = 1/6$ . In solving the Eliashberg equation, Here, we divide the variables  $\theta = [0, 2\pi]$  and  $k_z = [-\pi, \pi]$  into 40 and 16 meshes, respectively, and 512 Matsubara frequencies. In this section, we perform the calculation  $T = 0.005$  and  $\omega_D = 0.02$ .

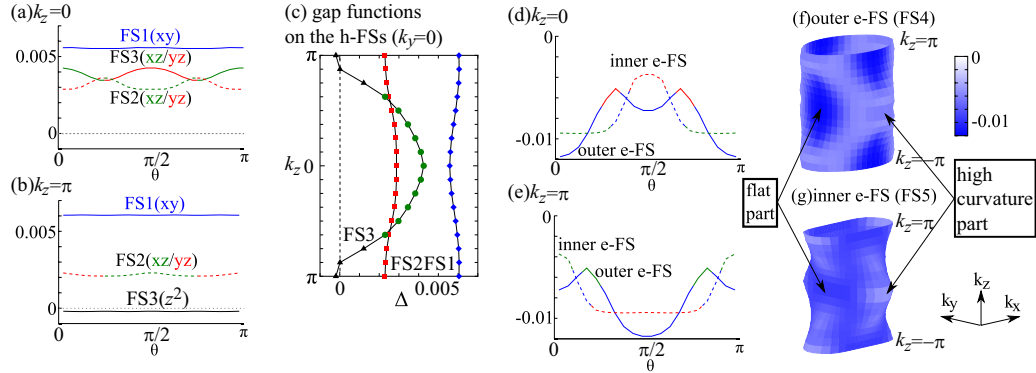


Figure 23: Obtained SC gap functions for  $U = 1.15$  and  $g_1 = g_2 = 0$ . (a),(b) SC gap functions on the h-FSs in  $k_z = 0$  and  $k_z = \pi$  planes. The green, red, blue and black lines correspond to  $xz$ ,  $yz$ ,  $xy$  and  $z^2$  orbitals, respectively. (c)  $k_z$  dependence of the SC gaps on the h-FSs in  $k_y = 0$  planes. Horizontal node appears on the FS3 around  $k_z = \pm\pi$ . (d),(e) SC gap functions on the e-FSs in  $k_z = 0$  and  $k_z = \pi$  planes. (f),(g) 3D gap functions on the outer and inner e-FSs. Reprinted from Ref.[16]. ©2013 by the American Physical Society.

#### 4.3.1 $s_{\pm}$ -wave SC gap mediated by spin fluctuations

First, we study the spin-fluctuation-mediated  $s_{\pm}$ -wave superconducting state for  $U \lesssim U_{\text{cr}}$  by putting  $g_1 = g_2 = 0$  and  $n_{\text{imp}} = 0$ . Here, we put  $U = 1.15$  ( $\alpha_s = 0.98$ ), and the obtained eigenvalue is  $\lambda_E = 1.01$ . The obtained gap structure is almost independent of  $\alpha_s$ . First, we discuss the SC gaps on the h-FSs. Figures 23(a) and (b) show the obtained gap functions on the h-FSs in the  $k_z = 0$  and  $\pi$  planes, respectively. The definitions of  $\theta$  and FS1-5 are shown in Fig. 21. In the  $k_z = 0$  plane, the SC gap size weakly depends on the orbital character of the FSs. However, in the  $k_z = \pi$  plane, the SC gap size strongly depends on the  $d$ -orbital. Especially, the SC gap on the  $z^2$ -orbital FS is almost zero and negative, reflecting the small spin fluctuations in the  $z^2$ -orbital because of the absence of the intra  $z^2$ -orbital nesting. (Note that  $z^2$ -orbital is absent on the e-FSs.) The horizontal node is clearly recognized in the SC gap in the  $k_y = 0$  plane shown in Fig. 23 (c). The obtained horizontal node on FS3 near  $k_z = \pi$  is consistent with the previous RPA calculation by Suzuki *et al* [83].

The obtained horizontal node would contradict to the four-fold symmetry of the thermal conductivity [53] and the small Volovik effect in the specific heat measurement [84, 85]. According to ARPES measurements, the horizontal-node was reported in Ref. [82], whereas it was not observed in Refs. [54, 81].

Next, we discuss the SC gaps on the e-FSSs. Figures 23 (d) and (e) show the obtained gap functions on the e-FSSs in the  $k_z = 0$  and  $\pi$  planes, respectively. As we can see, line nodes do not appear on the e-FSSs. This result is consistent with the analysis in Ref. [87], that is, the  $s_{\pm}$ -wave gap on the e-FSSs is fully-gapped if the h-FS made of  $xy$ -orbital appears. Note that the SC gaps for  $k_z = \pi$  in Fig. 23 (e) are obtained by rotating the gaps in the  $k_z = 0$  plane in (d) by  $\pi/2$ . Also, Fig. 23 (f) and (g) show 3D gap functions on the outer and inner FSs (FS4 and FS5), respectively. On both e-FSSs, the SC gap on the “flat part” is larger than that on the “high curvature part”.

#### 4.3.2 $s_{++}$ -wave SC gap mediated by orbital fluctuations

Next, we study the orbital-fluctuation-mediated  $s_{++}$ -state superconducting state for  $g \lesssim g_{\text{cr}}$  by putting  $U = 0$  and  $n_{\text{imp}} = 0$ . Here, we put  $g_1 = g_2 = 0.22$  ( $\alpha_c = 0.98$ ), and the obtained eigenvalue is  $\lambda_E = 0.59$ . The obtained gap structure is almost independent of  $\alpha_c$ . Figures 24 (a) and (b) show the obtained gaps on the h-FSSs in the  $k_z = 0$  and  $\pi$  planes, respectively. In highly contrast to the spin fluctuation scenario, the gap size on  $z^2$ -orbital FS is comparable with that on the other FSs, since strong orbital correlations are developed in all  $d$ -orbitals. Note that the quadrupole interaction possesses many non-zero interorbital matrix elements. The present numerical result is consistent with our previous calculation using the 2D 5-orbital model.[41]

Figure 24 (c) shows that the SC gap size of each h-FSSs is approximately independent on  $k_z$ , which is consistent with the small orbital dependence of the SC gap in  $(\text{Ba,K})\text{Fe}_2\text{As}_2$  and  $\text{BaFe}_2(\text{As,P})_2$  observed in Refs. [54, 81]. Figures 24(d) and (e) show the obtained gaps on the e-FSSs in the  $k_z = 0$  and  $\pi$  planes, respectively. Figure 24 (f) and (g) show the 3D SC gap functions on the outer and inner e-FSSs (FS4 and FS5), respectively. Thus, the obtained SC gaps on the e-FSSs is isotropic for any  $k_z$ .

We also discuss the SC gap functions in the case of  $g_1 = g$  and  $g_2 = 0$  in eq. (2). Figure 25 shows  $k_z$  dependence of the SC gaps on the h-FSSs for  $g_1 = 0.24$  ( $\alpha_c = 0.98$ ) and  $U = 0$ . In this case, the gap function on the  $z^2$ -orbital h-FS is smaller compared to the case of  $g_1 = g_2 = g$  in Fig. 24.

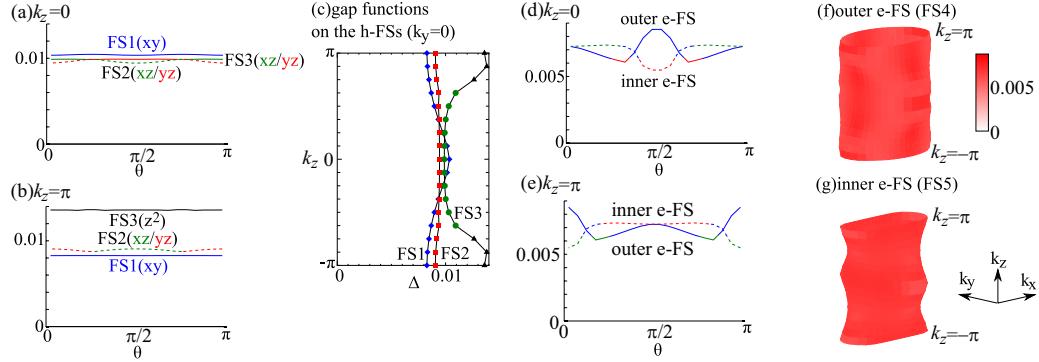


Figure 24: Obtained SC gap functions for  $g_1 = g_2 = 0.22$  and  $U = 0$ . (a),(b) SC gap functions on the h-FSSs in  $k_z = 0$  and  $k_z = \pi$  planes. The green, red, blue and black lines correspond to  $xz$ ,  $yz$ ,  $xy$  and  $z^2$  orbitals, respectively. (c)  $k_z$  dependence of the SC gaps on the h-FSSs in  $k_y = 0$  plane. Used colors are same as (a) and (b). (d),(e) SC gap functions on the e-FSSs in  $k_z = 0$  and  $k_z = \pi$  planes. (f),(g) 3D gap functions on the outer and inner e-FSSs. Reprinted from Ref.[16]. ©2013 by the American Physical Society.

On the other hand, the obtained SC gaps on the e-FSSs are almost isotropic, similarly to the results of  $g_1 = g_2 = g$ .

#### 4.3.3 Loop-shape nodes due to the competition of spin and orbital fluctuations

Recently, several measurements observed the nodal gap structure in  $\text{BaFe}_2(\text{As}_{1-x}\text{P}_x)_2$  [53, 54, 81]. This compound is very clean, and very accurate measurements of gap structure have been performed. They present a significant challenge for theories to reproduce the observed gap structure. However, as discussed in Sec. 4.3.1 and 4.3.2, we cannot reproduce the line-nodes on the electron FSs when either spin or orbital fluctuations solely develop.

Here, we study the emergence of highly anisotropic  $s$ -wave state due to the strong orbital and spin fluctuations. In the phase diagram of  $\text{BaFe}_2(\text{As}_{1-x}\text{P}_x)_2$ , both  $T_N$  and  $T_S$  decrease to zero at almost the same critical point  $x_c \approx 0.3$ . This fact means that both spin and orbital fluctuations become comparable in magnitude at  $x \sim x_c$ . Here, we consider the case that

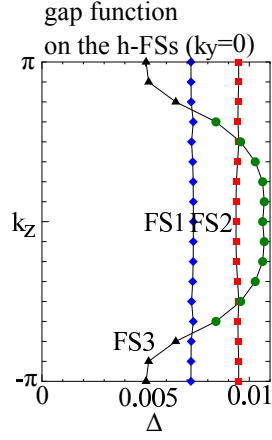


Figure 25: Obtained  $k_z$  dependence of the SC gaps on the h-FSs in  $k_y = 0$  plane. Used parameters are  $g_1 = 0.24$ ,  $g_2 = 0$  and  $U = 0$ . Reprinted from Ref.[16]. ©2013 by the American Physical Society.

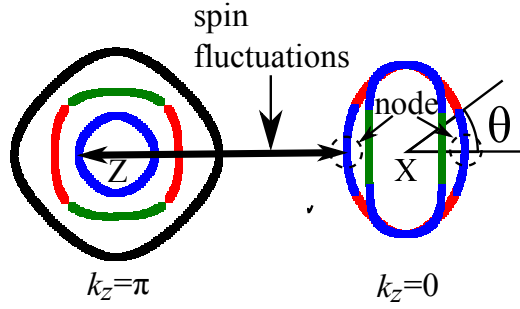


Figure 26: Formation of the nodal  $s$ -wave gap (shown in Fig. 27) due to the competition of orbital fluctuations (=inter-orbital attraction) and spin fluctuations (=intra-orbital repulsion). Green, red, blue, and black lines correspond to  $xz$ ,  $yz$ ,  $xy$ , and  $z^2$ -orbitals, respectively. Reprinted from Ref.[16]. ©2013 by the American Physical Society.

the  $s_{++}$ -wave state is realized by stronger orbital fluctuations. As increasing the spin fluctuation with momentum  $\mathbf{Q}$ ,  $\Delta_{\mathbf{k}}$  and  $\Delta_{\mathbf{k}+\mathbf{Q}}$  are suppressed when both  $\mathbf{k}$  and  $\mathbf{k} + \mathbf{Q}$  are on the FSs with the same orbital character, and finally the sign change  $\Delta_{\mathbf{k}} \cdot \Delta_{\mathbf{k}+\mathbf{Q}} < 0$  could be achieved. Such strong anisotropy originates from the competition between the attractive interaction of  $V^c$  and

repulsive interaction of  $V^s$  in eq. (20) of sec. 3.2. As shown in Fig. 26, strong spin fluctuations on the  $xy$ -orbital (due to intra  $xy$ -orbital nesting) produce the loop-shape node on the e-FS. Similar "anisotropic  $s$ -wave gap modified by the spin fluctuations" is considered to be realized in  $(\text{Y,Lu})\text{Ni}_2\text{B}_2\text{C}$ . [88]

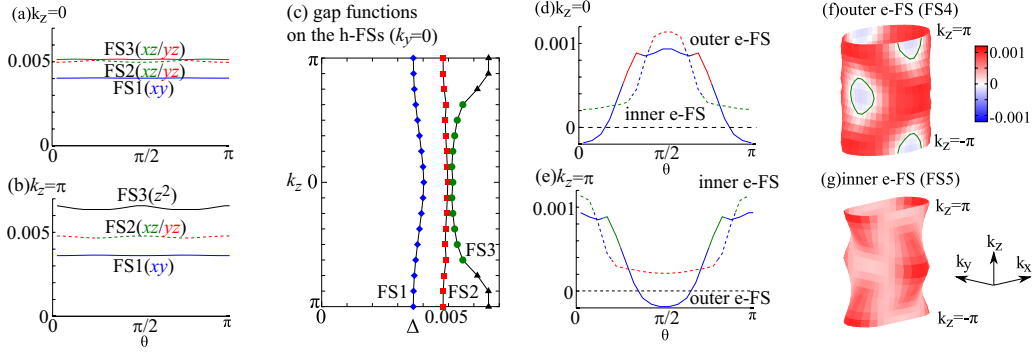


Figure 27: Obtained SC gap functions for  $g_1 = g_2 = 0.204$ ,  $U = 1.011$  and  $n_{\text{imp}} = 0.03$ . (a),(b) SC gap functions on the h-FSs in  $k_z = 0$  and  $k_z = \pi$  planes. (c)  $k_z$  dependence of SC gaps on the hole FSs in  $k_y = 0$  plane. (d),(e) SC gap functions on the e-FSs in  $k_z = 0$  and  $k_z = \pi$  planes. (f),(g) 3D gap functions on the outer and inner e-FSs. The green lines represent the gap nodes. Reprinted from Ref.[16]. ©2013 by the American Physical Society.

Hereafter, we present numerical results in the presence of small amount of impurities ( $I=1$  and  $n_{\text{imp}} = 0.03$ ), just to make the SC gap functions smoother. Figure 27 shows the results of nearly  $s_{++}$ -wave state with nodal structure on outer e-FS. We put  $g_1 = g_2 = 0.204$  and  $U = 1.011$ , ( $\alpha_c = 0.980$ ,  $\alpha_s = 0.859$ ), and the eigenvalue is  $\lambda_E = 0.50$ . Figures 27 (a)-(c) show the obtained SC gaps on the h-FSs in the  $k_z = 0$  plane,  $k_z = \pi$  plane, and  $k_y = 0$  plane, respectively. The obtained SC gaps on the h-FSs are nearly isotropic and orbital-independent, similarly to the results in Fig. 24. Especially, the gap size of the  $z^2$ -orbital h-FS is large even in the presence of loop-shape nodes on e-FSs.

Figures 27 (d) and (e) show the obtained SC gaps on the e-FSs in the  $k_z = 0$  and  $\pi$  planes, respectively. The SC gap on the inner e-FS is fully opened, and its sign is same as that on the h-FSs. On the outer e-FS, in contrast, the SC gap shows the sign change near  $\theta = 0, \pi$  ( $\theta = \pi/2, 3\pi/2$ ) in the  $k_z = 0$  plane ( $k_z = \pi$  plane). This sign change is caused by strong



spin fluctuations in the  $xy$ -orbital, as we have explained in Fig. 26. In this case, the SC gaps on the h-FSSs remains fully-gapped, due to the fact that the band-mass of h-FSSs is larger than that of the e-FSSs. As results, closed loop-shape nodes appear in the flat part on the outer e-FS, as recognized in Figs. 27 (f) and (g). This gap structure is consistent with the prediction given by the angle-resolved thermal conductivity under the magnetic field [53].

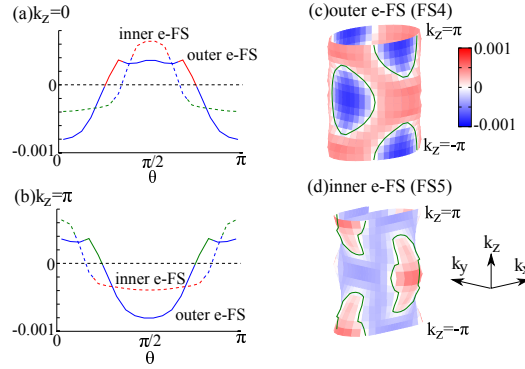


Figure 28: Obtained SC gap functions for  $g_1 = g_2 = 0.204$  and  $U = 1.017$ . (a),(b) SC gap functions on the e-FSSs in  $k_z = 0$  and  $k_z = \pi$  planes. (c),(d) 3D gap functions on the outer and inner e-FSSs. The green lines represent the gap nodes. Reprinted from Ref.[16]. ©2013 by the American Physical Society.

As increasing the value of  $U$  (or reducing  $n_{\text{imp}}$ ) slightly, the area of the sign reversed part on the outer e-FS increases, and the SC gap on the inner e-FS also shows the sign reversal. Figures 28 (a) and (b) show the SC gap functions on the e-FSSs for  $g_1 = g_2 = 0.204$  and  $U = 1.017$  ( $\alpha_c = 0.980$  and  $\alpha_s = 0.864$ ). The obtained eigenvalue is  $\lambda_E = 0.50$ . The obtained gap functions are approximately given by shifting the gaps in Figs. 27 (d) and (e) downwards, and line nodes appear on both the inner and outer e-FSSs. As described in Figs. 28 (c) and (d), closed nodal loops appear in the flat part on the outer e-FS and in the high curvature part on the inner e-FS. The SC gaps on the h-FSSs are almost the same as those shown in Fig 27 (a)-(c), so we do not show them.

As increasing the value of  $U$  (or reducing  $n_{\text{imp}}$ ) further, the sign of the SC gap on the outer e-FS is completely reversed, and small closed loop-nodes

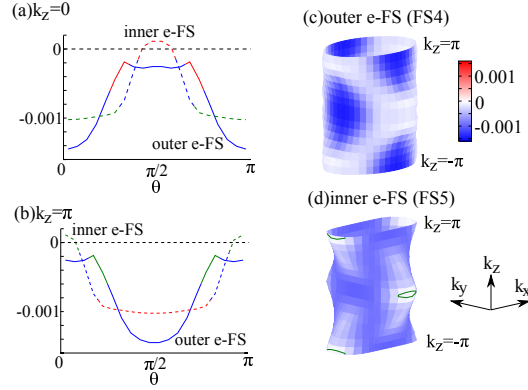


Figure 29: Obtained SC gap functions for  $g_1 = g_2 = 0.204$  and  $U = 1.023$ . (a),(b) SC gap functions in the e-FSs on  $k_z = 0$  and  $k_z = \pi$  planes. (c),(d) 3D gap functions on the outer and inner e-FSs. The green lines represent the gap nodes. Reprinted from Ref.[16]. ©2013 by the American Physical Society.

appear only on the inner e-FS. The obtained SC gaps are nearly  $s_{\pm}$ -wave state. Figures 29 (a) and (b) show the obtained gap functions on the e-FSs for  $g_1 = g_2 = 0.204$  and  $U = 1.023$  ( $\alpha_c = 0.980$ ,  $\alpha_s = 0.869$ ). They are approximately given by shifting the gaps in Figs. 28 (a) and (b) downwards. The obtained eigenvalue is  $\lambda_E = 0.50$ . Figures 29 (c) and (d) show the obtained 3D gap functions on the outer and inner e-FSs, respectively. Apparently, closed nodal loops appear in the high curvature part on the inner e-FS, whereas no nodes appear on the outer e-FS. This numerical result is consistent with the recent ARPES measurement by Yoshida *et al* [54]. On the other hand, the SC gaps on the h-FSs are similar to those in Figs. 27 (a)-(c).

In Figs. 27-29, we fixed the impurity parameters as  $n_{\text{imp}} = 0.03$  and  $I = 1$ . Now, we discuss the SC gap functions for general impurity parameters. Figure 30 (a) shows the  $U$ - $n_{\text{imp}}$  phase diagram for both  $I = 1$  and  $I = 0.3$ . The solid (dashed) lines represent the boundaries between  $s_{++}$  wave and nodal- $s$  wave, or nodal- $s$  wave and  $s_{\pm}$  wave for  $I = 1$  ( $I = 0.3$ ). As decreasing  $\alpha_s$  or increasing  $\alpha_c$ , the following crossover would be realized: (i) full gap  $s_{\pm}$ -wave  $\rightarrow$  (ii) nodal  $s$ -wave  $\rightarrow$  (iii) full gap  $s_{++}$ -wave. When both  $U$  and  $g$  are fixed, the same crossover occurs when  $n_{\text{imp}}$  increases. The residual resistivity

for  $I = 1$  derived from the linear response theory is about  $20 \mu\Omega\text{cm}$  per  $n_{\text{imp}} = 0.01$ .

We note that, in the present numerical calculation using 3D model, line-nodes can appear even if  $n_{\text{imp}} = 0$  as shown in Fig. 30. In contrast, in the previous calculation using 2D model [41, 43], we could not obtain the line-nodes for  $n_{\text{imp}} = 0$ , since the SC state changes from the  $s_{++}$ -wave to  $s_{\pm}$ -wave discontinuously as  $U$  increases.

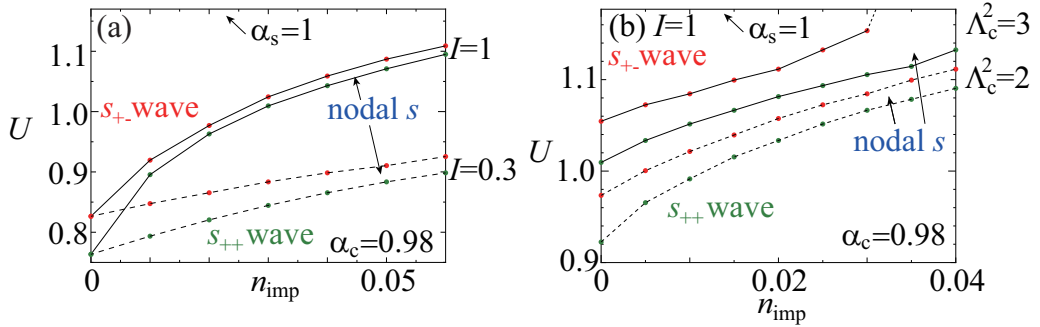


Figure 30:  $U$ - $n_{\text{imp}}$  phase diagram for  $\alpha_c = 0.98$  obtained for (a)  $I = 1$  and 0.3 with  $\Lambda_c = 1$  and for (b)  $I = 1$  with  $\Lambda_c = \sqrt{2}$  and  $\sqrt{3}$ . Reprinted from Ref.[16]. ©2013 by the American Physical Society.

In the present study based on the RPA, the  $s_{++} \leftrightarrow s_{\pm}$  crossover is realized in case of  $\alpha_s \ll \alpha_c$  ( $= 0.98$ ) for  $n_{\text{imp}} \ll 0.1$ . One of the main reasons would be the factor 3 in front of  $V^s$  in eq. (20), reflecting the  $\text{SU}(2)$  symmetry of the spin space. However, this factor 3 might be overestimated since the recent polarized neutron scattering measurements indicates the relation  $\chi_z^s(\mathbf{Q}) \gg \chi_{x,y}^s(\mathbf{Q})$  above  $T_c$  due to the spin-orbit interaction  $\lambda \mathbf{l} \cdot \mathbf{s}$  [89, 90].

Moreover, the RPA is recently improved by including the VC, and it was found that orbital fluctuations strongly develop in the Hubbard model [13]. Then, the orbital susceptibility is  $\hat{\chi}^c(q) = (\hat{X}^c(q) + \hat{\chi}^0(q))(1 - \hat{\Gamma}_g^c(\hat{X}^c(q) + \hat{\chi}^0(q))^{-1}$ , where  $\hat{X}^c(q)$  is the charge VC for the irreducible susceptibility. According to Ref. [13], the magnitude of the three-point vertex is estimated as  $\Lambda_c = 1 + X^c(q)/\chi^0(q) \sim 2$ , and then eq. (21) would be replaced with  $\hat{V}^c = \frac{1}{2}\Lambda_c^2\hat{\Gamma}_g^c\hat{\chi}^c\hat{\Gamma}_g^c$ . Figure 30 (b) shows the  $U$ - $n_{\text{imp}}$  phase diagram for  $\Lambda_c = \sqrt{2}$  and  $\sqrt{3}$ , in case of  $I = 1$ . We find that the  $s_{++}$ -wave region is widely extended, and the nodal- $s$ -wave region is also widen. The obtained gap

structure in the crossover regime for  $\Lambda_c > 1$  is the loop-shape nodes shown in Figs. 27-29.

#### 4.4 Discussion

In previous sections, we analyzed the gap equations based on the three-dimensional ten orbital model for  $\text{BaFe}_2(\text{As,P})_2$ . When orbital fluctuations are solely developed, fully-gapped  $s_{++}$ -wave state is realized. On the other hand, when spin fluctuations are solely developed, we obtain the  $s_{\pm}$ -wave state with horizontal node on a h-FS. During the crossover between  $s_{++}$ -wave and  $s_{\pm}$ -wave states due to the competition between orbital and spin fluctuations, the loop-shape nodes appear on the outer (inner) e-FS when the spin fluctuations are slightly weaker (stronger) than the orbital fluctuations. The obtained phase-diagram is shown in Fig. 30. We stress that all three h-FSs are fully-gapped during the crossover, since the SC gap on the  $z^2$ -orbital originates from the inter-orbital nesting between different h-FSs.

The crossover from the  $s_{\pm}$ -wave state to the  $s_{++}$ -wave state is also induced by increasing the impurity concentration. In this study, we considered the orbital-diagonal on-site impurity potential at Fe  $i$ -site, considering the Fe-site substitution by other elements. In this case, inter-band impurity scattering is always comparable to intra-band one, as shown by the  $T$ -matrix approximation in Ref. [9]. For this reason, when the spin fluctuations are solely developed, the realized  $s_{\pm}$ -wave state with  $T_{c0} \sim 30\text{K}$  is suppressed by small amount of impurities, with small residual resistivity  $\rho_0 \sim 5z^{-1}\mu\Omega\text{cm}$  ( $z^{-1} = m^*/m$  is the mass-enhancement factor). Since  $z^{-1} \sim 3$ , we can safely expect that the SC state in *dirty Fe-based superconductors* (say  $\rho_0 \sim 100\mu\Omega\text{cm}$ ) would be the  $s_{++}$ -wave state due to orbital fluctuations.

#### 4.5 Summary

In this section, we studied SC gap structure using ten orbital model for  $\text{BaFe}_2(\text{As,P})_2$ . When the orbital fluctuations due to inter-orbital quadrupole interaction (2) are strong, the  $s_{++}$ -wave state is realized. In contrast, the  $s_{\pm}$ -wave state is formed by strong spin fluctuations, mainly due to intra-orbital Coulomb interaction  $U$ . Both spin and orbital fluctuations would strongly develop in the optimally-doped regime near the O phase. In this case, we find that a smooth crossover between  $s_{++}$ - and  $s_{\pm}$ -wave states is

realized by changing the interactions or impurity concentration, without large suppression in  $T_c$ .

During this  $s_{++} \leftrightarrow s_{\pm}$  crossover, the loop-shape nodes are universally formed on the e-FSSs, as a result of the competition between inter-orbital attractive interaction and intra-orbital repulsive interaction. This result is consistent with recent angle-resolved thermal conductivity measurement [53] and ARPES measurement [54]. During the crossover, the SC gaps on the h-FSSs are fully-gapped and almost orbital independent due to orbital fluctuations, consistently with recent ARPES measurements [54, 81].

## 5 Summary

Since the discovery of iron based superconductivity, its superconducting mechanism had been studied intensively and it is one of the most significant research fields of condensed matter physics. Iron based superconductor is multiorbital system, differently from single orbital cuprate. In the mother compound, various phases such as the antiferromagnetic order and the orthorhombic structure phase transition appear, and the superconducting phase appears after the carrier doping or isovalent doping. While antiferromagnetic fluctuations are expected to exist near the antiferromagnetic order, the strong orbital fluctuations are also expected to develop near the structural transition. Therefore, the spin-fluctuation-mediated  $s_{\pm}$ -wave superconductivity [5] and the orbital-fluctuation-mediated  $s_{++}$ -wave superconductivity [6] had been proposed and studied based on the multiorbital models. In order to understand the pairing mechanism of iron pnictides, the  $\mathbf{k}$ -dependence of superconducting gap structure gives us important information. In this thesis, we constructed realistic three dimensional multiorbital models of  $\text{KFe}_2\text{Se}_2$ ,  $\text{LiFeAs}$ , and  $\text{BaFe}_2(\text{As,P})_2$ . Next, we calculated the gap structures when both the spin fluctuations and orbital fluctuations are developed. Finally, we compared the numerical results with the experimental results such as ARPES measurements.

In sec. 2, we study the heavily electron doped compound  $\text{KFe}_2\text{Se}_2$ . In this compound, the spin fluctuations favor the  $d$ -wave state and gap function inevitably has nodes. On the other hand, the orbital fluctuations favor the  $s_{++}$ -wave state, which is consistent with the experiments [47, 48, 49, 50]. Therefore, the orbital-fluctuation-mediated  $s_{++}$ -wave state is realized in  $\text{KFe}_2\text{Se}_2$ .

In sec. 3, we study the gap structure of  $\text{LiFeAs}$  in which superconductivity is realized without doping. In  $\text{LiFeAs}$ , the largest gap on the small h-FS is observed in ARPES measurements [66]. When the orbital fluctuations are strong and  $s_{++}$ -wave state is realized, the gaps on the small h-FSs are the largest of all and, therefore, the experimental results are reproduced. On the other hand, when spin fluctuations are strong and  $s_{\pm}$ -wave state is realized, the gaps on the small h-FSs are very small, which is inconsistent with experiments. In addition, we constructed more realistic model with SOI and calculated the gap structure, we obtained almost same results as previous results without SOI. Therefore, the orbital-mediated- $s_{++}$ -wave superconducting state is realized in  $\text{LiFeAs}$ .

In sec. 4, we study the gap structure of  $\text{BaFe}_2(\text{As,P})_2$ . The almost

equally-sized superconducting gaps on three h-FSs are measured in laser ARPES measurements [81]. When the spin-fluctuation-mediated  $s_{\pm}$ -wave state is realized, the gap on the h-FS which is composed of the  $z^2$ -orbital is very small and the horizontal nodes are formed: The reason is that the e-FSs are not composed of the  $z^2$ -orbital and therefore the intra- $z^2$ -orbital nesting is absent. These results are inconsistent with the experimental results. On the other hand, the orbital-fluctuation-mediated  $s_{++}$ -wave state is realized, the gap sizes on the all h-FSs are almost same since the orbital fluctuations including  $z^2$ -orbital are developed by the inter-orbital nesting between the h-FS and e-FSs. Meanwhile, line nodes are observed on the e-FSs. These nodes are reproduced when both the orbital and spin fluctuations are strong, as a result of the competition between different fluctuations. Indeed, the spin fluctuations and orbital fluctuations may balance in  $\text{BaFe}_2(\text{As,P})_2$  since the spin and orbital orders are vanished at almost same time.

Thus, the superconductivity is mainly realized by orbital fluctuations in  $\text{KFe}_2\text{Se}_2$ ,  $\text{LiFeAs}$ , and  $\text{BaFe}_2(\text{As,P})_2$ . In addition, the phase transition from tetragonal to orthorhombic [14] and the softening of shear modulus  $C_{66}$  [15] etc. can be explained by orbital fluctuation theory. Therefore, the development of strong orbital fluctuations is the significant key to understand the properties of both the superconducting and normal phases of iron based superconductors.

## Acknowledgments

I would like to express my appreciation to many people helping this research. I would like to express my gratitude for Professor Hiroshi Kontani for his great valuable advices, supports, and discussion during this research. I learned not only many things about this research, but attitude for science from his attitude for research. I would like to express my gratitude for Professor Seiichiro Onari for fruitful advices and discussion. I would like to thank Dr. Youichi Yamakawa for fruitful advices and discussion, especially about numerical calculations.

I wish to express my gratitude to all the members in the laboratory of Condensed-matter theory group for providing the good environments for my research. I would like to acknowledge the financial support provided by the Research Fellowship for Young Scientists of the Japan Society for the Promotion of Science and the Program for Leading Graduate Schools "Integrative Graduate Education and Research Program in Green Natural Sciences" of Japan Society for the Promotion of Science.

Finally, I would like to thank my family for helping me for many ways.



## A Five orbital tight binding model for LiFeAs

Here, we explain the five-orbital tight-binding model for LiFeAs, which is given in unfolding the ten-orbital model given in Ref. [71]. The ten-orbital model in Ref. [71] is obtained by fitting the experimental band structure of LiFeAs in Ref. [66] near the Fermi level. The five-orbital model (single Fe unit cell) is obtained by unfolding the ten-orbital model (two-Fe unit cell), according to the procedure in Ref. [22]. The FSs of both models are shown in Fig. 11 (a) and (b), respectively. Both models are equivalent, and the former model is more convenient for the numerical study. The FSs and band structure are given in Fig. 11. This experimental FSs of LiFeAs are very different from the FSs given by the density functional theory (DFT), in which FS1,2 predicted by the DFT are much larger. Better agreement between theory and ARPES is achieved by the LDA+DMFT study [91], since the FS1,2 shrinks due to the orbital-dependent self-energy that is absent in the LDA. As for the de Haas-van Alphen (dHvA) measurements, Ref. [92] showed reasonable agreement with the DFT for the e-FSs, and Ref. [93] reported the presence of very small three-dimensional hole-pockets, which would corresponds to h-FS1,2 in Fig. 11. The hopping parameters of the present model,  $t_{l,m}(\mathbf{R}_a)$  in eq. (17), are listed in Table I.

Table 1: Hopping integrals for  $\mathbf{R} = (x, y, z)$  for the present five-orbital model for LiFeAs. Notations are the same as those introduced in Refs. [5, 22].  $\sigma_y$ ,  $I$ , and  $\sigma_d$  corresponds to  $t_{l,m}(x, -y, z)$ ,  $t_{l,m}(-x, -y, z)$ , and  $t_{l,m}(y, x, z)$ , respectively. Here, ‘ $\pm$ ’ and ‘ $\pm(l', m')$ ’ in the row of  $(l, m)$  mean that the corresponding hopping is equal to  $\pm t_{l,m}(x, y, z)$  and  $\pm t_{l',m'}(x, y, z)$ , respectively. Notice also  $t_{l,m}(\mathbf{R}) = t_{m,l}(-\mathbf{R})$ .

$(l,m) \backslash \mathbf{R}$	[0,0,0]	[1,0,0]	[1,1,0]	[2,0,0]	[2,1,0]	[2,2,0]
(1,1)	-0.305					
(1,2)			-0.101			
(1,3)		0.100	-0.101			
(1,4)			-0.090			
(1,5)		-0.162				
(2,2)	-0.008	-0.050	0.152	-0.004	-0.040	-0.005
(2,3)			0.090			
(2,4)		-0.155	-0.064			
(2,5)			-0.010			
(3,3)	-0.008	-0.210	0.152	-0.051	0.053	-0.005
(3,4)			-0.064			
(3,5)		0.193	0.010			
(4,4)	0.020	0.019	0.030	-0.010	-0.004	
(4,5)						
(5,5)	-0.261	0.223	0.070			

$(l,m) \backslash \mathbf{R}$	[0,0,1]	[1,0,1]	[2,0,1]	$\sigma_y$	$I$	$\sigma_d$
(1,1)				+	+	+
(1,2)				-	-	+(1,3)
(1,3)				+	-	+(1,2)
(1,4)				-	+	+
(1,5)				+	+	-
(2,2)	-0.003	-0.012		+	+	+(3,3)
(2,3)				-	+	+
(2,4)				+	-	+(3,4)
(2,5)				-	-	-(3,5)
(3,3)	-0.003		0.011	+	+	+(2,2)
(3,4)				-	-	+(2,4)
(3,5)				+	-	-(2,5)
(4,4)	0.011	0.004		+	+	+
(4,5)				-	+	-
(5,5)				+	+	+

## B Hole- $s_{\pm}$ wave state in Ba122

Here, we show the hole- $s_{\pm}$ -wave realized in Ba122. First, we perform a local-density-approximation (LDA) band calculation for  $\text{BaFe}_2\text{As}_2$  and using the WIEN2K code based on the known crystal structure. Next, we derive a ten-orbital tight-binding model that reproduces the LDA band structure and its orbital character using the WANNIER90 code and the WIEN2WANNIER interface[62]. The  $d_{xy}$ -orbital h-FS by the LDA is too small compared to the experimental results from ARPES. In order to increase the size of the  $d_{xy}$ -orbital h-FS, we introduce the orbital-dependent potential term around  $\Gamma$  point by eq. (42). We put  $e_{xy} = 0.15$  eV, and the others are 0. The obtained FSs in the  $k_z = 0$  plane are shown in Fig. 31 (a). Near the  $\Gamma$  point, the h-FS composing  $d_{xy}$ -orbital is largest of three h-FSs. In addition, we present the results in the presence of small amount of impurity ( $I = 1$  and  $n_{\text{imp}} = 0.04$ ), just to make the SC gap structures smoother. To consider impurity effect, we use the  $T$ -matrix approximation as calculated in Ref.[16]. Here, we don't consider the SOI.

Figure 31 (b) shows the  $\alpha_c$ - $\alpha_s$  diagram of the gap structure in Ba122. In common with  $\text{LiFeAs}$ , Each  $s_{\pm}$ ,  $s_{++}$ , and hole- $s_{\pm}$  wave state is realized in wide parameter region. The gap structure on the plain  $k_z = 0$  at each point **a**  $\sim$  **d** is shown in the figure. h-FSs are the FSs around  $\Gamma$  point and e-FSs are the FSs around X point. The horizontal axis is  $\theta = \tan(\bar{k}_y/\bar{k}_x)$ , where  $(\bar{k}_x, \bar{k}_y)$  is the momentum on the FS with the origin at the center of each pocket. In the region " $\Delta_{xy}^h \sim 0$  ( $\Delta_{xz/yz}^h \sim 0$ )", the gaps on the other h-FSs and e-FSs have the same (opposite) sign, so nearly  $s_{++}$  ( $s_{\pm}$ )-wave state is realized.

When both  $\alpha_c$  and  $\alpha_s$  are close to unity, hole- $s_{\pm}$ -wave state is realized. At point **c**, the gap on only outer h-FS, which mainly consists of  $d_{xy}$ -orbital, is sign reversed. In addition, the gap at  $\theta = \pi/2, k_z = 0$  on the inner e-FS is relatively small, which is consistent with ARPES measurements[54].

When  $\alpha_c$  and  $\alpha_s$  are not near unity, nodal- $s$ -wave, which has loop nodes in e-FSs is realized between  $s_{++}$  and  $s_{\pm}$ -wave state. At point **b**, obtained gap structure has a loop node at  $\theta = \pi/2, k_z = 0$ . This gap structure corresponds to fig. 29. [16] When we set larger  $g$  or smaller  $U$ , obtained gap structure has a loop node at  $\theta = 0, k_z = 0$ , which corresponds to fig. 27. [16]. Therefore, a wide variety of gap structures can be obtained by cooperation of orbital and spin fluctuations.

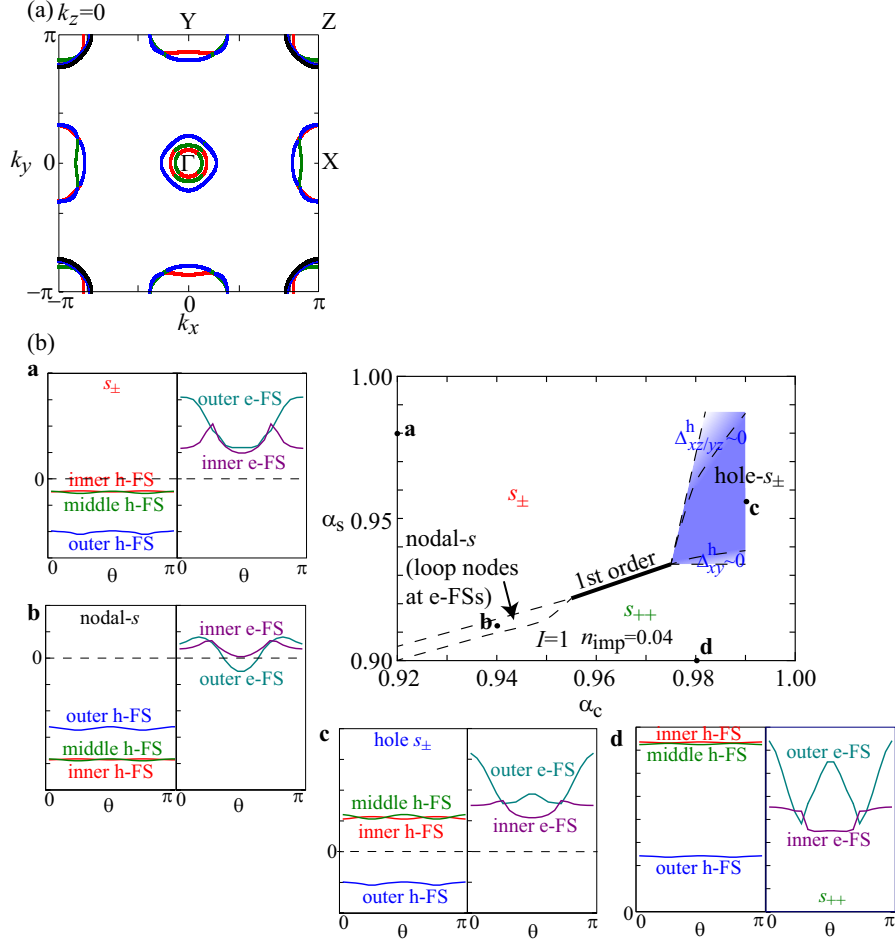


Figure 31: (a) The FSs in the  $k_z = 0$  plane of the three dimensional model for Ba122. The green, red, blue, and black lines correspond to  $xz$ ,  $yz$ ,  $xy$ , and  $z^2$  orbitals, respectively. (b)  $\alpha_c$ - $\alpha_s$  diagram of the gap structure in Ba122. The gap structure at each point **a**  $\sim$  **d** is shown in the figure. h-FSs are the FSs around  $\Gamma$  point and e-FSs are the FSs around X point. The horizontal axis is  $\theta = \tan(\bar{k}_y/\bar{k}_x)$ , where  $(\bar{k}_x, \bar{k}_y)$  is the momentum on the FS with the origin at the center of each pocket. Each  $s_{\pm}$ -wave,  $s_{++}$ -wave, and hole- $s_{\pm}$ -wave is realized in a wide parameter region. In the region " $\Delta_{xy}^h \sim 0$  ( $\Delta_{xz/yz}^h \sim 0$ )", the gaps on the other h-FSs and e-FSs have the same (opposite) sign, so nearly  $s_{++}$  ( $s_{\pm}$ )-wave state is realized.

## References

- [1] Y. Kamihara, T. Watanabe, M. Hirano, and H. Hosono, J. Am. Chem. Soc. **130**, 3296 (2008).
- [2] H. K. Onnes, Comm. Phys. Lab. Univ. Leiden, No. 119, 120, 133 (1911).
- [3] J. Bardeen, L. N. Cooper, and J. R. Schrieffer. Phys. Rev. **108**, 1175 (1957).
- [4] J. G. Bednorz and K. A. Müller, Z. Phys. B **64**, 189 (1986).
- [5] K. Kuroki, S. Onari, R. Arita, H. Usui, Y. Tanaka, H. Kontani, and H. Aoki, Phys. Rev. Lett. **101**, 087004 (2008).
- [6] H. Kontani and S. Onari, Phys. Rev. Lett. **104**, 157001 (2010).
- [7] M. Sato, Y. Kobayashi, S. C. Lee, H. Takahashi, E. Satomi, and Y. Miura, J. Phys. Soc. Jpn. **79**, 014710 (2010); S. C. Lee, E. Satomi, Y. Kobayashi, and M. Sato, *ibid.* **79**, 023702 (2010).
- [8] J. Li, Y. F. Guo, S. B. Zhang, J. Yuan, Y. Tsujimoto, X. Wang, C.I. Sathish, Y. Sun, S. Yu, W. Yi, K. Yamaura, E. Takayama-Muromachi, Y. Shirako, M. Akaogi, and H. Kontani, Phys. Rev. B **85**, 214509 (2012).
- [9] S. Onari and H. Kontani, Phys. Rev. Lett. **103**, 177001 (2009).
- [10] Y. Yamakawa, S. Onari, and H. Kontani, Phys. Rev. B **87**, 195121 (2013).
- [11] F. L. Ning, K. Ahilan, T. Imai, A. S. Sefat, M. A. McGuire, B. C. Sales, D. Mandrus, P. Cheng, B. Shen, and H.-H Wen, Phys. Rev. Lett. **104**, 037001 (2010).
- [12] Z. Li, Y. Ooe, X.-C. Wang, Q.-Q. Liu, C.-Q. Jin, M. Ichioka, and G.-q. Zheng, J. Phys. Soc. Jpn **79**, 083702 (2010).
- [13] S. Onari and H. Kontani, Phys. Rev. Lett. **109**, 137001 (2012).
- [14] S. Onari, Y. Yamakawa and H. Kontani, Phys. Rev. Lett. **112**, 187001 (2014).
- [15] H. Kontani and Y. Yamakawa, Phys. Rev. Lett. **113**, 047001 (2014).

- [16] T. Saito, S. Onari, and H. Kontani, *Phys. Rev. B* **88**, 045115 (2013).
- [17] M. Yi, D. H. Lu, J.-H. Chu, J. G. Analytis, A. P. Sorini, A. F. Kemper, S.-K. Mo, R. G. Moore, M. Hashimoto, W. S. Lee, Z. Hussain, T. P. Devereaux, I. R. Fisher, and Z.-X. Shen, *Proc. Natl. Acad. Sci. USA* **108**, 6878 (2011).
- [18] R. M. Fernandes, L. H. VanBebber, S. Bhattacharya, P. Chandra, V. Keppens, D. Mandrus, M. A. McGuire, B. C. Sales, A. S. Sefat, and J. Schmalian, *Phys. Rev. Lett.* **105**, 157003 (2010).
- [19] M. Yoshizawa, R. Kamiya, R. Onodera, Y. Nakanishi, K. Kihou, H. Eisaki and C. H. Lee, *Phys. Soc. Jpn.* **81**, 024604 (2012).
- [20] T. Goto, R. Kurihara, K. Araki, K. Mitsumoto, M. Akatsu, Y. Nemoto, S. Tatematsu, and M. Sato, *J. Phys. Soc. Jpn.* **80**, 073702 (2011).
- [21] J. L. Niedziela, D. Parshall, K. A. Lokshin, A. S. Sefat, A. Alatas, and T. Egami, *Phys. Rev. B* **84**, 224305 (2011).
- [22] T. Miyake, K. Nakamura, R. Arita, and M. Imada, *J. Phys. Soc. Jpn.* **79**, 044705 (2010).
- [23] I. I. Mazin, D. J. Singh, M. D. Johannes, and M. H. Du, *Phys. Rev. Lett.* **101**, 057003 (2008).
- [24] T. Nomura, *J. Phys. Soc. Jpn.* **78**, 034716 (2009).
- [25] H. Ikeda, R. Arita, and J. Kuneš, *Phys. Rev. B*, **82**, 024508 (2010).
- [26] T. Moriya, Y. Takahashi, and K. Ueda, *J. Phys. Soc. Jpn.* **59**, 2905 (1990); K. Ueda, T. Moriya, and Y. Takahashi, *J. Phys. Chem. Solids*, **53**, 1515 (1992).
- [27] P. Monthoux and D. Pines, *Phys. Rev. B* **47**, 6069 (1993).
- [28] N. E. Bickers and S. R. White, *Phys. Rev. B* **43**, 8044 (1991).
- [29] J. Schmalian, *Phys. Rev. Lett.* **81**, 4232 (1998).
- [30] H. Kino and H. Kontani, *J. Phys. Soc. Jpn.* **67**, 3691 (1998).
- [31] H. Kondo and T. Moriya, *J. Phys. Soc. Jpn.* **67**, 3695 (1998).

- [32] T. Takimoto, T. Hotta, and K. Ueda, Phys. Rev. B **69**, 104504 (2004).
- [33] Y. Nakajima, T. Taen, Y. Tsuchiya, T. Tamegai, H. Kitamura, and T. Murakami, Phys. Rev. B **82**, 220504 (2010).
- [34] A. D. Christianson, E. A. Goremychkin, R. Osborn, S. Rosenkranz, M. D. Lumsden, C. D. Malliakas, I. S. Todorov, H. Claus, D. Y. Chung, M. G. Kanatzidis, R. I. Bewley, and T. Guidi, Nature (London) **456**, 930 (2008).
- [35] Y. Qiu, W. Bao, Y. Zhao, C. Broholm, V. Stanev, Z. Tesanovic, Y. C. Gasparovic, S. Chang, J. Hu, B. Qian, M. Fang, and Z. Mao, Phys. Rev. Lett. **103**, 067008 (2009).
- [36] D. S. Inosov, J. T. Park, P. Bourges, D. L. Sun, Y. Sidis, A. Schneidewind, K. Hradil, D. Haug, C. T. Lin, B. Keimer, and V. Hinkov, Nature Phys. **6**, 178 (2010).
- [37] S. Onari, H. Kontani, and M. Sato, Phys. Rev. B **81**, 060504(R) (2010); S. Onari and H. Kontani, *ibid.* **84**, 144518 (2011).
- [38] Y. Nakai, T. Iye, S. Kitagawa, K. Ishida, H. Ikeda, S. Kasahara, H. Shishido, T. Shibauchi, Y. Matsuda, and T. Terashima, Phys. Rev. Lett. **105**, 107003 (2010).
- [39] T. Nakano, N. Fujiwara, K. Tatsumi, H. Okada, H. Takahashi, Y. Kamihara, M. Hirano, and H. Hosono, Phys. Rev. B **81**, 100510(R) (2010).
- [40] H. Kontani, T. Saito, and S. Onari, Phys. Rev. B **84**, 024528 (2011).
- [41] T. Saito, S. Onari, and H. Kontani, Phys. Rev. B **82**, 144510 (2010).
- [42] T. Saito, S. Onari, and H. Kontani, Phys. Rev. B **83**, 140512(R) (2011).
- [43] H. Kontani, Y. Inoue, T. Saito, Y. Yamakawa, and S. Onari, Solid State Commun. **152**, 718 (2012).
- [44] Y. Ohno, M. Tsuchiizu, S. Onari, and H. Kontani, J. Phys. Soc. Jpn. **82**, 013707 (2013).
- [45] M. Tsuchiizu, Y. Ohno, S. Onari, and H. Kontani, Phys. Rev. Lett. **111**, 057003 (2013).

- [46] T. Takimoto, T. Hotta, T. Maehira, and K. Ueda, *J. Phys. Condens. Matter* **14**, L369 (2002).
- [47] Y. Zhang, L. X. Yang, M. Xu, Z. R. Ye, F. Chen, C. He, H. C. Xu, J. Jiang, B. P. Xie, J. J. Ying, X. F. Wang, X. H. Chen, J. P. Hu, M. Matsunami, S. Kimura, and D. L. Feng, *Nature Mater.* **10**, 273 (2011).
- [48] T. Qian, X.-P. Wang, W.-C. Jin, P. Zhang, P. Richard, G. Xu, X. Dai, Z. Fang, J.-G. Guo, X.-L. Chen, and H. Ding, *Phys. Rev. Lett.* **106**, 187001 (2011).
- [49] L. Zhao, D. Mou, S. Liu, X. Jia, J. He, Y. Peng, L. Yu, X. Liu, G. Liu, S. He, X. Dong, J. Zhang, J. B. He, D. M. Wang, G. F. Chen, J. G. Guo, X. L. Chen, X. Wang, Q. Peng, Z. Wang, S. Zhang, F. Yang, Z. Xu, C. Chen, and X. J. Zhou, *Phys. Rev. B* **83**, 140508(R) (2011).
- [50] B. Zeng, B. Shen, G. Chen, J. He, D. Wang, C. Li, and H.-H. Wen, *Phys. Rev. B* **83**, 144511 (2011).
- [51] S. Borisenko, D. Evtushinsky, I. Morozov, S. Wurmehl, B. Büchner, A. Yaresko, T. Kim, and M. Hoesch, arXiv:1409.8669.
- [52] H. Miao, L.-M. Wang, P. Richard, S.-F. Wu, J. Ma, T. Qian, L.-Y. Xing, X.-C. Wang, C.-Q. Jin, C.-P. Chou, Z. Wang, W. Ku, and H. Ding, *Phys. Rev. B* **89**, 220503(R) (2014).
- [53] M. Yamashita, Y. Senshu, T. Shibauchi, S. Kasahara, K. Hashimoto, D. Watanabe, H. Ikeda, T. Terashima, I. Vekhter, A. B. Vorontsov, and Y. Matsuda, *Phys. Rev. B* **84**, 060507(R) (2011).
- [54] T. Yoshida, S. Ideta, T. Shimojima, W. Malaeb, K. Shinada, H. Suzuki, I. Nishi, A. Fujimori, K. Ishizaka, S. Shin, Y. Nakashima, H. Anzai, M. Arita, A. Ino, H. Namatame, M. Taniguchi, H. Kumigashira, K. Ono, S. Kasahara, T. Shibauchi, T. Terashima, Y. Matsuda, M. Nakajima, S. Uchida, Y. Tomioka, T. Ito, K. Kihou, C. H. Lee, A. Iyo, H. Eisaki, H. Ikeda, R. Arita, T. Saito, S. Onari, and H. Kontani, *Sci. Rep.* **4**, 7292 (2014).
- [55] J. Guo, S. Jin, G. Wang, S. Wang, K. Zhu, T. Zhou, M. He, and X. Chen, *Phys. Rev. B* **82**, 180520(R) (2010).



- [56] I. R. Shein and A. L. Ivanovskii, Phys. Lett. A **375**, 1028 (2011).
- [57] I. A. Nekrasov and M. V. Sadovskii, Pisma Zh. Eksp. Teor. Fiz. [JETP Lett.] **93**, 182 (2011).
- [58] W. Yu, L. Ma, J. B. He, D. M. Wang, T.-L. Xia, and G. F. Chen, Phys. Rev. Lett. **106**, 197001 (2011).
- [59] F. Wang, F. Yang, M. Gao, Z.-Y. Lu, T. Xiang, and D.-H. Lee, Europhys Lett. **93**, 57003 (2011).
- [60] T. A. Maier, S. Graser, P. J. Hirschfeld, and D. J. Scalapino, Phys. Rev. B **83**, 100515(R) (2011).
- [61] T. Das and A. V. Balatsky, Phys. Rev. B **84**, 014521 (2011).
- [62] J. Kunes, R. Arita, P. Wissgott, A. Toschi, H. Ikeda, and K. Held, Comp. Phys. Commun. **181**, 1888 (2010).
- [63] K. Yada and H. Kontani, Phys. Rev. B **77**, 184521 (2008); J. Phys. Soc. Jpn. **75**, 033705 (2006).
- [64] S. Onari and H. Kontani, Phys. Rev. B **85**, 134507 (2012).
- [65] I. I. Mazin, Phys. Rev. B **84**, 024529 (2011).
- [66] S. V. Borisenko, V. B. Zabolotnyy, A. A. Kordyuk, D. V. Evtushinsky, T. K. Kim, I. V. Morozov, R. Follath, and B. Büchner, Symmetry **4**, 251 (2012).
- [67] K. Umezawa, Y. Li, H. Miao, K. Nakayama, Z.-H. Liu, P. Richard, T. Sato, J. B. He, D.-M. Wang, G. F. Chen, H. Ding, T. Takahashi, and S.-C. Wang, Phys. Rev. Lett. **108**, 037002 (2012).
- [68] N. Qureshi, P. Steffens, Y. Drees, A.C. Komarek, D. Lamago, Y. Sidis, L. Harnagea, H.-J. Grafe, S. Wurmehl, B. Büchner, and M. Braden, Phys. Rev. Lett. **108**, 117001 (2012).
- [69] J. Knolle, V. B. Zabolotnyy, I. Eremin, S. V. Borisenko, N. Qureshi, M. Braden, D. V. Evtushinsky, T. K. Kim, A. A. Kordyuk, S. Sykora, Ch. Hess, I. V. Morozov, S. Wurmehl, R. Moessner, and B. Büchner, Phys. Rev. B **86**, 174519 (2012).

- [70] A. E. Taylor, M. J. Pitcher, R. A. Ewings, T. G. Perring, S. J. Clarke, and A. T. Boothroyd, *Phys. Rev. B* **83**, 220514 (2011).
- [71] Y. Wang, A. Kreisel, V. B. Zabolotnyy, S. V. Borisenko, B. Büchner, T. A. Maier, P. J. Hirschfeld, and D. J. Scalapino, *Phys. Rev. B* **88**, 174516 (2013).
- [72] M. P. Allan, A. W. Rost, A. P. Mackenzie, Yang Xie, J. C. Davis, K. Kihou, C. H. Lee, A. Iyo, H. Eisaki, and T.-M. Chuang, *Science* **336**, 563 (2012).
- [73] S. Graser, A. F. Kemper, T. A. Maier, H.-P. Cheng, P. J. Hirschfeld, and D. J. Scalapino, *New J. of Phys.* **12**, 073030 (2010); *Phys. Rev. B* **81**, 214503 (2010).
- [74] D. Watanabe, T. Yamashita, Y. Kawamoto, S. Kurata, Y. Mizukami, T. Ohta, S. Kasahara, M. Yamashita, T. Saito, H. Fukazawa, Y. Kohori, S. Ishida, K. Kihou, C. H. Lee, A. Iyo, H. Eisaki, A. B. Vorontsov, T. Shibauchi, and Y. Matsuda, *Phys. Rev. B* **89**, 115112 (2014).
- [75] P. Zhang, P. Richard, T. Qian, X. Shi, J. Ma, L.-K. Zeng, X.-P. Wang, E. Rienks, C.-L. Zhang, Pengcheng Dai, Y.-Z. You, Z.-Y. Weng, X.-X. Wu, J. P. Hu, and H. Ding, *Phys. Rev. X* **4**, 031001 (2014).
- [76] T. Saito, S. Onari, Y. Yamakawa, H. Kontani, S. V. Borisenko, and V. B. Zabolotnyy, *Phys. Rev. B* **90**, 035104 (2014).
- [77] S. Maiti and A. V. Chubukov, *Phys. Rev. B* **87**, 144511 (2013).
- [78] F. Ahn, I. Eremin, J. Knolle, V. B. Zabolotnyy, S. V. Borisenko, B. Büchner, and A. V. Chubukov, *Phys. Rev. B* **89**, 144513 (2014).
- [79] Z. P. Yin, K. Haule, and G. Kotliar, *Nature Phys.* **10**, 845 (2014).
- [80] J. Friedel, P. Lenglar, and G. Leman, *J. Phys. Chem. Solids* **25**, 781 (1964).
- [81] T. Shimojima, F. Sakaguchi, K. Ishizaka, Y. Ishida, T. Kiss, M. Okawa, T. Togashi, C.-T. Chen, S. Watanabe, M. Arita, K. Shimada, H. Namatame, M. Taniguchi, K. Ohgushi, S. Kasahara, T. Terashima, T. Shibauchi, Y. Matsuda, A. Chainani, and S. Shin, *Science* **332**, 564 (2011).

- [82] Y. Zhang, Z. R. Ye, Q. Q. Ge, F. Chen, J. Jiang, M. Xu, B. P. Xie, and D. L. Feng, *Nature Phys.* **8**, 371 (2012).
- [83] K. Suzuki, H. Usui, and K. Kuroki, *J. Phys. Soc. Jpn.* **80**, 013710 (2011).
- [84] J. S. Kim, P. J. Hirschfeld, G. R. Stewart, S. Kasahara, T. Shibauchi, T. Terashima, and Y. Matsuda, *Phys. Rev. B* **81**, 214507 (2010)
- [85] Y. Wang, J. S. Kim, G. R. Stewart, and P. J. Hirschfeld, S. Graser, S. Kasahara and T. Terashima, Y. Matsuda, T. Shibauchi, and I. Vekhter, *Phys. Rev. B* **84**, 184524 (2011).
- [86] D. V. Efremov, M. M. Korshunov, O. V. Dolgov, A. A. Golubov, and P. J. Hirschfeld, *Phys. Rev. B* **84**, 180512(R) (2011).
- [87] K. Kuroki, H. Usui, S. Onari, R. Arita, and H. Aoki, *Phys. Rev. B* **79**, 224511 (2009).
- [88] H. Kontani, *Phys. Rev. B* **70**, 054507 (2004).
- [89] P. Steffens, C. H. Lee, N. Qureshi, K. Kihou, A. Iyo, H. Eisaki, and M. Braden, *Phys. Rev. Lett.* **110**, 137001 (2013).
- [90] O. J. Lipscombe, L. W. Harriger, P. G. Freeman, M. Enderle, C. Zhang, M. Wang, T. Egami, J. Hu, T. Xiang, M. R. Norman, and P. Dai, *Phys. Rev. B*, **82**, 064515 (2010).
- [91] Z. Yin, K. Haule, and G. Kotliar, *Nat. Mater.* **10**, 932 (2011); J. Ferber, K. Foyevtsova, R. Valenti, and H. O. Jeschke, *Phys. Rev. B* **85**, 094505 (2012); G. Lee, H. S. Ji, Y. Kim, C. Kim, K. Haule, G. Kotliar, B. Lee, S. Khim, K. H. Kim, K. S. Kim, K.-S. Kim, and J. H. Shim, *Phys. Rev. Lett.* **109**, 177001 (2012).
- [92] C. Putzke, A. I. Coldea, I. Guillamo'n, D. Vignolles, A. McCollam, D. LeBoeuf, M. D. Watson, I. I. Mazin, S. Kasahara, T. Terashima, T. Shibauchi, Y. Matsuda, and A. Carrington, *Phys. Rev. Lett.* **108**, 047002 (2012).
- [93] B. Zeng, D. Watanabe, Q. R. Zhang, G. Li, T. Besara, T. Siegrist, L. Y. Xing, X. C. Wang, C. Q. Jin, P. Goswami, M. D. Johannes, and L. Balicas, *Phys. Rev. B* **88**, 144518 (2013).